POLITECNICO DI TORINO

Master's Degree in Civil Engineering

Master thesis

FLUTTER ANALYSIS OF LONG-SPAN SUSPENSION BRIDGES:

THE CASE-STUDY OF THE MESSINA STRAIT PROJECT

Supervisors:
Prof. Alberto Carpinteri
Dr. Gianfranco Piana
Eng. Sebastiano Russo

Candidate:
Stella Huang

Academic year 2022/2023

Ringraziamenti

Giunta al termine del mio percorso universitario mi è doveroso ringraziare tutti coloro che mi hanno sostenuta durante i miei studi e che ne hanno contribuito.

Un ringraziamento speciale al Prof. Alberto Carpinteri, per avermi trasmesso la passione per l'ingegneria strutturale, in particolare l'instabilità aeroelastica dei ponti sospesi, dandomi l'opportunità e la fiducia nell'affrontare questo lavoro di tesi magistrale.

Ringrazio il Dott. Gianfranco Piana e l'Ing. Sebastiano Russo, che con la loro pazienza e infinita disponibilità mi hanno guidata durante tutto il percorso di stesura dell'elaborato.

Un grazie di cuore ai miei amici, che nonostante la distanza che ci separa, non hanno mai smesso di sostenermi, con cui ho condiviso i momenti di gioia e di difficoltà durante questi anni, sono grata di avervi avuto al mio fianco.

Per ultimo vorrei ringraziare i miei familiari, che hanno sempre creduto in me incondizionatamente, è merito della loro fiducia e del loro amore che sono riuscita a raggiungere questo traguardo.

Abstract

The construction of a permanent link over the Messina Strait has always been considered a great undertaking, due to challenging environmental conditions such as the depth of water, strong sea current, intense wind, and seismic activities. These factors, among others, have significantly delayed the design stage and subsequent possible construction. The bridge's design and feasibility debate began several decades ago, culminating in 1992, with the approval of the world's longest suspension bridge project, featuring a main span of 3300 metres.

This thesis focuses on one of the most dangerous phenomena that could occur in suspension bridges, i.e. *flutter instability*. The analysis aims to investigate the behaviour of the Messina Strait Bridge under wind loads, utilizing both numerical and analytical approaches.

The first part provides a brief overview of the evolutionary process of suspension bridges in history. Subsequently, the development of the Messina Strait Bridge project is presented, from the 1969 international design competition up to the most recent updates, including the feasibility analyses conducted regarding the different solution proposed. Furthermore, the various effects of wind action on long-span suspension bridges are described. Being a project of great relevance, many researchers have conducted extensive studies, two of these are reported and their results will be compared to the ones obtained in this thesis.

The second part of this thesis describes in depth the approved project and focuses on the various finite element models developed, from a simpler model of the main span only to the complete model of the entire bridge. The numerical methods adopted in this study are then introduced and the analyses performed using both MATLAB and ANSYS software are reported. They consist of a preliminary modal analysis, in order to determine the natural frequencies and the vibration modes, then the flutter analysis is carried out, which takes into account all the aerodynamic loads involved, modelled by the flutter derivatives. In the end, the critical flutter velocity of the wind, that initiates instability, and the flutter frequency are derived. In addition, some considerations have been made regarding the influence of the Drag component on the critical wind speed. Lastly, a further method was explored, the single-mode criterion, which allows to examine uncoupled single-degree-of-freedom flutter problems, and it was applied on the Messina Bridge project as well as on the Tacoma Narrows Bridge, a well-known case of instability that had led to failure.

In conclusion, the critical flutter wind speed is assessed to be over 94 m/s, which corresponds to 340 km/h, extremely higher than most severe wind ever recorded at the bridge's location. The results derived from the flutter analyses, performed using MATLAB and ANSYS software, in terms of critical flutter wind speed and flutter frequency, agree with each other within

4% error, thus both analytical and numerical approaches produce the same result. Moreover, they align strongly with the values obtained by the research groups examined, with a relative error under 8%. An additional flutter analysis is performed in order to assess the influence of the lateral flutter derivatives, which proves to be essential to achieve flutter instability in long-span bridges.
Similarly, the model was studied utilizing the single-mode criterion; however, it doesn't produce any worthwhile results due to the fact that the bride's deck was designed to resemble an air foil, therefore highly stable to single-degree-of-freedom flutter and the critical mechanism always involves the coupling between two, or more, modes.
In the end, numerical and analytical investigations, confirm the excellent aeroelastic behaviour of the bridge over the Messina Strait, whose design was carefully developed in the last few decades.

Table of contents

Ringraziamenti I

Abstract II

List of Figures VI

List of Tables VIII

PART 1 1

Chapter 1 2

Introduction on long-span suspension bridges 2

1.1. Suspension bridge evolution 3

1.2. The Messina Strait Bridge project development 6

Chapter 2 14

Wind effects on long-span suspension bridges 14

2.1. Steady aerodynamic analysis 15

2.2. Torsional divergence 17

2.3. Two-degree-of-freedom flutter 18

2.4. Three-degree-of-freedom flutter 21

2.5. The single-mode criterion 23

Chapter 3 24

Aeroelastic studies of the Messina Bridge project 24

3.1. Diana *et al.* studies 25

3.2. Jurado *et al.* studies 28

3.3. D'Asdia and Sepe studies 32

PART 2 35

Chapter 4 36

Messina Strait Bridge project 36

4.1. General bridge outline 36

4.2. Suspended deck 37

4.3. Deck restrains and expansion joints 39

4.4. Suspension system 41

4.5. Towers 41

4.6. Foundations 44

4.7. Operation & maintenance strategies 44
Chapter 5 45
MATLAB flutter analysis 45
5.1. Introduction to multimodal aeroelastic analysis 45
5.2. Messina Strait bridge project case 47
5.3. Result comparison 49
Chapter 6 50
ANSYS flutter analysis 50
6.1. Flutter problem using ANSYS 50
6.2. Structural FE models 54
6.2.1. Fishbone model, main span 54
6.2.2. Fishbone model, three spans 57
6.2.3. Complete model 59
6.3. Flutter analysis 61
6.4. Result comparison 64
6.5. Influence of lateral flutter derivatives 65
Chapter 7 67
The single-mode criterion 67
7.1. Introduction 67
7.2. The Tacoma Narrows bridge case 69
7.3. The Messina Strait bridge case 71
Chapter 8 74
Conclusions 74
References 76

List of Figures

Figure 1.1 Suspension bridge scheme with force flow (Akashi Kaikyo bridge) 2
Figure 1.2 View of the Golden Gate bridge during its construction 4
Figure 1.3 View of the Severn bridge during its construction 5
Figure 1.4 View of the Canakkale bridge during its construction [3] 5
Figure 1.5 Visual impact assessment on the Sicilian side 6
Figure 1.6 Four span bridged proposed by Arch. Montuori, engineer Calini and Pavlo 7
Figure 1.7 Floating underwater tunnel by Grant Alan and Partners, Covell and Partners, Inbucon international 7
Figure 1.8 Three span stayed bridge by Lambertini Group 7
Figure 1.9 Single span suspension bridge by Musmeci Group 8
Figure 1.10 Three span suspension bridge by Ponte di Messina Group SpA 8
Figure 1.11 Five span suspension bridge by Technital SpA 8
Figure 1.12 (a) Original sketches of Dr. Brown of the multi-box deck [6] 9
Figure 1.13 (b) Original sketches of Dr. Brown of the multi-box deck [6] 9
Figure 1.14 Proposed crossing solutions 10
Figure 1.15 View of the landscape for Calabria side 11
Figure 1.16 View of the bridge from the deck 12
Figure 1.17 New comcept of suspension bridge 12
Figure 1.18 Additional cable system 13
Figure 2.1 Suspension bridge scheme 14
Figure 2.2 Steady aerodynamic model 15
Figure 2.3 Examples of aerodynamic coefficients 16
Figure 2.4 One-degree-of-freedom simplified model 17
Figure 2.5 Two-degree-of-freedom simplified model 19
Figure 2.6 Examples of flutter derivatives [9] 21
Figure 2.7 Three-degree-of-freedom simplified model 21
Figure 3.1 Messina strait bridge project main features 25
Figure 3.2 Deck design 25
Figure 3.3 General layout of the research 25
Figure 3.4 Vibration modes 26
Figure 3.5 Aeroelastic full bridge model (1:250 scale) 27
Figure 3.6 Vertical and torsional frequency variation 28
Figure 3.7 Finite element model of the Messina Bridge 28
Figure 3.8 Wind tunnel testing of the Messina bridge deck 30
Figure 3.9 Flutter derivatives of Messina Bridge 30
Figure 3.10 Natural frequencies and mode shapes considered for flutter analysis 31
Figure 3.11 Flutter analysis result 32
Figure 3.12 1992 design of the proposed bridge 32

Figure 3.13 Flutter derivatives 33
Figure 3.14 Natural modes 34
Figure 4.1 Plan view of the location and the connections 36
Figure 4.2 Side view of the Messina Bridge 36
Figure 4.3 Virtual view from the deck 38
Figure 4.4 Virtual view from below the bridge 38
Figure 4.5 3D model of the 2005 proposed deck 39
Figure 4.6 Lateral span on Sicilian side 40
Figure 4.7 Proposed deck-tower connection 41
Figure 4.8 Preliminary design of the towers 42
Figure 4.9 Towers according to the 2005 proposal 43
Figure 4.10 Structural instrumentation layout 44
Figure 5.1 Flutter derivatives of the Messina bridge project 47
Figure 5.2 Damping factors and modal frequencies 48
Figure 5.3 Messina bridge modal shapes in wind-free condition 48
Figure 5.4 Messina bridge modal shapes critical flutter condition 49
Figure 6.1 Hybrid finite element model 51
Figure 6.2 FE model 1 of the Messina Strait bridge project 54
Figure 6.3 Modal frequencies and modal shapes of the model 1 56
Figure 6.4 FE model 2 of the Messina Strait bridge project 57
Figure 6.5 Modal frequencies and modal shapes of the model 2 58
Figure 6.6 FE model 3 of the Messina Strait bridge project 59
Figure 6.7 Model 3 deck detail 59
Figure 6.8 Modal frequencies and modal shapes of the model 3 60
Figure 6.9 FE model 3 with MATRIX27 elements 61
Figure 6.10 Flutter derivatives derived at the University of La Coruña 62
Figure 6.11 Variation of the real part of complex eigenvalues 63
Figure 6.12 Variation of the imaginary part of complex eigenvalues 63
Figure 6.13 Flutter shape: coupled vertical, torsional and lateral modes 64
Figure 6.14 Variation of the real and the imaginary part of complex eigenvalue, without drag case 66
Figure 6.15 Comparison of the variation of the real and the imaginary part of complex eigenvalue 66
Figure 7.1 Lateral view of Tacoma Narrows bridge 69
Figure 7.2 Tacoma Narrows bridge collapse 69
Figure 7.3 Examples of $A2*$ flutter derivatives 69
Figure 7.4 Torsional single-degree-of-freedom flutter 70
Figure 7.5 $A2*$, $P1*$ and $H1*$ of Messina Strait bridge 71
Figure 7.6 Sway single-degree-of-freedom flutter 71
Figure 7.7 Bending single-degree-of-freedom flutter 72
Figure 7.8 Torsional single-degree-of-freedom flutter 72

List of Tables

Table 1.1 Record breaking bridges built in the world 3
Table 3.1 Natural frequencies 26
Table 3.2 Dynamic verification on the 1:250 full bridge aeroelastic model 27
Table 3.3 Geometrical and mechanical properties FE model 29
Table 3.4 Natural frequencies of the Messina Bridge 29
Table 3.5 Mechanical properties assumed 33
Table 3.6 Natural angular frequency and period 33
Table 3.7 Results of the multi-mode analysis 34
Table 5.1 Main features of the study-case 47
Table 5.2 Steady-state aerodynamic coefficients 47
Table 5.3 Messina bridge flutter analysis, result comparison 49
Table 6.1 Geometrical and mechanical properties of the Messina Strait bridge project 55
Table 6.2 Modal frequencies and modal shapes comparison 55
Table 6.3 Geometrical and mechanical properties of the Messina Strait bridge project 57
Table 6.4 Modal frequencies and modal shapes comparison 57
Table 6.5 Geometrical and mechanical properties of the Messina Strait bridge project 59
Table 6.6 Modal frequencies and modal shapes comparison 60
Table 6.7 Messina bridge flutter analysis, result comparison 64

PART 1

Chapter 1

Introduction on long-span suspension bridges

Suspension bridges possess an unmistakable architectural profile, rendering their surrounding landscape extremely identifiable. To mention some of the most famous bridges: the Brooklyn Bridge in New York and the Golden Gate Bridge in San Francisco.

It's a type of bridge in which the traffic-carrying deck is hung by means of hangers below the main cables, suspended between tall towers and anchored at each end of the bridge. This arrangement allows the deck to be levelled or to arc upwards for additional clearance.

The loads applied to the deck, are carried to the main cables through hangers and subsequently brought to the ground mainly through the towers for the vertical component and through the anchor blocks for the horizontal one.

Figure 1.1 Suspension bridge scheme with force flow (Akashi Kaikyo bridge)

1.1. Suspension bridge evolution

The earliest versions of this type of bridges dates back to the 15th century, built by a Tibetan siddha using iron chains to build the most primitive version of suspension bridge [1].
The bridge over the Menai Strait can be considered as one of the first modern suspension bridge, built in Wales by Thomas Telford and completed in 1826. After that, many suspension bridges have been built, often with the intention of building a record-breaking bridge, featuring the longest span ever. The first one worth mentioning is the Brooklyn bridge in New York, that spans over 486 m, opened to traffic in 1883. More than half of a century later 3 more bridges broke that record, all located in the USA: George Washington Bridge, Golden Gate Bridge and Verrazzano Narrows Bridge. Subsequently 2 European bridges were finalized: Humber Bridge in England and Great Belt East Bridge in Denmark, however this latter record didn't last long because in the same year, in 1998, the Akashi Kaikyo Bridge was completed and its record lasted until 2022, when the Canakkale Bridge was built in Turkey and its main span covers 2023 meters.

The following table summarizes all the previously mentioned bridges:

Construction end	Bridge	Location	Main span length
1883	Brooklyn bridge	New York	486 m
1931	George Washington Bridge	New York	1067 m
1937	Golden Gate Bridge	San Francisco	1280 m
1964	Verrazzano Narrows Bridge	New York	1298 m
1981	Humber Bridge	United Kindom	1410 m
1998	Great Belt East Bridge	Denmark	1624 m
1998	Akashi Kaikyo Bridge	Japan	1991 m
2022	1915 Çanakkale Bridge	Turkey	2023 m

Table 1.1 Record breaking bridges built in the world

As is clear from the Table 1.1, from the first half of the 20th, suspension bridges started gaining popularity due to their long span lengths, that allowed to overcome greater distances, that otherwise would not be accomplished with other types of bridges. Furthermore, it is more cost efficient than other bridges, as it requires less material while covering greater distances, and it is usually built without the use of falsework therefore it doesn't require access from below. Moreover, another fundamental advantage is the stability to seismic actions, hence it could even be built even on seismic sites.
The main issue with suspension bridges is due to their flexibility that makes them more prone to wind effects, that could induce instability or excessive vibration. Instability caused by the interaction between an air flow and an elastic structure is called *aeroelastic instability*. The attention was drawn on this aspect after the Tacoma Narrows Bridge collapse in 1940, when under a recorded wind speed

of around 20 m/s, the bridge started to develop wave motions and twisting motion of the roadway, that resulted in failure a few hours later.

It's possible to divide the suspension bridges evolution in three generations:

- The first generation consist of truss deck bridges, built in the USA between the end of the 19th and the beginning of the 20th century (i.e. Brooklyn 1883, Golden Gate 1937). The truss deck gives high flexural and torsional stiffness to the structure however, higher stiffnesses correspond to larger masses, which represent a critical aspect for long-span bridges. The span length of the Akashi Kaikyo bridge (1998) reaches 1991 m, which is the maximum limit for this type of bridge, it's important also to point out that the deck exhibits a lateral deformation of 30 m under wind action.

Figure 1.2 View of the Golden Gate bridge during its construction

- Second generation bridges are characterized by a streamlined box deck, similar to an air foil shape. This type of deck is very light-weight and exhibits good torsional stiffness, thanks to the closed box shape, low flexural stiffness due to the shallow depth, together with a very low wind drag. Furthermore, this type of section was considerably more economical due to the fabrication techniques that were more efficient than those used for truss girders [2]. Built in the second half of the 20th century in Europe (i.e. Severn Bridge 1966, Humber Bridge 1981, Bosforo 1973, Great East Belt 1998, Runyang 2005), the bridge main span's length could vary between 1000 m and 1600 m.

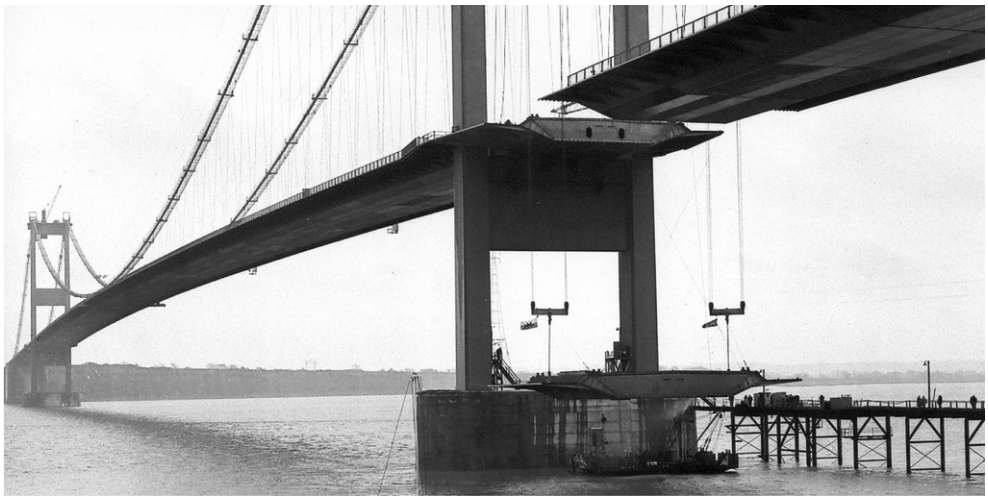

Figure 1.3 View of the Severn bridge during its construction

- The third generation was conceived with the design of the Messina Strait Bridge. This type of deck allowed to achieve lighter bridges with extremely long spans. The deck section is composed by multiple airfoil-shaped boxes, which offer a highly reduced wind resistance, and they are stable to aero-elastic instability phenomena. As of today, the longest bridge with this type of deck is the Cannakale Bridge, that reaches 2023 m, which is the longest bridge ever built, however the Messina Strait Bridge is expected to reach 3300 m.

Figure 1.4 View of the Canakkale bridge during its construction [3]

In suspension bridges the ratio between the sag of the main cable and the span length is generally set between 1/8 and 1/11. The tension in the main cable varies with the sag ratio, and in bridges where the dead load of the cables is modest compared to the deck weight and traffic loads, the cable tension will be approximately inversely proportional to the sag ratio, thus by increasing the sag, the cable tension decreases, reducing its required cross section, and an overall reduction of the quantity of cable steel, however more material will be employed to build higher towers to allow an increase of the sag.

In long span bridges, where the dead load of the cable constitutes a considerable part of the total load, the effect of increasing the sag ratio will be more pronounced as the cable tension, and therefore the cable cross section, decreases not only due the increased sag but also due to the reduced cable dead load. Moreover, the reduced self-weight of the main cables will also have a positive effect on the aerodynamic stability: the reduced ratio between the cable mass and the distributed mass across the deck will result in a more distinct separation between the vertical and torsional frequency, thus preventing flutter instability, as will be seen in the next chapters.

1.2. The Messina Strait Bridge project development

The Messina Strait Bridge is long-planned construction that will link the island of Sicily to the southern Italian mainland. The Figure 1.5 shows the geographical location and the virtual view with the proposed bridge.

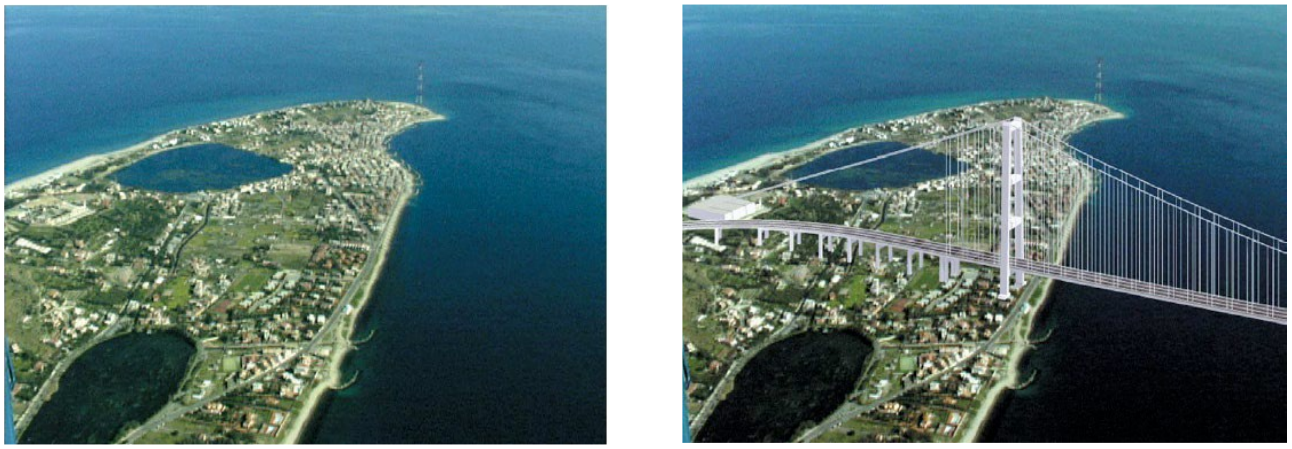

Figure 1.5 Visual impact assessment on the Sicilian side

The Messina Strait is a part of the Mediterranean Sea separating the island of Sicily on the west side from mainland Italy on the east side, and it connects the Ionian Sea with the Tyrrhenian Sea. The bridge is planned at the minimum width of the strait, and it is approximately 3 kilometres between Ganzirri in Sicily and Cannitello in Calabria. The location presents many difficulties from the morphological, seismic, and marine point of view: the strait is an active tectonic area that is directly affected by the interaction between the African and the European continental plates, as well as being characterized by a deep seabed and strong water currents.
The bridge construction had always been postponed due to its magnitude, other than political reasons among many others, like the unstable economic situation of southern Italy compared to the northern regions.

The idea of joining Calabria and Sicily existed since the Romans time, but engineering challenges due to the environmental conditions such as the depth of water, strong sea current, high winds, and seismic activities have been the main obstacles of the bridge construction.

In 1969 the Italian Ministry of Public Works issued an international design competition that attracted enormous attention, with more than a hundred proposals from designers worldwide, whom submitted a mixture of traditional and unconventional schemes. A total of 143 design were submitted and the nominated judging committee approved 75 of them. The designs ranged from single to multi-span suspension and cable-stayed bridges to three-dimensional cable networks, underground and floating tunnels, and 12 of them were awarded: 6 won an ex-aequo first prize and 6 won the second ex-aequo prize [4]. The following figures depicts the designs that won the first ex-aequo prize:

- Arch. Montuori in collaboration engineer Calini and Pavlo – Four span suspension bridge

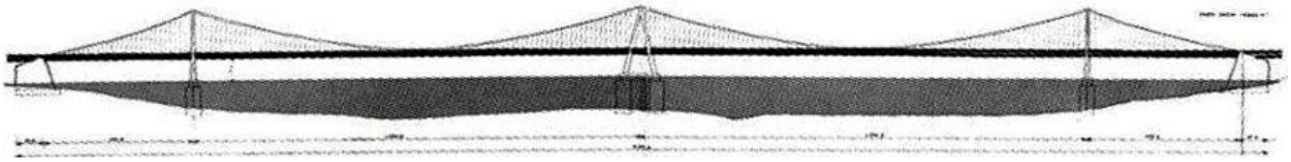

Figure 1.6 Four span bridged proposed by Arch. Montuori, engineer Calini and Pavlo

- Grant Alan and Partners, Covell and Partners, Inbucon international – Floating underwater tunnel

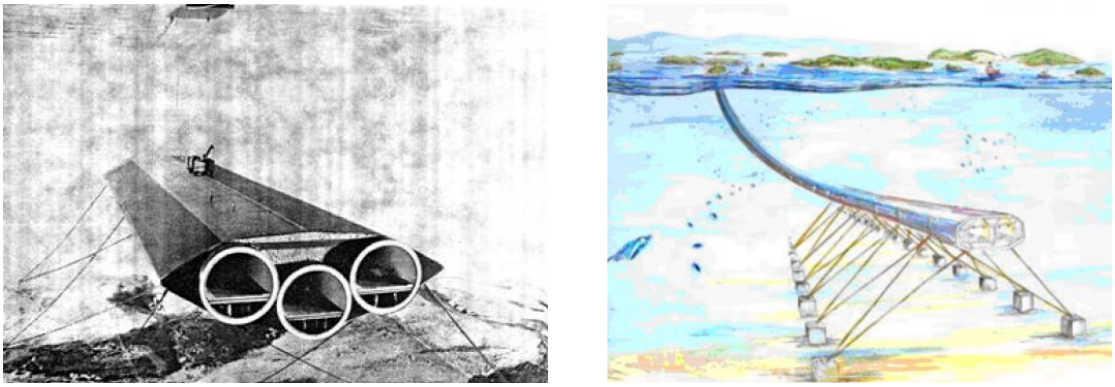

Figure 1.7 Floating underwater tunnel by Grant Alan and Partners, Covell and Partners, Inbucon international

- Lambertini Group – Three span cable stayed bridge

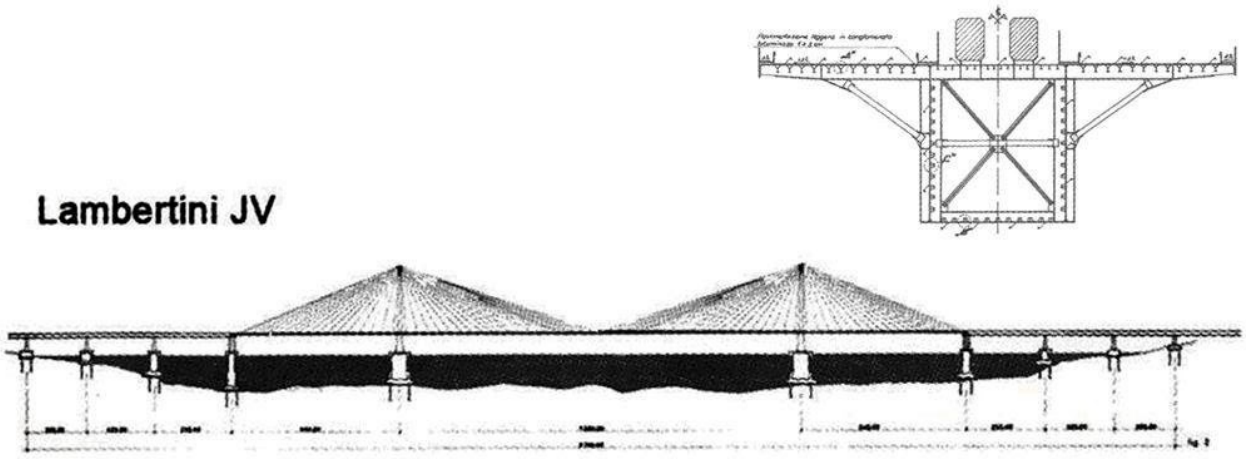

Figure 1.8 Three span stayed bridge by Lambertini Group

- Musmeci Group – Single span suspension bridge

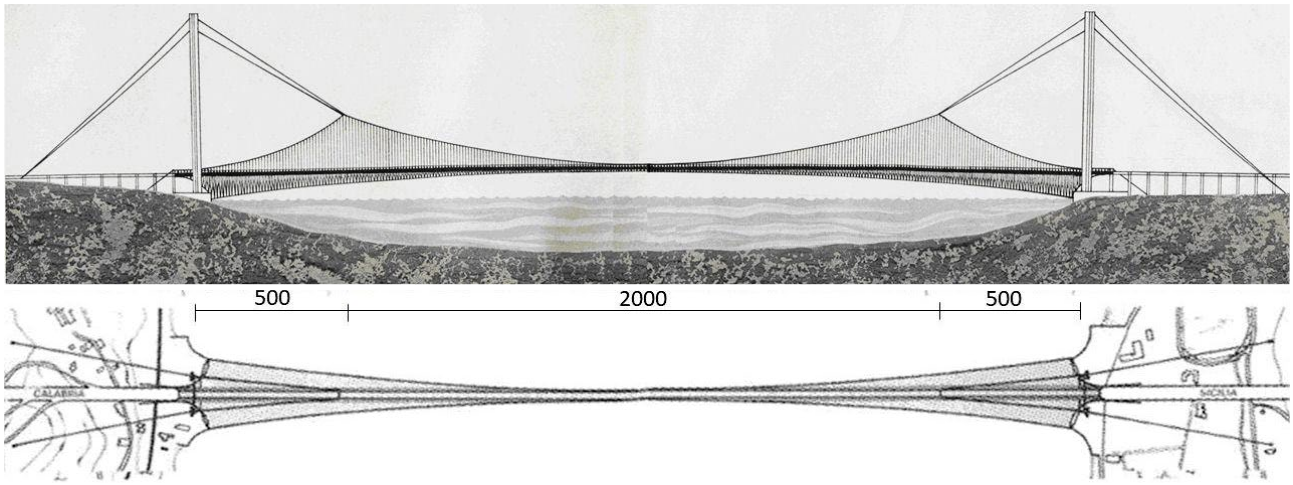

Figure 1.9 Single span suspension bridge by Musmeci Group

- Ponte di Messina Group SpA – Three span suspension bridge

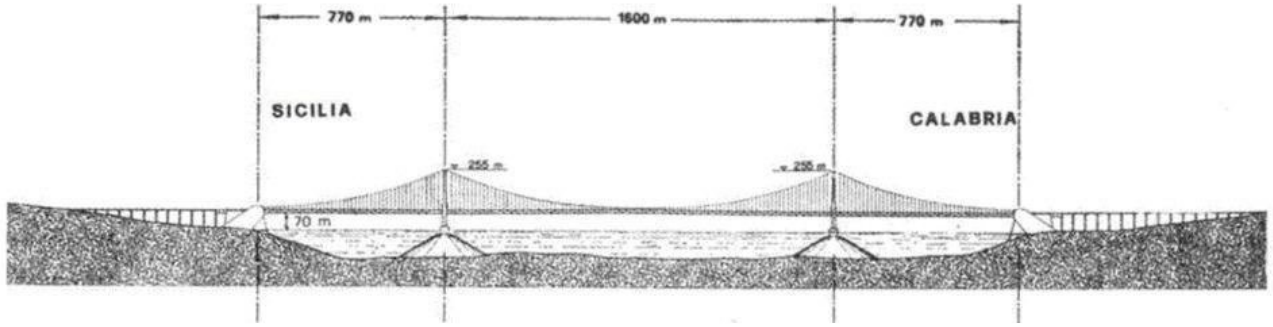

Figure 1.10 Three span suspension bridge by Ponte di Messina Group SpA

- Technital SpA – Five span suspension bridge

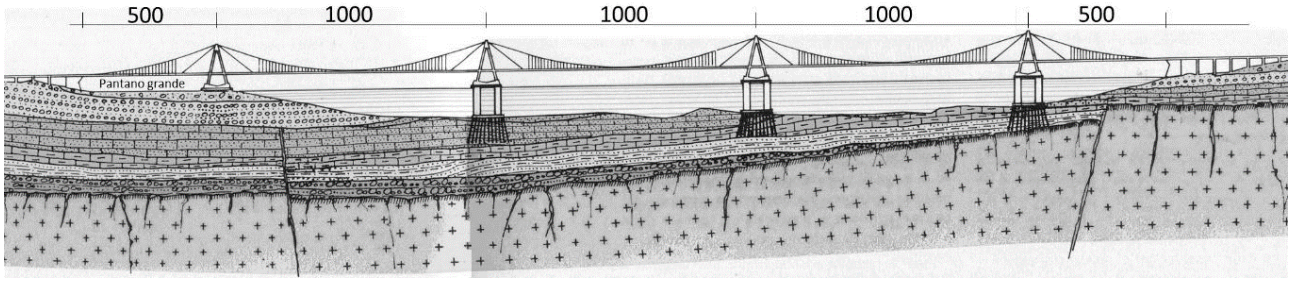

Figure 1.11 Five span suspension bridge by Technital SpA

Right after the design competition, the Ponte di Messina Group (GPM), a private company started investing considerable efforts and resources in the project, aimed at carrying out a technically founded feasibility assessment. One of the main assumptions made by GPM was that no type of tunnel solution, floating or underground, was of any possible interest, hence they focused their studies on bridge schemes only. Initially, the single span solution was considered with caution, being

too far from existing technical knowledge, but a significant contribution was brought by Dr. William C. Brown, who envisioned the first concepts of aerodynamically designed highly stable bridge decks that were going to be fully developed ten years later. His original sketches are reported in Figure 1.6 (a) and (b). The design was supported for the first time by a systematic campaign of wind tunnel tests, enabling the comparison of alternatives and providing experimental proof that was possible to achieve sufficient stability at such spans [5].

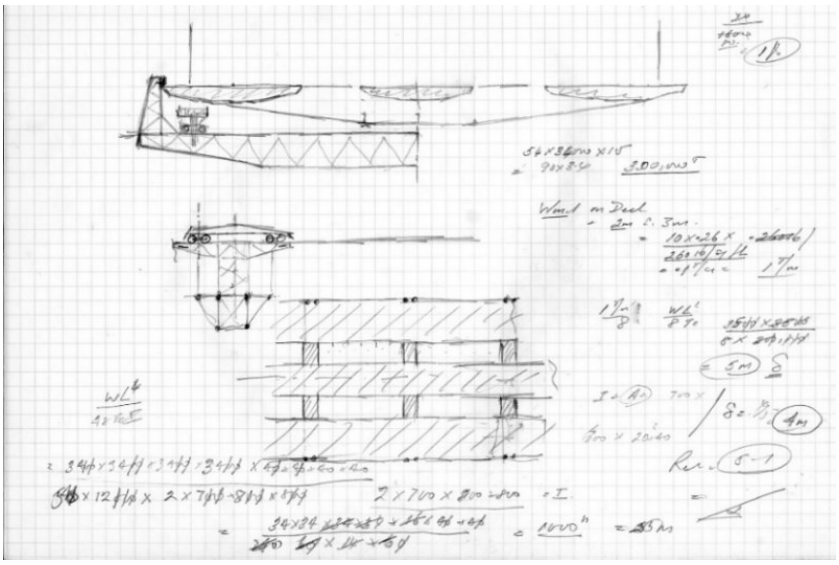

Figure 1.12 (a) Original sketches of Dr. Brown of the multi-box deck [6]

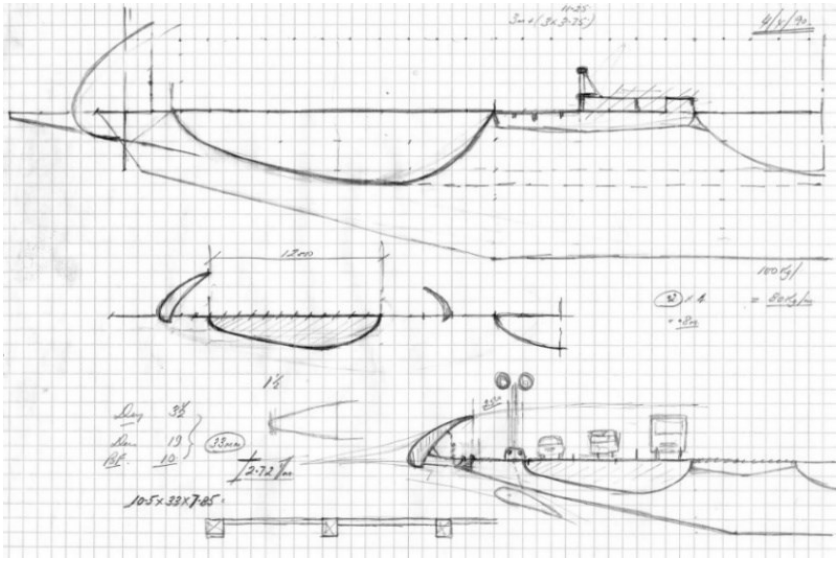

Figure 1.13 (b) Original sketches of Dr. Brown of the multi-box deck [6]

GPM concluded its activities in 1979, issuing a feasibility report that stated as feasible a two-span solution, but with uncertainties regarding the offshore foundation, and a single span solution which was the favoured one in terms of robustness and performance.

In 1981, the Italian government issued a statutory law forming the state-owned company Stretto di Messina Spa, whose task was to design, build and operate a permanent rail and road link across the Messina Strait. When they started their own survey and testing activities, they classified the proposed crossing solutions considered into three categories (Figure 1.8):

- Underground tunnels;
- Floating tunnels, whether cable-anchored at the seabed or supported by underwater piers;
- Bridges, both single and multi span.

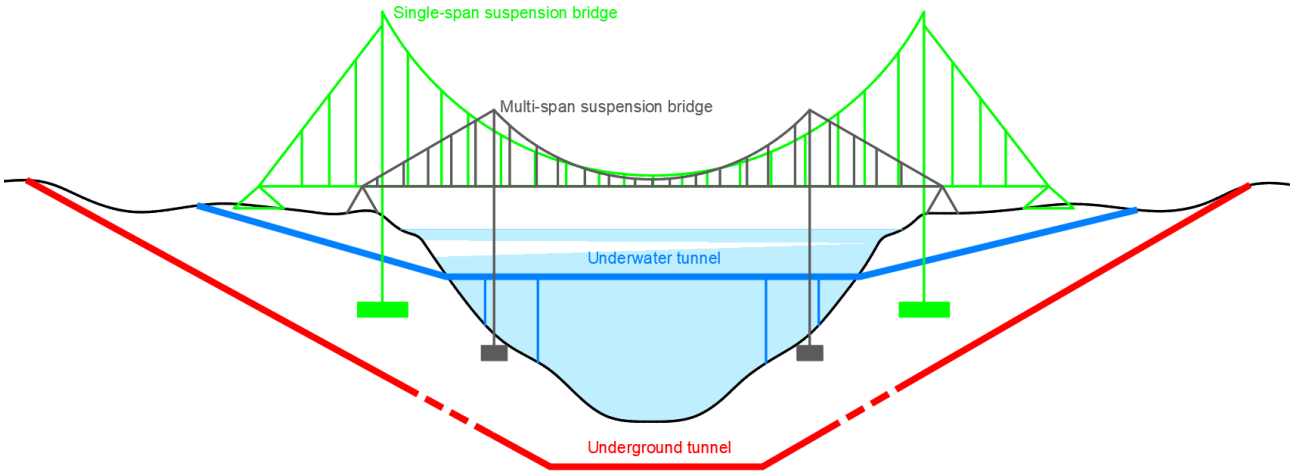

Figure 1.14 Proposed crossing solutions

Many possibilities were extensively explored until 1986, when they issued their feasibility report, whose main conclusion were:

- Underground or underwater tunnels were technically unfeasible, besides being extremely costly beyond any cost/benefit ratio of possible financial interest;
- Among all the bridge schemes, solutions with more than two spans were considered be of lower technical and financial performance, therefore only two span and single span suspension bridge schemes were considered;
- The robustness and performance of the single span solution is superior to the two-span option.

Such conclusions were analogous to those already obtained by GPM, but they were more significant due to a higher level of environmental knowledge supporting it and advanced innovative design solution.

In 2002 the preliminary design of a single span suspended bridge was finalized and approved, subsequently in 2004, Stretto di Messina Spa issued a competition to select the general contractor to carry out the final design and construction. Eurolink, a consortium led by Salini Impregilo Group, an Italian company, was awarded the bid to construct in 2005 and 5 years later they delivered the definitive design, with over 8.000 graphic papers, that were approved the following year [7]. The project manager consultant was assigned to American company Parson Transportation Group.

Eventually in 2013 the Italian government declared the liquidation the Stretto di Messina Spa and the project decayed. However, ten years later, in 2023 a decree law was approved, that re-establishes the Stretto di Messina Spa and the resumption of the executive design process of the previous project [8].

The approved design consists of a single span suspension bridge linking Cannitello in Calabria and Ganzirri in Sicily, with three roadways and one railway for each direction. It is expected to be 3666 metres long and the main span would be 3300 metres, rendering it the world longest suspended bridge. The deck, consisting of three separate boxes linked with cross beams every 30 metres, is hanged on 2 sets of dual steel cables with a diameter of 1.24 m, which drapes over two 382 metres high towers.

Figure 1.15 View of the landscape for Calabria side

Webuild SpA, formerly Salini Impregilo SpA, the group leader of the general contractor Eurolink, stated that the Messina Strait Bridge would join Italy to Europe, by means of an innovative, strategic project that is ready to be built, as soon as the contract is reinstated and updated. The executive project is expected to take 8 months, while the construction time to build the bridge will be just over 6 years.

The deck is expected to support 6.000 vehicles per hour and the passage of up to 200 trains per day, moreover the bridge is designed with a clearance of 65,5 metres, if subjected to maximum loading, while in normal operating conditions, the clearance will be around 74 metres, therefore it won't affect the maritime traffic crossing the strait.

The cost of the construction of the bridge is approximately €4,5 billion, which is about 40% of the total value of the infrastructure network that would include the bridge and all the works related to the crossing, but also the upgrade of the road and rail networks in Sicily and Calabria. On the other hand, the project is expected to boost the national GDP, and it would involve about 300 suppliers

and more than 100.000 people would be potentially employed and most of them would come from the southern part of the nation, where the unemployment rate is high [9].

Figure 1.16 View of the bridge from the deck

Although it's a "ready to be built" project, which has been tested for many years in every critical aspect, a colossal infrastructure as the designed Messina Bridge has never been constructed before, and it would be one and half time longer than the current longest bridge, the uncertainties related to the construction are one of the main reasons it hasn't been built yet. Despite this, its design has already inspired many other long span bridges, some of which are already completed or under construction, as the Canakkale bridge in Turkey, depicted in Figure 1.4.

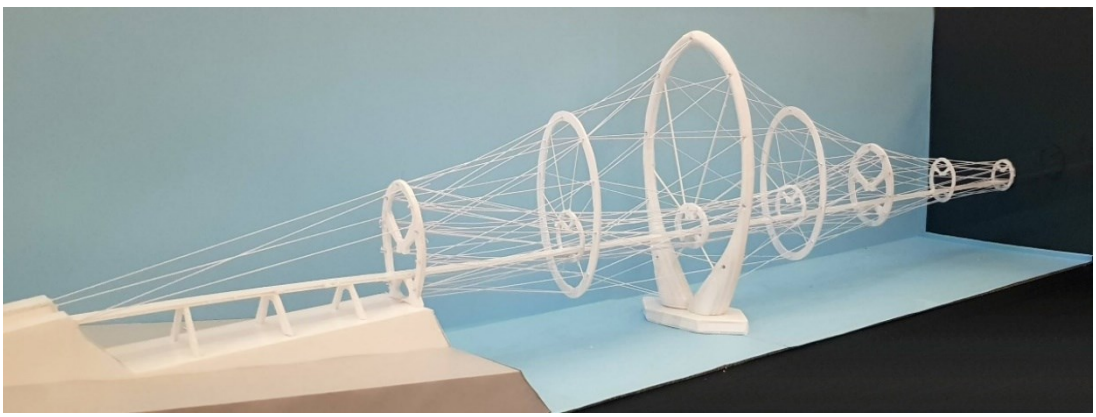

Figure 1.17 New comcept of suspension bridge

However, new designs of the bridge are still in development, that could achieve even greater distances as well as new features are designed for the current project in order to further improve the overall behaviour. For instance, Figure 1.17 and 1.18 depicts the works of engineer Peroni [10]: a new concept of suspension bridges, that could span over up to 5 kilometres and the proposal of an additional cable system, faced downwards that further anchors the deck to the ground, reducing drastically the lateral displacement [11].

Figure 1.18 Additional cable system

Chapter 2

Wind effects on long-span suspension bridges

The deck of a suspension bridges is connected to steel cables by means of a series of vertical hangers, this configuration can induce larger deck deformations (Figure 2.1). This type of structures are typically susceptible, due to their flexibility, to wind action as it might induce instability or excessive vibration in long-span bridges.

Figure 2.1 Suspension bridge scheme

Instability caused by the interaction between an air flow and an elastic structure is called *aeroelastic instability* and in the case of bridges, it includes torsional divergence, galloping, flutter and vortex-induced vibrations.
In order to avoid instabilities, the design requires that the maximum wind speed estimated at the bridge site is sufficiently lower than a critical value.
Modern designs of long-span bridge are conducted by combining experimental investigation through wind tunnel testing with computer analysis, that rely on analytical or semi-analytical models, as well as on numerical procedures, which are implemented in computer programs and usually requires parameters that are experimentally determined.

The interaction between bridge vibration and wind flow is usually idealized as being divided in two kinds of forces: motion dependent and motion independent, the former vanishes if the structure is rigidly constrained, while the latter, dependent only on the wind characteristics and section geometry, exist whether the bridge is moving or not. According to this schematization, the equation of motion in the presence of aerodynamic forces can be expressed in the following general form:

$$[M]\{\ddot{\delta}\} + [C]\{\dot{\delta}\} + [K]\{\delta\} = \{F(\delta, \dot{\delta})\}_{md} + \{F\}_{mi} \tag{2.1}$$

Where:

- [M] is the mass matrix
- [C] is the damping matrix

- [K] is the stiffness matrix
- $\{\delta\}$ is the displacement vector
- $\{F(\delta, \dot{\delta})\}_{md}$ is the motion-dependent aerodynamic force vector
- $\{F\}_{mi}$ is the motion-independent wind force vector.

Despite the fact that both motion-dependent and motion-independent forces cause deformations, aero-elastic instability is only generated by the motion-dependent part, which in short-span bridges, is insignificant and there is no concern about aeroelastic instability, while in flexible structures such as long-span bridges, both instability and vibration need to be carefully investigated.
Aeroelastic phenomena are characterized by the fact than when an elastic structure and the air flow are combined, they result in a single dynamic system with features that differ from those of the two components taken independently. Some instability phenomena, such as torsional divergence and galloping, can be treated with quasi-static approach, while flutter instability must be analysed as a fully dynamic phenomenon.

2.1. Steady aerodynamic analysis

The analysis is performed considering a static condition of the bridge with the application of plane forces in x and y directions, torque moment and steady forces, generated by the laminar flow in the deck direction. Stability is evaluated with respect to the deformed shape of the deck under wind action and its instability.

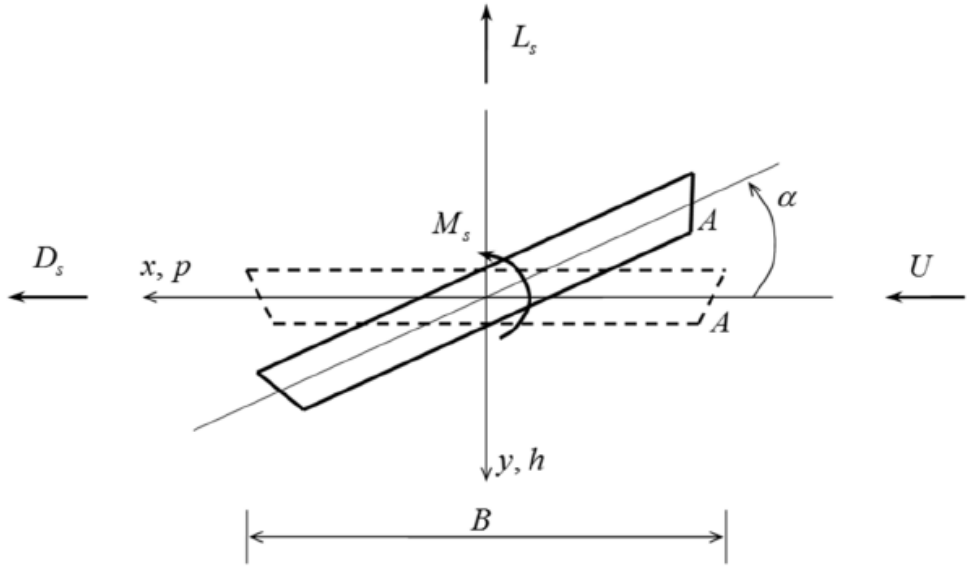

Figure 2.2 Steady aerodynamic model

Drag force in x direction, lift force in y direction and moment around z axis are determined with the following equations:

$$D_s = \frac{1}{2}\,\rho\,U^2 B\,C_D(\alpha) \tag{2.2}$$

$$L_s = \frac{1}{2}\,\rho\,U^2 B\,C_L(\alpha) \tag{2.3}$$

$$M_s = \frac{1}{2}\,\rho\,U^2 B^2 C_M(\alpha) \tag{2.4}$$

Where:

- ρ is the air density [kg/m³];
- U is the average wind speed [m/s];
- B is the deck width [m];
- C_D, C_L, C_M are the non-dimensional static aerodynamic coefficients of drag, lift and moment;
- α is the angle of attack [deg].

Aerodynamic coefficients are evaluated in wind tunnel on a scaled section, where it is possible to control the variation of α, and forces 2.2, 2.3 and 2.4 are obtained. By dividing D_s, L_s by $\frac{1}{2}\,\rho\,U^2 B$, and M_s by $\frac{1}{2}\,\rho\,U^2 B^2$ it is possible to determine C_D, C_L, C_M.

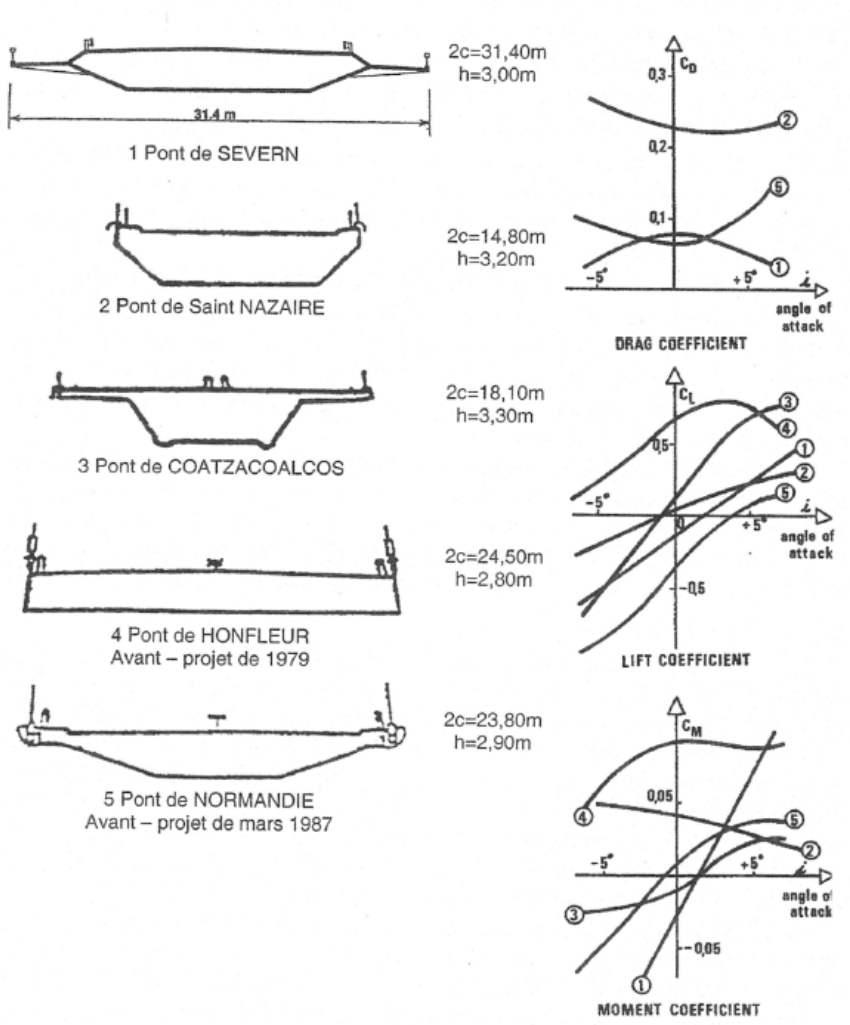

Figure 2.3 Examples of aerodynamic coefficients

For small angles of attack, the values of C_D, C_L, C_M can be linearized and then Equations 2.2, 2.3 and 2.4 become:

$$D_s = \frac{1}{2}\,\rho\,U^2 B\,C_D(0) \tag{2.5}$$

$$L_s = \frac{1}{2}\,\rho\,U^2 B\left(C_L(0) + \left(\frac{dC_L}{d\alpha}\right)\alpha\right) \tag{2.6}$$

$$M_s = \frac{1}{2}\,\rho\,U^2 B^2\left(C_M(0) + \left(\frac{dC_M}{d\alpha}\right)\alpha\right) \tag{2.7}$$

2.2. Torsional divergence

Aerostatic divergence is usually treated as a static instability, caused by the vanishing of the total stiffness (elastic plus aerodynamic) associated with the torsional mode.

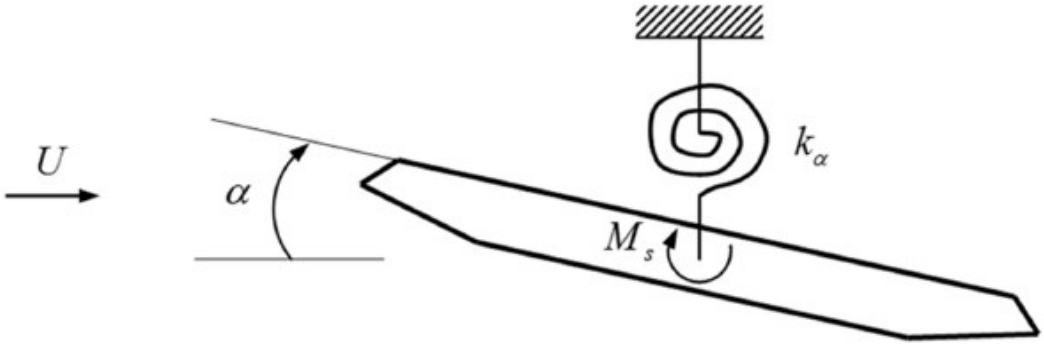

Figure 2.4 One-degree-of-freedom simplified model

Wind flowing against the structure exerts a mean pressure proportional to the square of the wind velocity and it generally induces both aerodynamic forces and moments in a structure. At a critical wind velocity, the edge-loaded bridge may buckle out of plane under the action of a drag force or torsionally diverge under a wind-induced moment that increases with the attack angle.
A simplified model to study torsional divergence considers only the deck section immersed in a two-dimensional flow in the single-degree-of-freedom system, shown in Figure 2.4. Considering a small rotation angle α, the aerodynamic moment resulting from wind, M, is given by:

$$M = \frac{1}{2}\,\rho\,U^2 B^2\,C_M(\alpha) = \frac{1}{2}\,\rho\,U^2 B^2\left[C_M(0) + \left(\frac{dC_M}{d\alpha}\right)\alpha\right] \tag{2.8}$$

Where:

- ρ is the air density [kg/m³];
- U is the average wind speed [m/s];
- B is the deck width [m];
- $C_M(\alpha)$ is the aerodynamic moment coefficient, which is a function of the angle of attack α, that can be determined by wind tunnel tests;

- $C_M(0)$ denotes the moment coefficient for the angle of attack equal to zero.

When the aerodynamic moment caused by wind exceeds the resting torsional capacity, the displacement of the bridge diverges. Equating the aerodynamic moment given by Equation 2.8 to the internal elastic moment $k\alpha$ gives:

$$k_\alpha \alpha - \frac{1}{2}\rho U^2 B^2 \left[C_M(0) + \left(\frac{dC_M}{d\alpha}\right)\alpha\right] = 0 \tag{2.9}$$

Where k_α is the spring constant of torsional stiffness. Equation 2.9 can be written as follow:

$$\left[k_\alpha - \frac{1}{2}\rho U^2 B^2 \left(\frac{dC_M}{d\alpha}\right)\right]\alpha - \frac{1}{2}\rho U^2 B^2 C_M(0) = 0 \tag{2.10}$$

The term within square brackets represents the total (elastic plus aerodynamic) torsional stiffness of the system and by equating the total stiffness to zero, the critical wind speed for torsional divergence is obtained:

$$U_D = \sqrt{\frac{2k_\alpha}{\rho B^2 \left(\frac{dC_M}{d\alpha}\right)_{\alpha=0}}} \tag{2.11}$$

The critical speed given by Equation 2.11 must be sufficiently higher than the maximum speed at the bridge site. However, it should be observed that the previous usually overestimates the torsional divergence speed compared to more sophisticated models, in which the coupling between vertical bending and torsion is taken into account.

2.3. Two-degree-of-freedom flutter

Aerostatic flutter is a dynamic instability phenomenon that originates from the mutual interaction of elastic, inertial and self-excited aerodynamic forces, therefore at a certain wind speed the structure oscillates in a divergent, destructive manner.

If a system immersed in a wind flow is given a small perturbation, its motion will either decay or diverge, depending on whether the energy extracted from the flow is smaller or larger than the energy dissipated by mechanical damping. The critical condition, which divides decay from divergent motions, occurs at wind speed called *flutter speed*, at which the motion of the structure exhibits oscillations of increasing amplitude at a constant frequency, called *flutter frequency*.

Flutter instability, originally studied in aeronautics, became of interest for bridge engineering after the collapse of the Tacoma narrows bridge in 1940, and the analyses usually performed combines both experimental and analytical procedures. The analysis aims to determine the lowest wind speed that initiates instability on the proposed bridge deck configuration, which should be sufficiently higher than meteorological expected wind speeds at the bridge site.

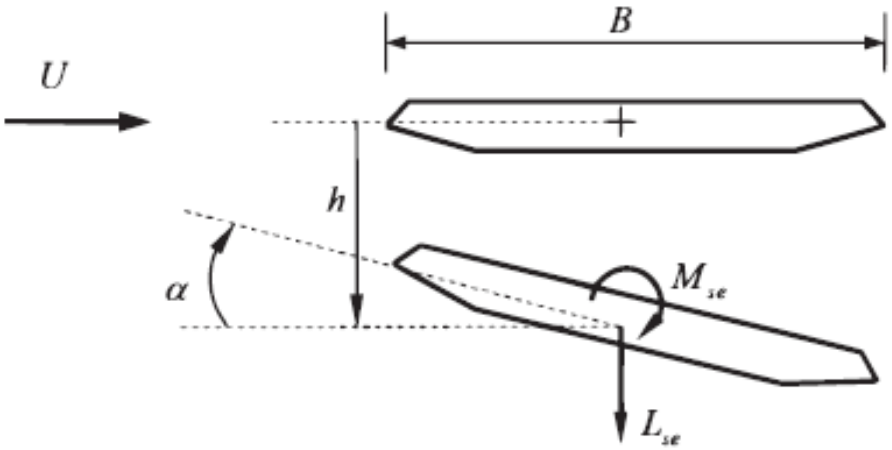

Figure 2.5 Two-degree-of-freedom simplified model

Figure 2.5. shows the self-excited aerodynamic forces acting on a deck which is subjected to a constant wind flow U, and in this two-degree-of-freedom simplified model only the vertical deflection h and the torsional rotation α are considered.

A closed-form expression for the unsteady aerodynamic forces acting on the oscillating bridge decks cannot be obtained. To solve the problem, Scanlan and Tomko proposed a semiempirical model, based on the so-called *flutter derivatives* that are experimentally determined in wind tunnels. The self-exciting forces can be assumed as linear functions of structural displacements and velocities, parametrically dependent on the *reduced frequency of oscillation* K:

$$L_{se}(t,K) = \frac{1}{2}\rho U^2 B\left[KH_1^*(K)\frac{\dot{h}(t)}{U} + KH_2^*(K)\frac{B\dot{\alpha}(t)}{U} + K^2H_3^*(K)\alpha(t) + K^2H_4^*(K)\frac{h(t)}{B}\right] \quad (2.12)$$

$$M_{se}(t,K) = \frac{1}{2}\rho U^2 B^2\left[KA_1^*(K)\frac{\dot{h}(t)}{U} + KA_2^*(K)\frac{B\dot{\alpha}(t)}{U} + K^2A_3^*(K)\alpha(t) + K^2A_4^*(K)\frac{h(t)}{B}\right] \quad (2.13)$$

Where

$$K = \omega B/U = 2\pi f B/U \quad (2.14)$$

- B is the deck width
- ω is the angular frequency of oscillation
- U is the undisturbed mean wind speed

The coefficients H_i^* and A_i^* $(i = 1-4)$ are the flutter derivatives, functions of the reduced frequency of oscillation K, as well as the mean angle of attack. The coefficients that multiply generalized displacements are intended as aerodynamic stiffness, while those which multiply generalized velocities represents aerodynamic damping. Equations 2.12 and 2.13 do not explicitly include additional mass terms in $\ddot{h}$ and $\ddot{\alpha}$, which are considered to be negligible in wind engineering applications.

The flutter derivatives are usually plotted as a function of the *reduced velocity*:

$$U_r = \frac{U}{fB} = \frac{2\pi}{K} \tag{2.14}$$

In a flutter analysis, only the onset instability condition is normally exanimated for the design of bridge structures. Under the assumption of small oscillations perturbating the flow, the structure can be modelled as a damped linear oscillator with two-degree-of-freedom:

$$m\ddot{h}(t) + c_h\dot{h}(t) + k_h h(t) = L_{se}(t, K) \tag{2.15}$$

$$I\ddot{\alpha}(t) + c_\alpha\dot{\alpha}(t) + k_\alpha\alpha(t) = M_{se}(t, K) \tag{2.16}$$

Where:

- h and α are the vertical bending and the torsional angle
- m and I are the mass and the polar mass moment of inertia per unit length
- c_α and c_h are the mechanical damping coefficients
- k_h and k_α are the stiffness in the heaving and pitching modes, respectively
- L_{se} and M_{se} are the self-excited lift and moment per unit length, depending on time *t* and on the deck oscillation through K

In classical flutter, also known as coupled or stiffness-driven flutter, the two modes coalesce into a single flutter frequency that originates a motion which introduces energy into the system, leading to divergent or large-amplitude oscillations. Considering a harmonic solution to Equations 2.12 and 2.13 in the form:

$$h(t) = h_0 e^{\omega t} \tag{2.18}$$

$$\alpha\ t\ = \alpha_0 e^{\omega t} \tag{2.19}$$

and imposing the system complex determinant to zero, after separating the real and the imaginary part, a fourth degree and a third degree polynomial equations are obtained, with respect to the reduced frequency of oscillation, the common solution of which gives the critical reduced frequency for flutter K_F.

The frequency ω_F that simultaneously satisfies both polynomial equations is the flutter frequency. Therefore, the flutter speed can be obtained as:

$$U_F = \frac{B\omega_F}{K_F} \tag{2.20}$$

If more than one intersection point is found in the selected range of K, the lowest U_F is the required solution.

Alternatively, the flutter speed can be calculated with the eigenvalues $\omega_n = \omega_{r,n} + i\omega_{i,n}$ (n = 1,2,3 ...) of the system, by increasing the wind speed until the real part of an eigenvalue, which is related to damping, until it reaches a positive value. The imaginary part of the same eigenvalue represents the flutter frequency.

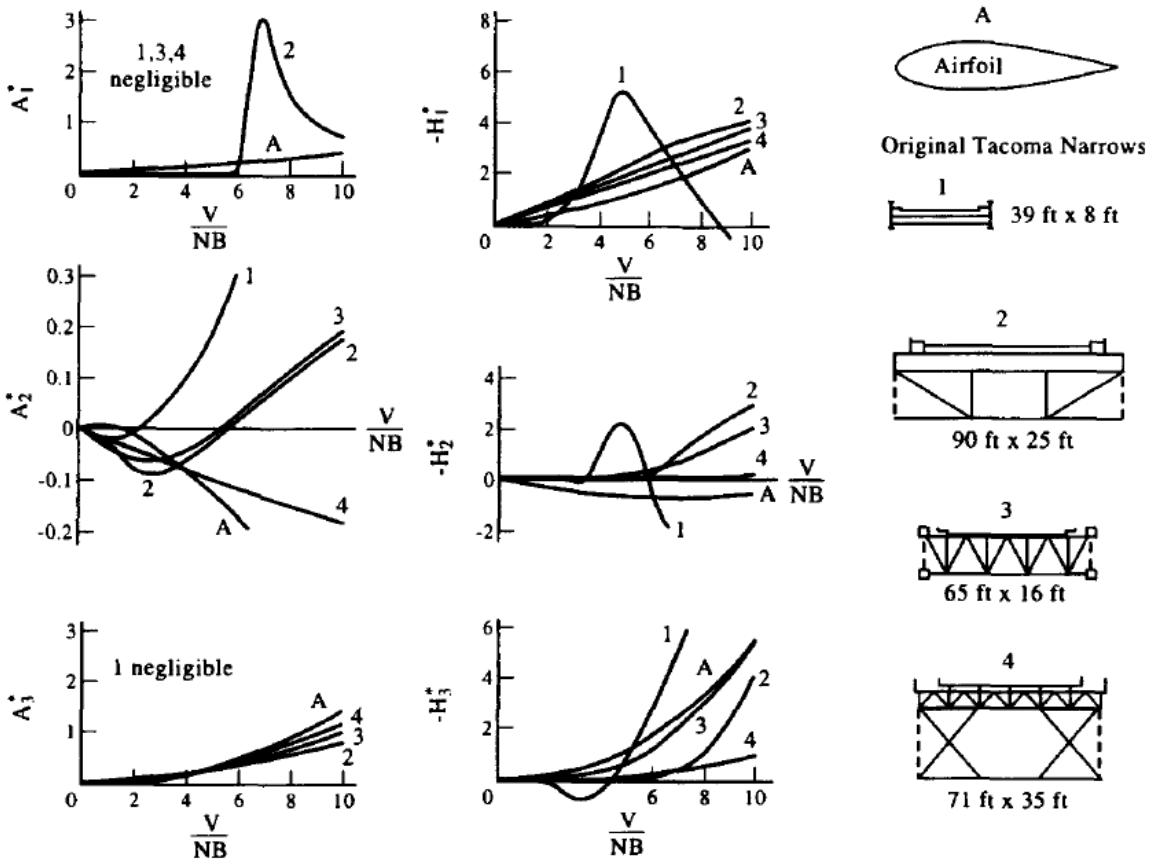

Figure 2.6 Examples of flutter derivatives [12]

2.4. Three-degree-of-freedom flutter

Although the simplified representation of the bridge deck response with only two-degree-of-freedom yields excellent results, in very long span bridges, therefore more flexible, the lateral (sway) component of the motion cannot be neglected, and it may be relevant for flutter instability.

Several studies have been made to estimate the influence of the motion induced drag on the critical wind speed. More precisely, it has been assessed that it becomes significant for main spans longer than 1500 metres. The influence of lateral components is studied in Section 6.5.

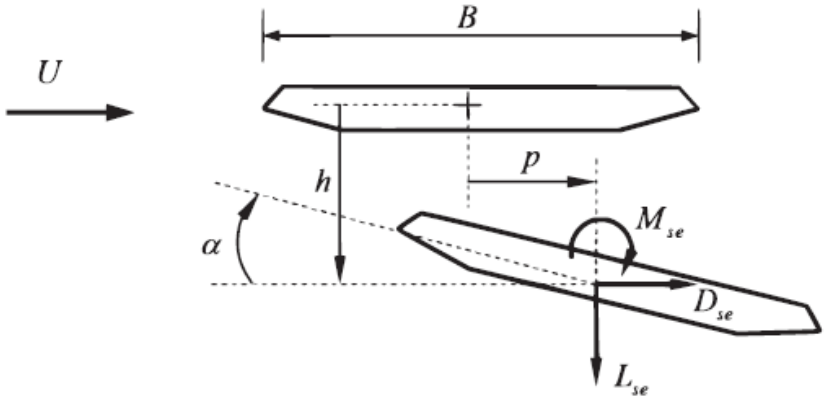

Figure 2.7 Three-degree-of-freedom simplified model

By taking into account the along-wind force and displacement, the general expression of the self-excited forces in matrix form for a finite element analysis becomes:

$$\begin{Bmatrix} L_{se} \\ D_{se} \\ M_{se} \end{Bmatrix} = \frac{1}{2}\rho U^2 B \left(\begin{bmatrix} \frac{K^2 H_4^*}{B} & \frac{K^2 H_6^*}{B} & K^2 H_3^* \\ \frac{K^2 P_6^*}{B} & \frac{K^2 P_4^*}{B} & K^2 P_3^* \\ K^2 A_4^* & K^2 A_6^* & K^2 A_3^* B \end{bmatrix} \begin{Bmatrix} h \\ p \\ \alpha \end{Bmatrix} + \begin{bmatrix} \frac{K H_1^*}{U} & \frac{K H_5^*}{U} & \frac{K H_2^* B}{U} \\ \frac{K P_5^*}{U} & \frac{K P_1^*}{U} & \frac{K P_2 B}{U} \\ \frac{K A_1^* B}{U} & \frac{K A_5^* B}{U} & \frac{K A_2^* B^2}{U} \end{bmatrix} \begin{Bmatrix} \dot{h} \\ \dot{p} \\ \dot{\alpha} \end{Bmatrix} \right)$$
$$= \frac{1}{2}\rho U^2 B \left([F_d]\{q\} + \frac{1}{U}[F_v]\{\dot{q}\} \right) \quad (2.21)$$

Where:

- $L_{se}, D_{se}\ and\ M_{se}$ are the self-excited lift force, drag force and pitch moment, respectively;
- $h, p\ and\ \alpha$ are the displacements at the centre of the deck section in the directions corresponding to $L_{se}, D_{se}\ and\ M_{se}$, respectively;
- $H_i^*, P_i^*\ and\ A_i^*$ $(i = 1 - 6)$ are the generalized derivatives;
- $[F_d]\ and\ [F_v]$ are the flutter derivatives matrices corresponding to displacement and velocity, respectively.

In liner analysis, the general aeroelastic motion equations of bridge system are expressed in terms of the generalized modal coordinate vector $\{\delta\}$:

$$[M]\{\ddot{\delta}\} + \left([C] - \frac{1}{2}\rho U^2 B[C^*]\right)\{\dot{\delta}\} + \left([K] - \frac{1}{2}\rho U^2 B[K^*]\right)\{\delta\} = \{0\} \quad (2.22)$$

Where $[M], [C]\ and\ [K]$ are the generalized mass, damping and stiffness matrices, respectively, and $[C^*]\ and\ [K^*]$ are the generalized aerodynamic damping and aerodynamic stiffness matrices, respectively.

Matrices $[M], [C]\ and\ [K]$ are derived in the same way as in the classical dynamic analysis, while matrices $[C^*]\ and\ [K^*]$, corresponding to $[F_v]\ and\ [F_d]$ in Equation 2.21, respectively, are assembled from local aerodynamic forces.

By assuming harmonic oscillation in the form $\{\delta\} = \{\delta_0\}e^{i\omega t}$, the following characteristic problem is obtained:

$$\left(-\omega^2[M] + i\omega\left([C] - \frac{1}{2}\rho U^2 B[C^*]\right) + [K] - \frac{1}{2}\rho U^2 B[K^*]\right)\{\delta_0\} = \{0\} \quad (2.23)$$

The flutter speed U_F and the flutter frequency ω_F can be derived from the nontrivial solution of Equation 2.23, which is given by the following condition:

$$det\left(-\omega^2[M] + i\omega\left([C] - \frac{1}{2}\rho U^2 B[C^*]\right) + [K] - \frac{1}{2}\rho U^2 B[K^*]\right) = 0 \quad (2.24)$$

2.5. The single-mode criterion

Relevant for bridges is also single-degree-of-freedom flutter, referred also as damping-driven flutter, wherein negative damping in a single mode can be attained without any coupling with other modes. This form physically interprets the onset of flutter as the wind velocity that produces enough negative aerodynamic damping to offset the bridge's own mechanical damping.
A preliminary judgement on the flutter behaviour of the section can be made by examining the flutter derivatives, which could be modified in order to eliminate the positive flutter derivatives as shown in Figure 2.6, especially A_2^* and H_1^*, since they govern torsional flutter and vertical flutter.
If, among the aerodynamic damping terms, only those associated with A_2^* and H_1^* are considered significant, the total structural plus aerodynamic damping can be written as:

$$c_{h,tot} = c_h - \frac{1}{2}\rho UBKH_1^*(K) \tag{2.25}$$

$$c_{\alpha,tot} = c_\alpha - \frac{1}{2}\rho UB^3KA_2^*(K) \tag{2.26}$$

For vertical and torsional degree of freedom, respectively.
For the air foil, A_2^* and H_1^* are both negative for every value of K, therefore, the total damping is always positive for both h and α. It can be concluded that, in an incompressible flow, the air foil isn't subjected to single-degree-of-freedom flutter in a vertical or torsional mode; that is, the critical mechanism always involves a coupling between these two modes (classical flutter instability).

Dedicated numerical procedure, allows to solve Equation 2.23 efficiently, such as the pK-F method, developed by A.Namini and P.Albrecth [13]. The single-mode criterion expressed by Equations 2.25 and 2.26, can also be applied in Finite Element Framework, as illustrated in [14] and [15].

Moreover, Scanlan (1987) [16] and Scanlan and Jones (1990) [17], introduced a single-mode criterion for a generic multi-degree-of-freedom system employing only the aerodynamic damping terms H_1^*, P_1^* and A_2^* and in addition the stiffness term in A_3^*:

$$H_1^*(\bar{K})G_{hi} + P_1^*(\bar{K})G_{pi} + A_2^*(\bar{K})G_{\alpha i} \geq \frac{4\xi_i I_i}{\rho B^4 L_d}\frac{\omega_i}{\bar{\omega}_i} \tag{2.27}$$

Where

$$\bar{\omega}_i = \omega_i\left[\frac{1}{1 + \frac{\rho B^4}{2I_i}A_3^*(\bar{K})G_{\alpha i}}\right]^{1/2} \tag{2.28}$$

And

$$\bar{K}_i = \frac{B\bar{\omega}_i}{U} \tag{2.29}$$

Chapter 3

Aeroelastic studies of the Messina Bridge project

After the publication of the Messina Strait Bridge project many research groups started testing it, focusing especially on aerostatic instabilities, caused by the interaction between an air flow and an elastic structure, tin order to prevent dangerous conditions or even worse, the collapse of the whole structure, such as the Tacoma Narrows bridge disaster in 1940.
Investigations usually begin with the development of a finite element model of the bridge to analyse its behaviour under wind actions, with particular attention towards flutter, then a modal analysis is carried out to determine the natural frequencies and the vibrations modes. Subsequently, the flutter analysis, based on the flutter derivatives, that can be extracted in wind tunnel tests on spring mounted scaled models of the bridge. The flutter analysis is performed for each of the modes considered, and the flutter instability occurs when the structural damping of one of these modes becomes null. The corresponding wind speed is called *flutter velocity* and any increment of the wind velocity from this point will increase the vibrations exponentially.

Due to magnitude and relevance of the Messina Strait Bridge, many research groups have published their studies, and two of them will are presented in this thesis:

- Prof. G. Diana *et al.* of Politecnico di Milano [18];
- Prof. J. A. Jurado *et al.* of University of A Coruña [19];
- Prof. P. D'Asdia (Univeristà degli Studi di Trieste) and Prof. V. Sepe (Università degli Studi di Roma "La Sapienza") [20].

3.1. Diana *et al.* studies

Their studies are based on the 1992 bridge design, and its lateral view and cross section are reported in Figure 3.1 and Figure 3.2:

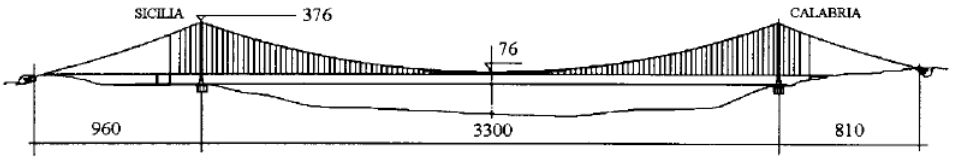

Deck mass	24300 kg/m	Global cable tension	267200 t
Cable mass	32000 kg/m	Tower height	376 m

Figure 3.1 Messina strait bridge project main features

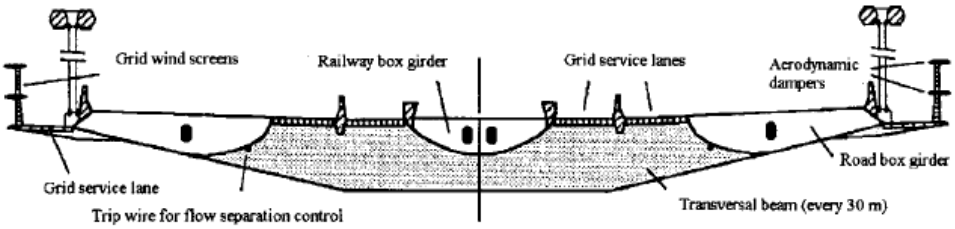

Figure 3.2 Deck design

Due to the relevance of the Messina Strait Bridge project, it has been possible to perform many kinds of test, comparing results of section models at different scales with those obtained on a full scale aeroelastic model and with several numerical simulations: in the end a final verification has been performed on a real bridge, the Humber Bridge.

The flow chart of Figure 3.3 summarizes the main aspects of the research: it started with a wind tunnel test on a 1:87 scale section model (block 6, Figure 3.3). The output of this first step mainly consists of two information: the static loads and the self-exciting loads, linked to the relative motion between the wind and the structure.

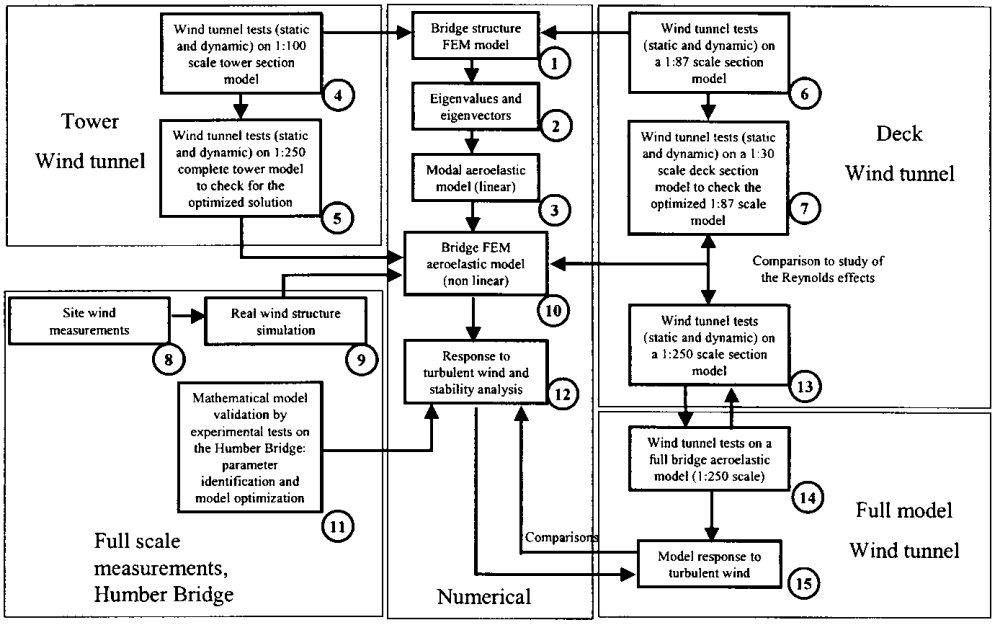

Figure 3.3 General layout of the research

Hence it is possible to assess the stability, through simple one or two-degree-of -freedom model: if the cross section is stable, the whole structure will be stable too, being just an extrusion in the third dimension of the considered section model. At this stage it is also possible to perform a design optimization in order to improve the aerodynamic performances, being the section model is easily modifiable.

Moreover, at this stage it is already possible to estimate the flutter instability velocity, around 62 m/s, but experimental testing and numerical simulation have found out that this instability is well beyond this limit, fixed around 80 m/s, unfortunately a more precise flutter velocity hasn't been published yet.

The table below reports the structural frequencies obtained from the numerical modelling:

	frequency [Hz]	Mode of vibration
I	0.033	first horizontal (symmetric)
II	0.059	second horizontal (non symmetric)
III	0.061	first vertical (non symmetric)
IV	0.080	first-third vertical (symmetric)
V	0.081	first torsional (non symmetric)
VI	0.084	first-third horizontal (symmetric)
VII	0.093	first axial
IX	0.097	first-third torsional (symmetric)
X	0.103	second horizontal cables (symmetric)
XII	0.107	third vertical (symmetric)
XIII	0.116	first-third horizontal cables (symmetric)
XIV	0.128	fourth vertical
XV	0.129	third torsional

Table 3.1 Natural frequencies

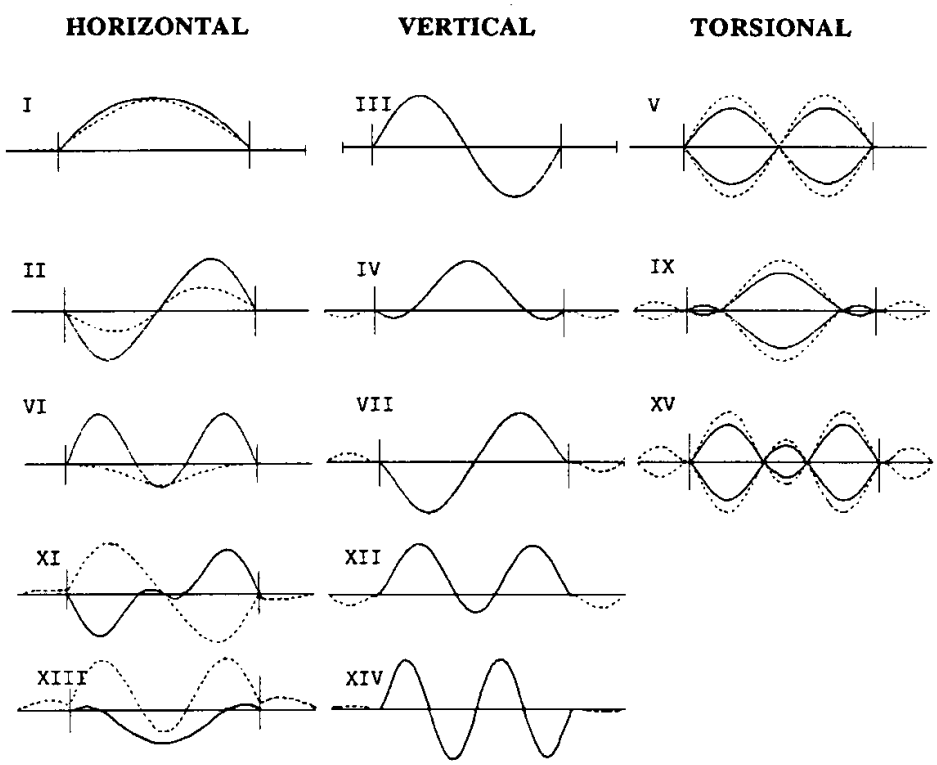

Figure 3.4 Vibration modes

After the optimization loop has been completed, further tests have been carried out on the best behaving deck section, with a bigger model (1:30 scale), however, despite Politecnico di Milano preferred an easy-to-handle 2D section model rather than a 3D complete one, the project's magnitude required further verifications on a 3D full bridge aeroelastic model.
At that time no wind tunnel was suitable for that kind of testing, was available in Italy, so an agreement with the Danish Maritime Institute (DMI) of Copenhagen has allowed several months of testing on a 1:250 scale model (block 14, 15, Figure 3.3).

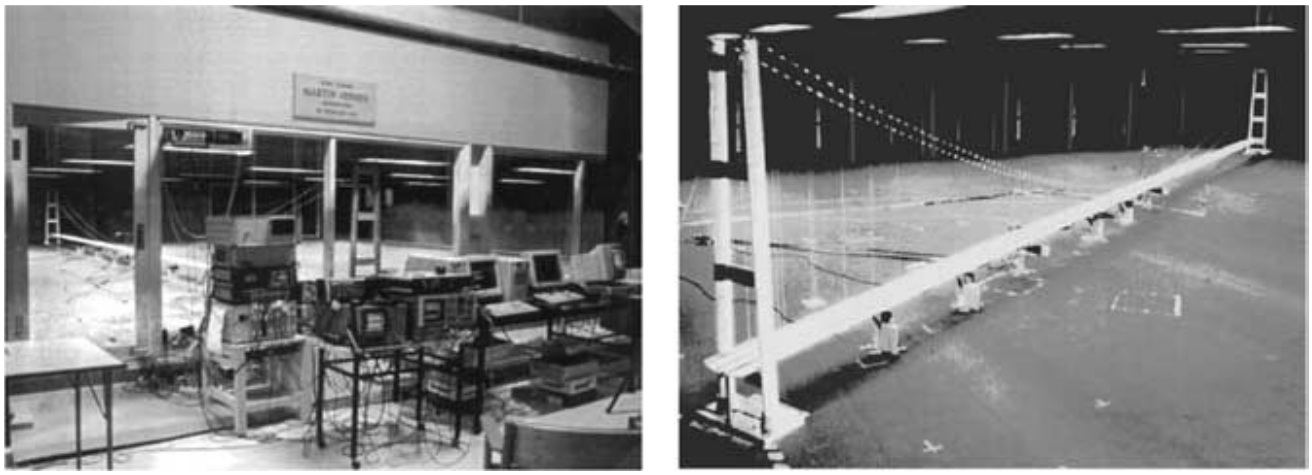

Figure 3.5 Aeroelastic full bridge model (1:250 scale)

The adopted model reproduces the real bridge dynamic behaviour, taking into consideration lateral, torsional and vertical stiffness, the results are reported in Table 3.2, which shows how the similar achievement means a good agreement between the prototype and model dynamic features; the only critical issue is the modal damping, as for real structures the structural damping tends to increase for higher modes, while the model shows a opposite trend.

		Real bridge natural frequencies (Hz)	Model nat. freq. target (Hz)	Model nat. freq. measured (Hz)	Non dimension damping % of critical
Lateral 1	Sym	0.033	0.52	0.52	0.4
Lateral 2	Asym	0.059	0.93	0.97	0.4
Vertical 1	Asym	0.061	0.97	1.03	1
Vertical 2	Sym	0.08	1.27	1.35	1
Torsional 1	Asym	0.081	1.28	1.45	1
Lateral 3	Sym	0.084	1.33	1.37	
Vertical 3	Asym	0.093	1.47		
Torsional 2	Sym	0.097	1.53	1.7	0.5
Vertical 4	Sym	0.107	1.69	1.9	0.7
Lateral 4	Asym	0.107	1.69	1.7	
Lateral 5	Sym	0.116	1.83		
Vertical 5	Sym	0.129	2.04	2.1	0.7
Torsional 3	Asym	0.129	2.04	2.3	0.5

Table 3.2 Dynamic verification on the 1:250 full bridge aeroelastic model

In addition, Figure 3.6 reports the variation of first vertical and the first torsional mode frequency with increasing wind speed, and since the stiffness-driven flutter occurs when these frequencies coalesce. At the design wind speed of 62 m/s the bridge still exhibits a stable behaviour, as the two frequencies are still distinct.

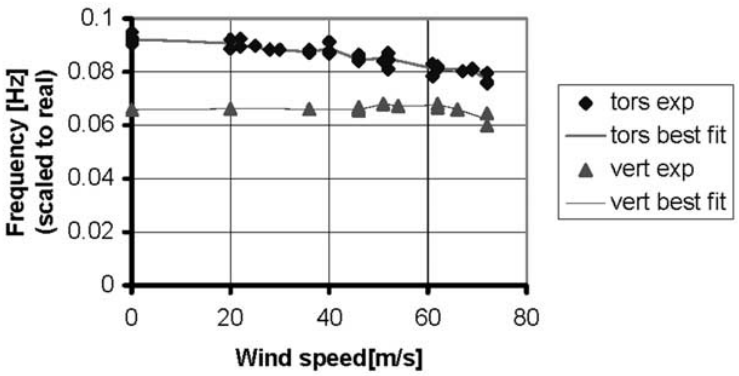

Figure 3.6 Vertical and torsional frequency variation

3.2. Jurado *et al.* studies

These studies are performed by a hybrid approach that consists of an experimental phase and a subsequent computational phase. The aim is to find out the value of flutter wind speed and during the design phase it must be verified that it's higher that the extreme wind estimated at the location of the bridge.

A finite element model of the entire bridge (Figure 3.7) was developed in ABAQUS, consisting of 2913 elements with 12,528 degrees of freedom and the geometrical and mechanical properties are summarized in Table 3.3:

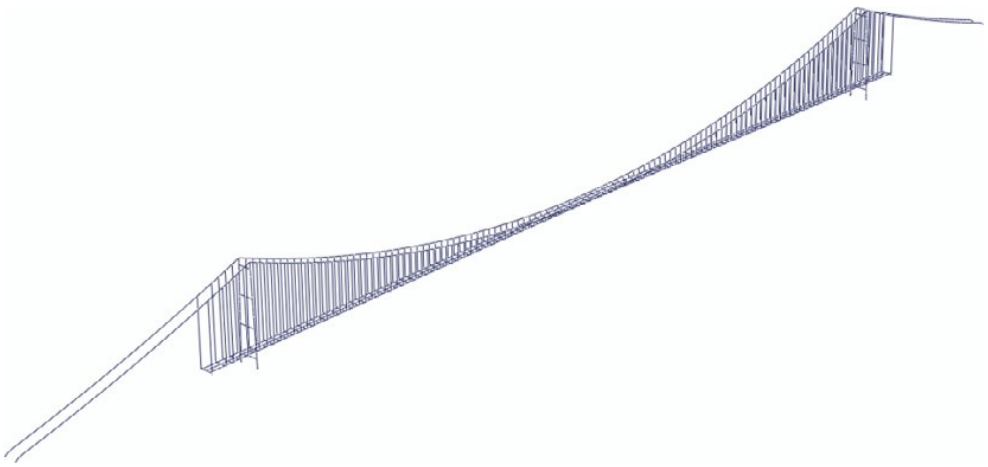

Figure 3.7 Finite element model of the Messina Bridge

Total deck length (m)	3666
Central span length (m)	3300
Lateral span length (m)	183
Distance between tower-anchorage, Sicily side (m)	960
Distance between tower-anchorage, Calabria side (m)	810
Total deck width (m)	61.13
Central box area (m)	0.341
Central box moment of inertia, I_y (m^4)	0.286
Central box moment of inertia, I_z (m^4)	1.847
Central box polar moment of inertia, J (m^4)	0.653
Central box mass per unit length of deck (t/m)	7.85
Lateral box area (m)	0.645
Lateral box moment of inertia, I_y (m^4)	0.623
Lateral box moment of inertia, I_z (m^4)	11.018
Lateral box polar moment of inertia, J (m^4)	1.375
Lateral box mass per unit length of deck (t/m)	12.5
Non-structural mass per unit length of deck (t/m)	4.37

Table 3.3 Geometrical and mechanical properties FE model

The modal analysis was carried out in two steps due to the large flexibility of the structure. Firstly, the initial stresses in main cables and hangers were calculated under self-weight, and then the modal analyses were performed with the corresponding overall stiffness of the bridge. Table 3.4 summarize some of the natural frequencies of the Messina bridge reported in Kusano's studies [21], being the more recent publication of J. A. Jurado *et al.*, and the comparison to Diana *et al.* data [18].

Mode	Type	Freq (Hz)	
		Kusano	Diana
1	LS	0.0309	0.033
2	LA	0.0573	0.059
3	VA	0.0606	0.061
4	VS	0.0811	0.080
5	LS	0.0860	0.084
6	TA	0.0868	0.081
7	VA	0.0925	0.093
8	VS	0.0980	
9	TS/LA	0.1032	0.097
10	VA	0.1033	
11	LA	0.1042	
12	VS	0.1078	0.107
13	LS	0.1142	
14	VA	0.1279	0.128
15	LA	0.1347	
16	TS/LA	0.1356	0.129
17	VS/LA	0.1448	
18	LA	0.1461	
19	VS	0.1565	
20	VS	0.1586	
21	VS	0.1603	
22	VS	0.1620	
23	LA/TA	0.1658	
24	VS	0.1678	
25	VA	0.1734	

Table 3.4 Natural frequencies of the Messina Bridge

The eighteen flutter derivatives of the numerical example were extracted from the bridge sectional model (1:100 scale) test carried out in the wind tunnel at the University of A Coruña (Spain), and they are reported in Figure 3.9:

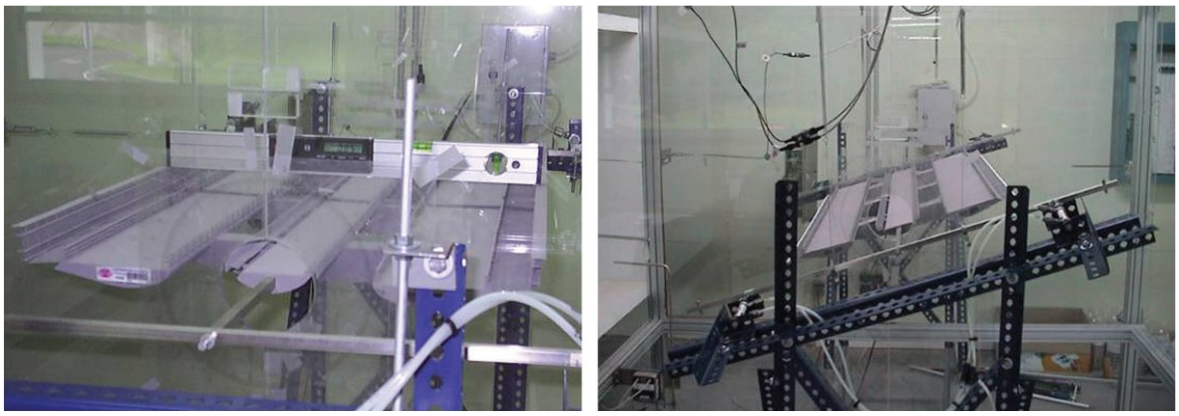

Figure 3.8 Wind tunnel testing of the Messina bridge deck

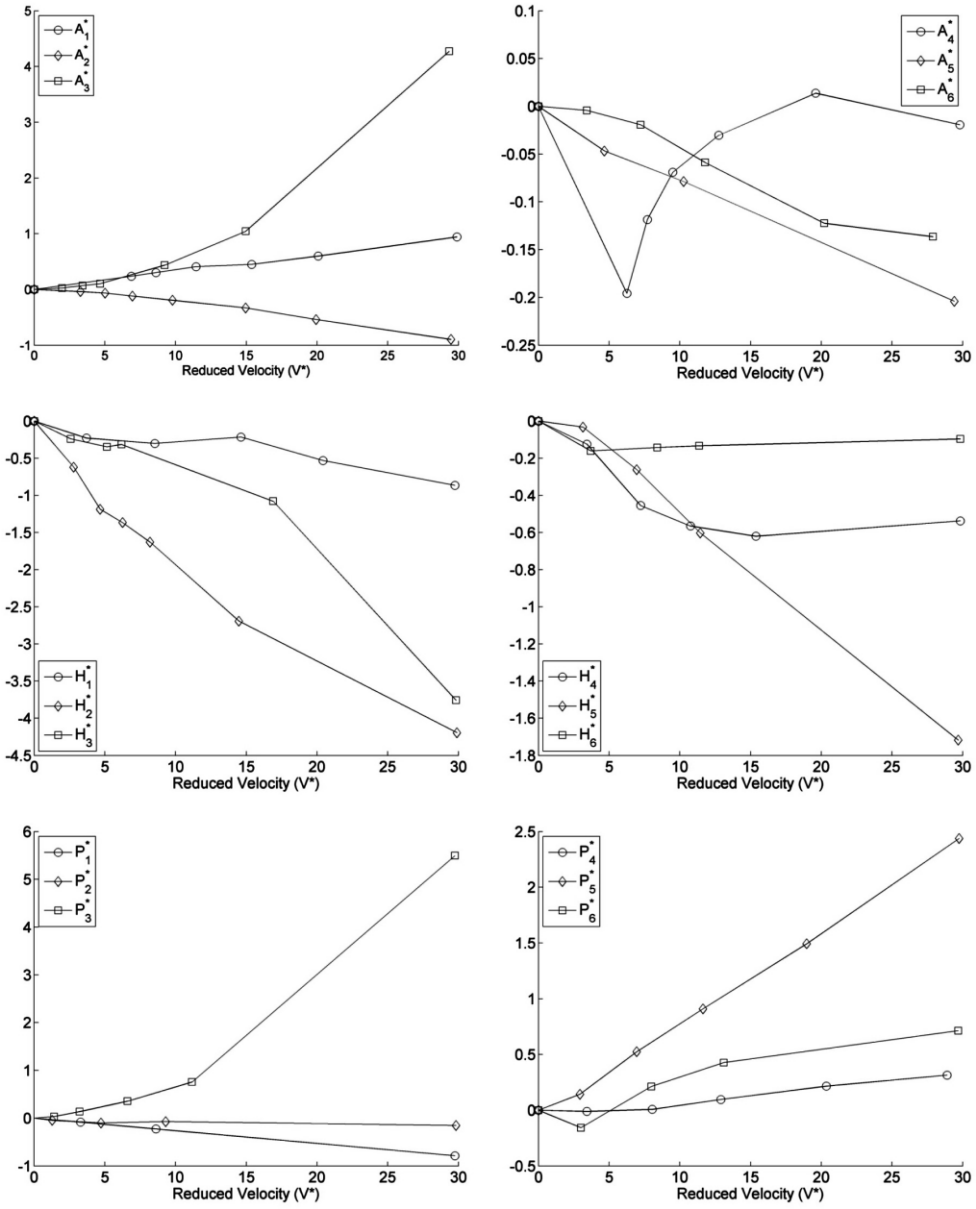

Figure 3.9 Flutter derivatives of Messina Bridge

Then, the FLAS code, developed by the University of A Coruña, was employed to compute flutter velocity using the natural frequencies and mode shapes of the bridge obtained in the modal analysis as well as other basic information of the bridge such as span length, number of elements in each span, aeroelastic modes to consider as well as structural damping.

The seven most relevant modes, 1, 2, 3, 4, 5, 6 and 11 (Figure 3.10) were considered, and the results are shown in Figure 3.13. The top half of the graph shows the evolution of negative alpha values vs. wind velocity, which are related to the damping of the structure.

Flutter occurs when the alpha value of the torsional mode goes from negative to positive, which is a point of null structural damping at the wind speed of 102.72 m/s. Any increment of wind velocity from this point will increase the vibration exponentially.

The bottom half is the evolution of beta values, which are related to frequencies of the structure. The frequency of the mode 6 gradually decreases as flutter occurs at the reduced frequency of 0.246.

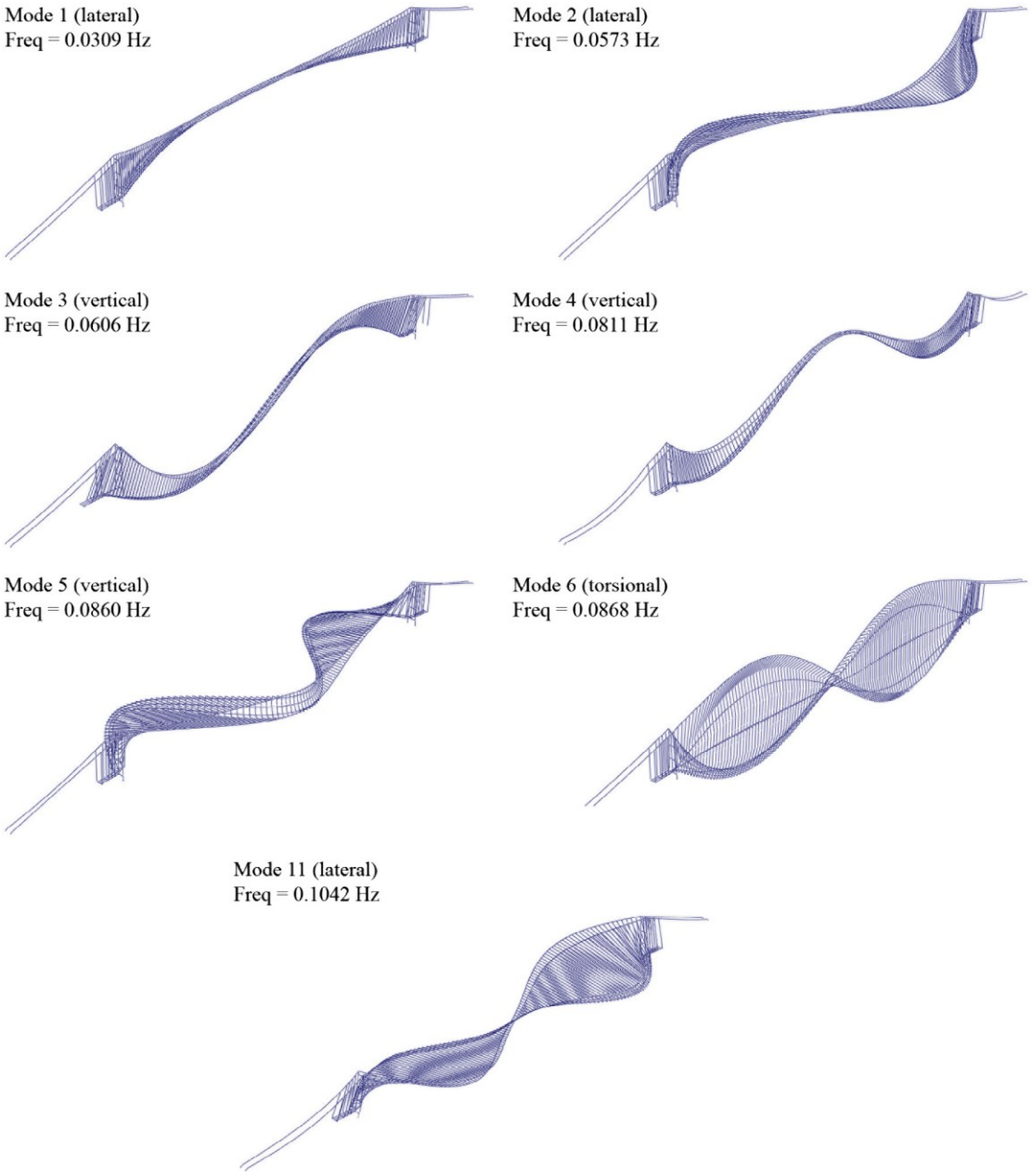

Figure 3.10 Natural frequencies and mode shapes considered for flutter analysis

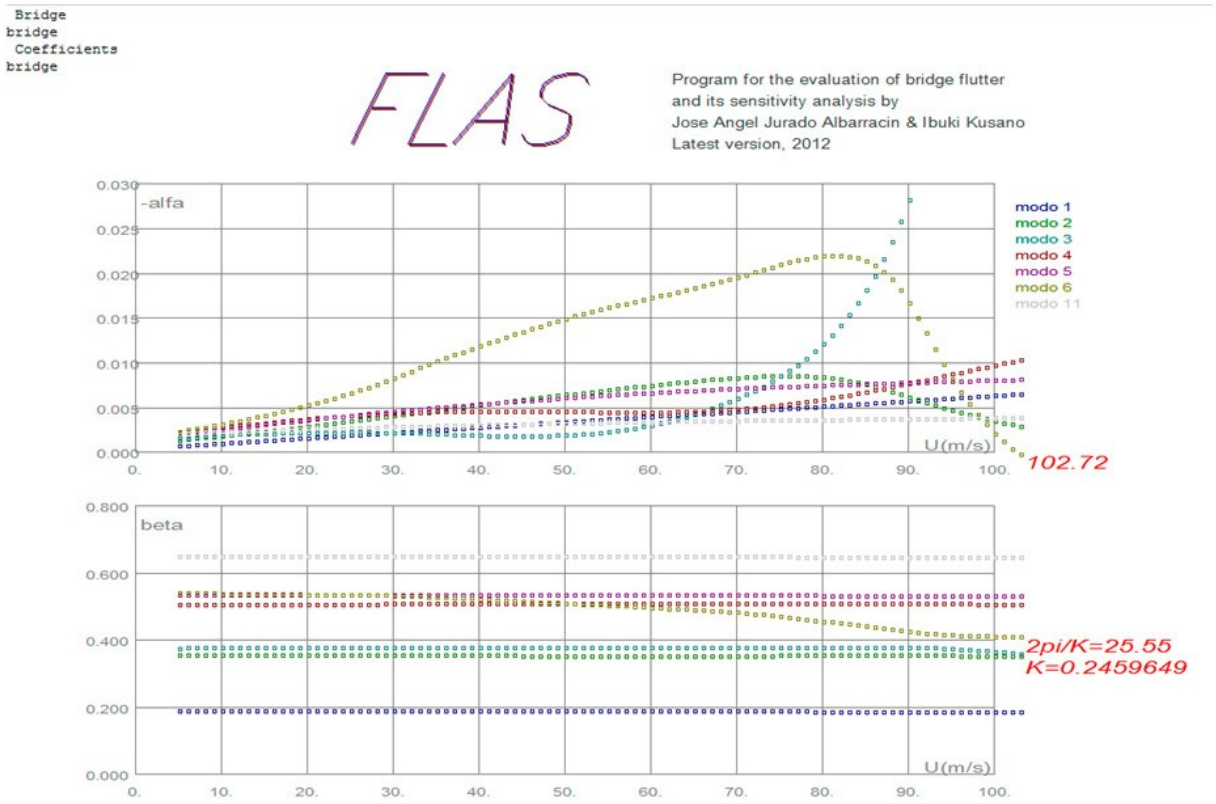

Figure 3.11 Flutter analysis result

Moreover, they developed a numerical methodology for optimization of the deck shape and cable size in long span bridges considering aeroelastic and structural constrains, further details can be found in [21], [22] and [23].

3.3. D'Asdia and Sepe studies

This study was conducted on the 1992 design of the proposed bridge over the Messina Strait, and it was further examined in [24], with a multi-mode approach, originally proposed by Scanlan in [25].

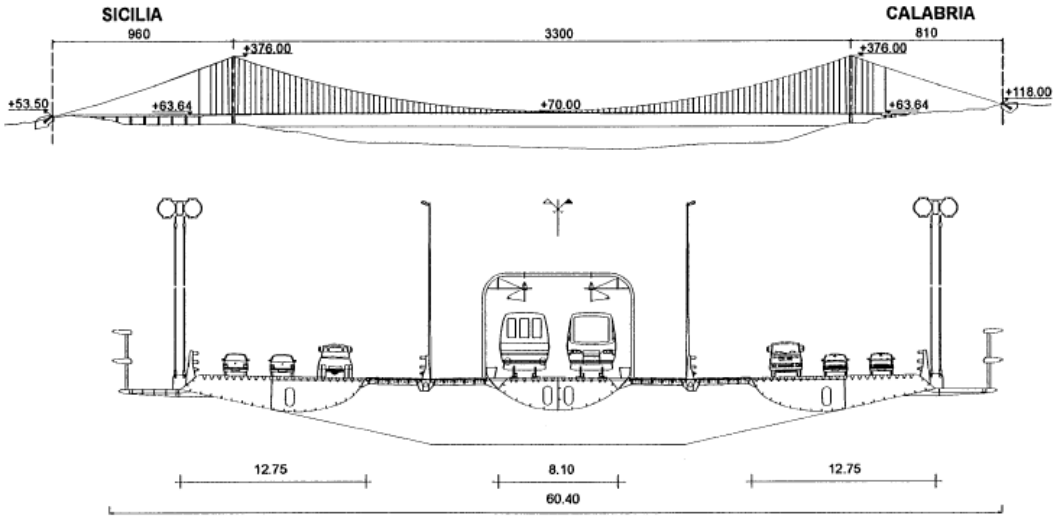

Figure 3.12 1992 design of the proposed bridge

A FEM model has been developed consisting of 5000 d.o.f., and the first 20 natural modes around the dead load equilibrium configuration or around the average configuration in wind flow have been evaluated and a computer code was able to take into account geometrical nonlinearities and the stiffness. Average values of mass M per unit length and torsional mass moment of inertia I per unit length have been evaluated taking into account both main cables and deck:

M [kg/m]	5.50E+04
I [kgm^2/m]	2.80E+07

Table 3.5 Mechanical properties assumed

The structural damping ξ_i has been assumed varying from 0.6% to 0.9%, depending on the modes considered.
The multi-mode approach is able to provide within the same analysis more solutions (Table 3.7), according to the number of modes taken into account, using the aeroelastic derivatives reported in Figure 3.13, obtained through experimental investigations carried out during the design process.

It can be observed in Figure 3.14 that several pairs of vertical and torsional modes have nearly identical mode shapes. For these modes, the ratio between frequencies of torsional mode and the corresponding vertical mode is close to the ratio between the deck half-width and the polar moment of inertia radius, meaning that the deck stiffness is negligible compared to the cable stiffness.

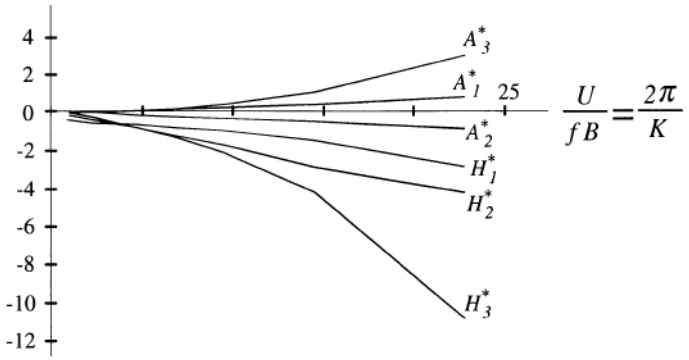

Figure 3.13 Flutter derivatives

mode	angular frequency ω_j (rad/s)	period T_j (s)	most significant component
a	0.195	32.2	1st lateral
b	0.352	17.8	2nd lateral
c	0.380	16.5	1st vertical
d	0.500	12.6	1st torsional
e	0.501	12.5	3rd lateral
f	0.508	12.4	2nd vertical
g	0.606	10.4	2nd torsional
h	0.626	10.0	4th lateral
i	0.677	9.3	3rd vertical
l	0.705	8.9	5th lateral
m	0.803	7.8	3rd torsional

Table 3.6 Natural angular frequency and period

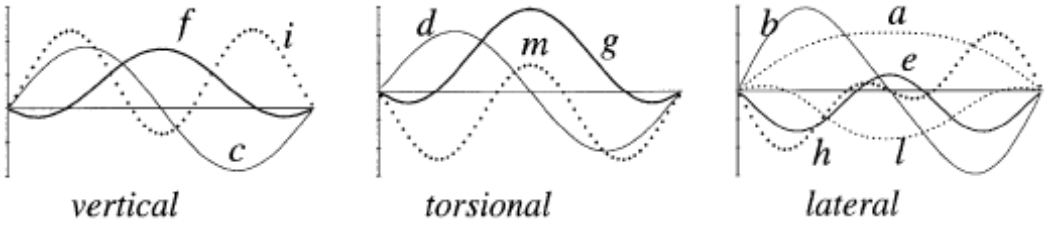

Figure 3.14 Natural modes

The critical wind speed corresponds to the lowest value (94 m/s), is in good agreement with the analytical and experimental results obtained during design studies.
It can be observed that the second vertical mode *f* has roughly the same frequency of the first torsional one *d*: this introduced complications in their numerical evaluation but, most importantly, it indicates that these modes can't be excited independently one from the other, as confirmed by wind tunnel experiments performed on a 1:250 model during the design process.

modes taken into account	ω_c rad/s	K_c	U_c m/s
c d	0.418	0.276	94
f g	0.544	0.204	165
i m	0.726	0.200	225
c d f g	0.418	0.276	94
c d f g i m	0.418	0.276	94
c d (deformed)	0.424	0.275	96

Table 3.7 Results of the multi-mode analysis

It is also important to assess the role of horizontal displacements along-wind (lateral modes), whose contribution can be stabilising or not depending on the deck geometry and on the mode shapes; in this case, the mode *b* along-wind has exactly the same shape (Figure 3.14) of the first vertical one *c* and also the frequencies are very close, thus it is expected to be aerodynamic coupled; on the other hand, the frequencies of mode *h* and of the third vertical mode *i* are close, but instead they are orthogonal.

PART 2

Chapter 4

Messina Strait Bridge project

4.1. General bridge outline

The Messina Strait Bridge is planned at the minimum width of the Strait, at approximately 3 kilometres between the cities of Ganzirri in Sicily and Cannitello in Calabria.

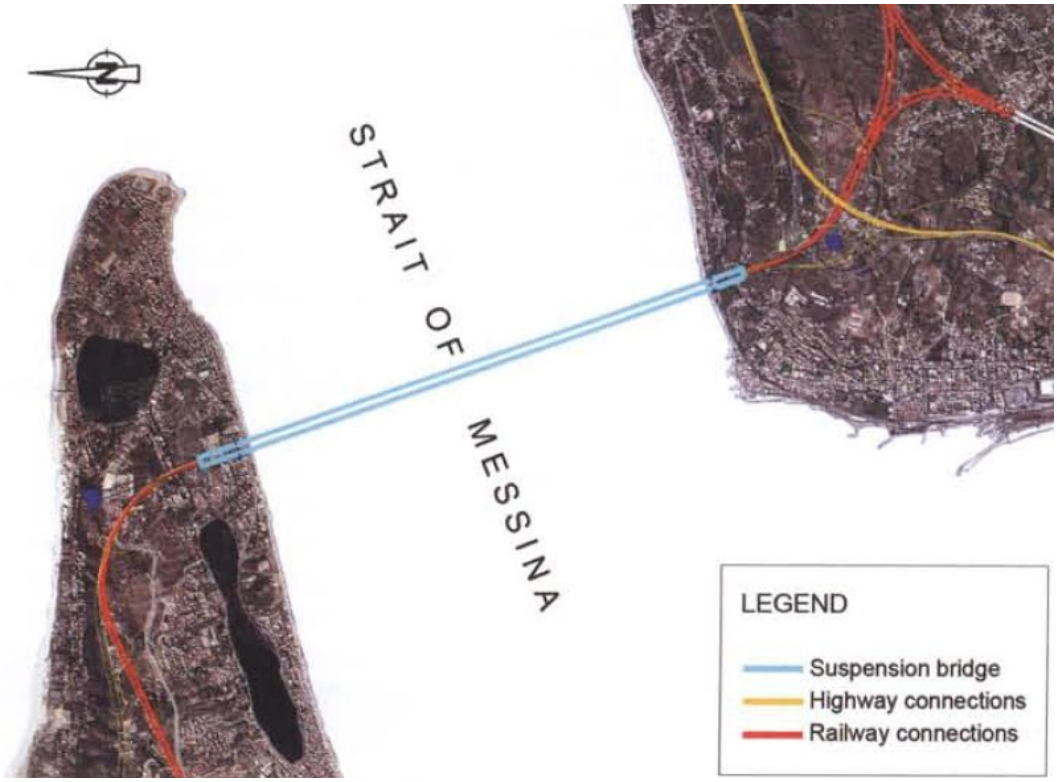

Figure 4.1 Plan view of the location and the connections

The final overall configuration is shown in Figure 4.2:

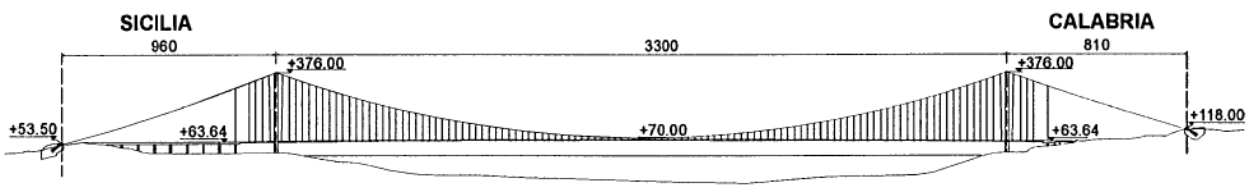

Figure 4.2 Side view of the Messina Bridge

4.2. Suspended deck

The suspended deck consists of three stream-lined longitudinal boxes, the lateral ones designated for the road carriageways, while the centre one for the railways.
The road platform comprises two 3.75 m wide road lanes plus emergency lanes, for each direction. Inspection and maintenance lanes are located externally on cantilevering elements at the side of the road boxes, outside from the hangers. The central box carries two railway tracks plus inspection walkways. The large open area between the boxes brings the total deck width to about 61 m, with 52 m distance between the cables.

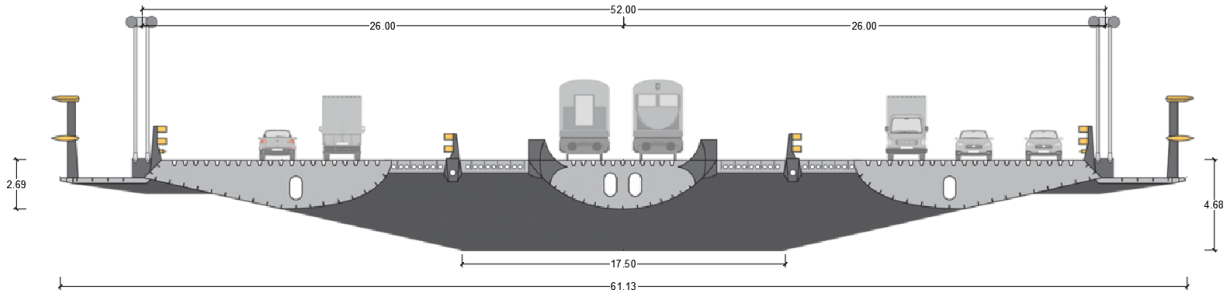

Figure 4.3 Cross section of the deck

To achieve aerodynamic efficiency, the central box had to be as shallow as possible, in order to maximize the effectiveness of the total centre void area, hence, the depth of the railway box was set to 2.2 m, which was considered the minimum for internal inspection and maintenance.
On the other hand, the road boxes were made deeper, with the purpose of increasing the overall deck torsional stiffness and achieving the minimum bottom flange plate thickness to minimize weight while maintaining durability and local stability, defined at 9 mm, resulting in a 2.7 metres depth for the road boxes. The upper orthotropic deck plate configuration was on the contrary dominated by local strength and fatigue behaviour resulting in a minimum deck plate thickness of 14 mm and 6 mm for the trapezoidal trough.
The curved shape is the result of an optimization process, to achieve the best aerodynamic efficiency, and it also plays a role in improving local stability against buckling of plates in longitudinal compression.
Moreover, the deck structure is equipped with four inspection gantries, two in the centre span and one in each of the side spans.

The longitudinal boxes are carried by transverse box girders spanning between the hanger planes, forming a grid for the whole suspended deck structure.
The transverse girders are 4 m wide rectangular boxes spanning 52 m between the hangers, varying in depth from about 1.3 to 4.7 metre, and formed by plates whose thickness varies from 12 to 24 mm, and the optimum distance between the transverse girders is considered to be 30 m.

Figure 4.3 Virtual view from the deck

Figure 4.4 Virtual view from below the bridge

The static redundancy of the system ensures that the deck would not collapse even on the unlikely event that all the hangers at one end of a crossbeam breaks.

Different steel grades will be employed: S355ML for most of the deck, with S420ML for special elements at the tower articulation, and the total amount of structural steel expected in the deck is about 55.000 tons, the resulting total steel girder self-weight is only 18.1 t/m, with a total deck dead load of about 23 t/m.

To improve serviceability under severe wind conditions, external wind screens are implemented in the overall aerodynamic design. Small aerofoils control the flow and act as aerodynamic dampers, while the wind protection element is a perforated metal sheet tuned so as to reduce the air flow and protect vehicles from the direct action of strong wind.
The interior boxes will be dehumidified to control corrosion, and external steel surfaces will be painted with a multi-layer system to maximize durability.
Impregilo JV group, winner of the 2005 tender, proposed a simpler trapezoidal shape instead of the curved lower plating for the railway box, and it would have continuous longitudinal web under each rail, in order to minimize the potential fatigue damage.

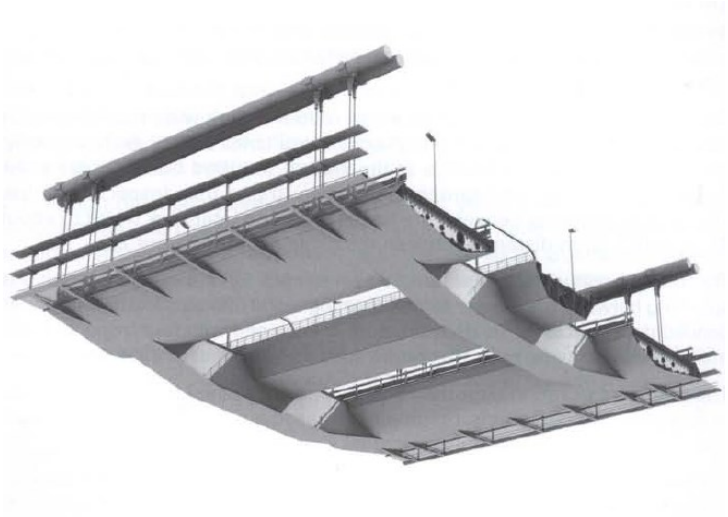

Figure 4.5 3D model of the 2005 proposed deck

4.3. Deck restrains and expansion joints

Typically, suspension bridges have lateral spans close to half the main span length, but the land configuration of the Messina Strait bridge site does not allow normal configuration with two long side spans: on Sicily's side the site is so close to the east island point that there is simply not enough space, and the access viaducts must immediately turn southwards. On Calabria's side, the coast is comparatively steep, and the hills quickly become too high for a side span. Indeed, the road and rail corridors go into tunnel within a short distance.
Due to these short spans, the design of the deck restrains, and expansion joints was complicated, but an innovative idea arose in the early nineties, thanks to the contribution of Dr. Brown, who proposed to make the longitudinal boxes discontinuous at each tower, replacing the continuous structure with two simply supported spans and restoring the continuity in the short spans. The central railway box is left continuous throughout.

Figure 4.6 Lateral span on Sicilian side

The deck structure is retained laterally at the towers via a large pendulum strut with X-bracing. This configuration creates an extremely flexible deck segment at the towers, and as a consequence the lateral forces in the side span are dramatically reduced and the rotations, due to transverse wind are carried at the tower segment, and not to the abutments.
On the other hand, the rotation about the vertical axis of the flexible deck segment at the tower are absorbed via moderate flexure in the continuous central rail box. This doesn't generate forces in the simply supported outer roadway box segments which have small expansion joints, which do not experience the overall large span displacements but only the local relative movements associated with temperature changes over short segment length and local kinematics from the global bridge behaviour.
The span of the special road and rail box segments at towers to achieve the optimal balance between flexibility and size was found to be 50 m.

In 2005, the Impregilo JV group improved the complex expansion joint mechanism, with consequent reductions in cost, wear and maintenance requirements, by reducing substantially the longitudinal displacement. They proposed the longitudinal connection between the deck and towers through two pairs of hydraulic devices or "buffers", connected to short cantilever extensions of the side span of a transverse cross girder. These devices, operating via hydraulic control, behave in an elastic manner up to a force limit, and then at higher longitudinal displacements maintain a constant force in a pseudo "elastic-perfectly-plastic" manner, as result many frequent displacements are restrained. Furthermore, the devices behave as a passive control system for longitudinal seismic actions, introducing a beneficial energy dissipation for the earthquake response.

Figure 4.7 Proposed deck-tower connection

4.4. Suspension system

The suspension system comprises two pairs of main cables set 52 m apart. In the main span, each 1.24 m diameter cable comprises 44.352 wires of 5.38 mm, giving a total steel cross section area just over 1 m^2. The total length of each cable will be 5.270 m, whereas the total amount of structural steel used in the suspension system is about 167.000 t for cable wires, 5.500 t for suspenders and 7.000 t for cable clamps and saddles. In addition, this was assessed as the best cable configuration in [26]. The hangers are spaced every 30 m, connecting the ends of the crossbeams from the main cables. Hanger diameters vary up to a maximum of about 160 mm, and the longest hanger next to the towers are about 300 m long and weigh about 30 tons.

4.5. Towers

The towers are huge structures, rising to a height of 382 metres and sustaining the enormous vertical load applied from the main cables. Key design considerations include the challenging economic constructability and the need to sustain high lateral forces deriving from horizontal wind load on the whole structure as well as very large seismic forces arising from the design earthquake conditions.

The steel plate material utilized is grade 420, with thickness varying from 40.45 mm over most of the height to 60-65 mm in the lower sections and the total amount of structural steel is expected to about 55.500 t per tower.

The tower legs are multicellular structures with overall dimensions of 12x16 m and connected by four crossbeams having rectangular cross section of 4x16.9 m.

The shape of tower legs in the preliminary design was optimized for structural performance, aerodynamic behaviour, and aesthetic appearance, resulting in the peculiar "lozenge" cross section. Such shape exhibits better wind drag coefficients than a simple rectangular one, while at the same time eliminating high stress area in connection with the strong wind multi axial bending present.

The base connection of the steel legs to the concrete foundation plinth is obtained by embedding into the concrete a 12 m section of leg equipped with a large number of shear connectors.

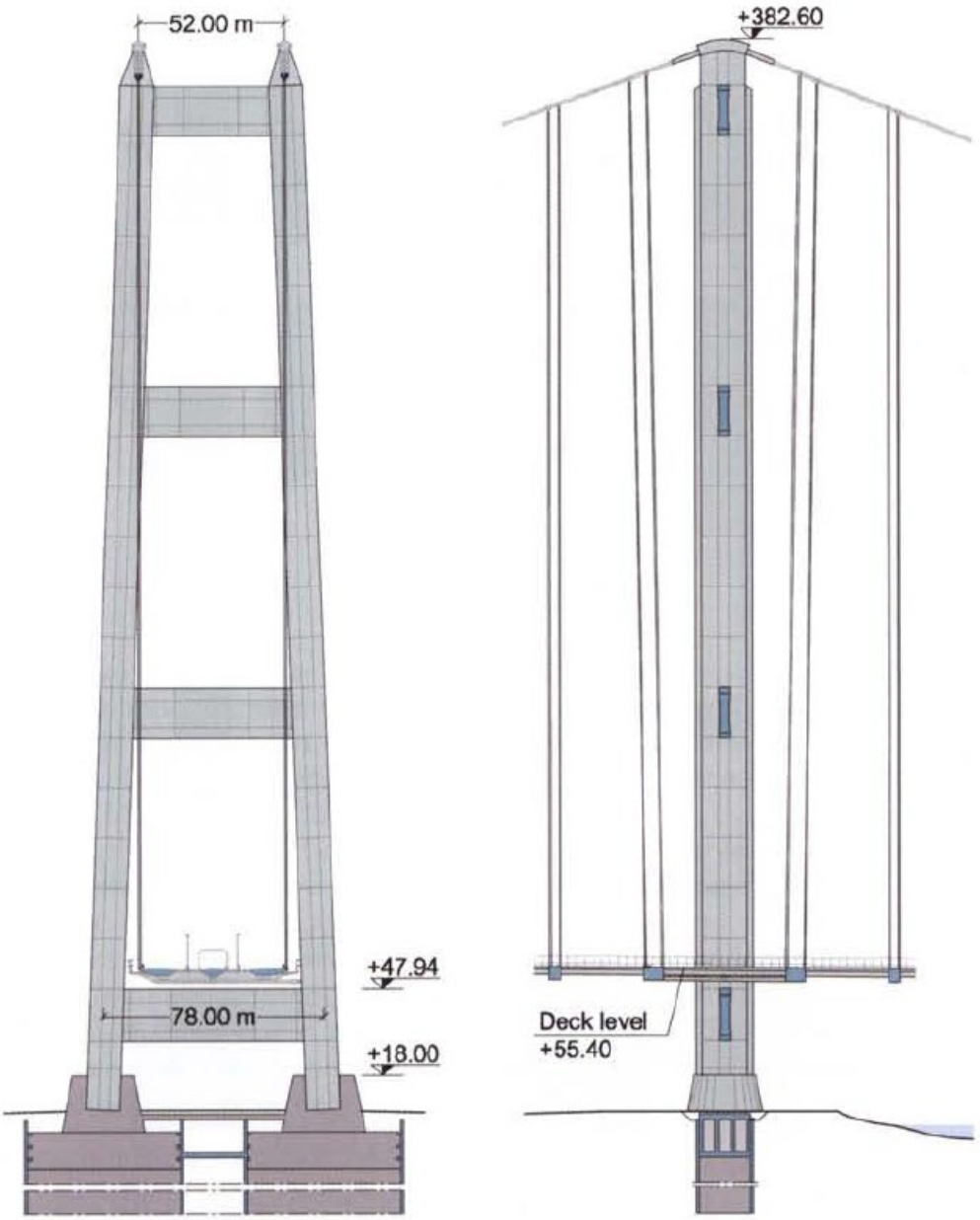

Figure 4.8 Preliminary design of the towers

Impregilo JV proposed some variations regarding towers, and the most evident one being mainly for aesthetic reasons: the removal of the lower crossbeam and the shaping of the remaining three with curved top and bottom flanges (Figure 4.9).

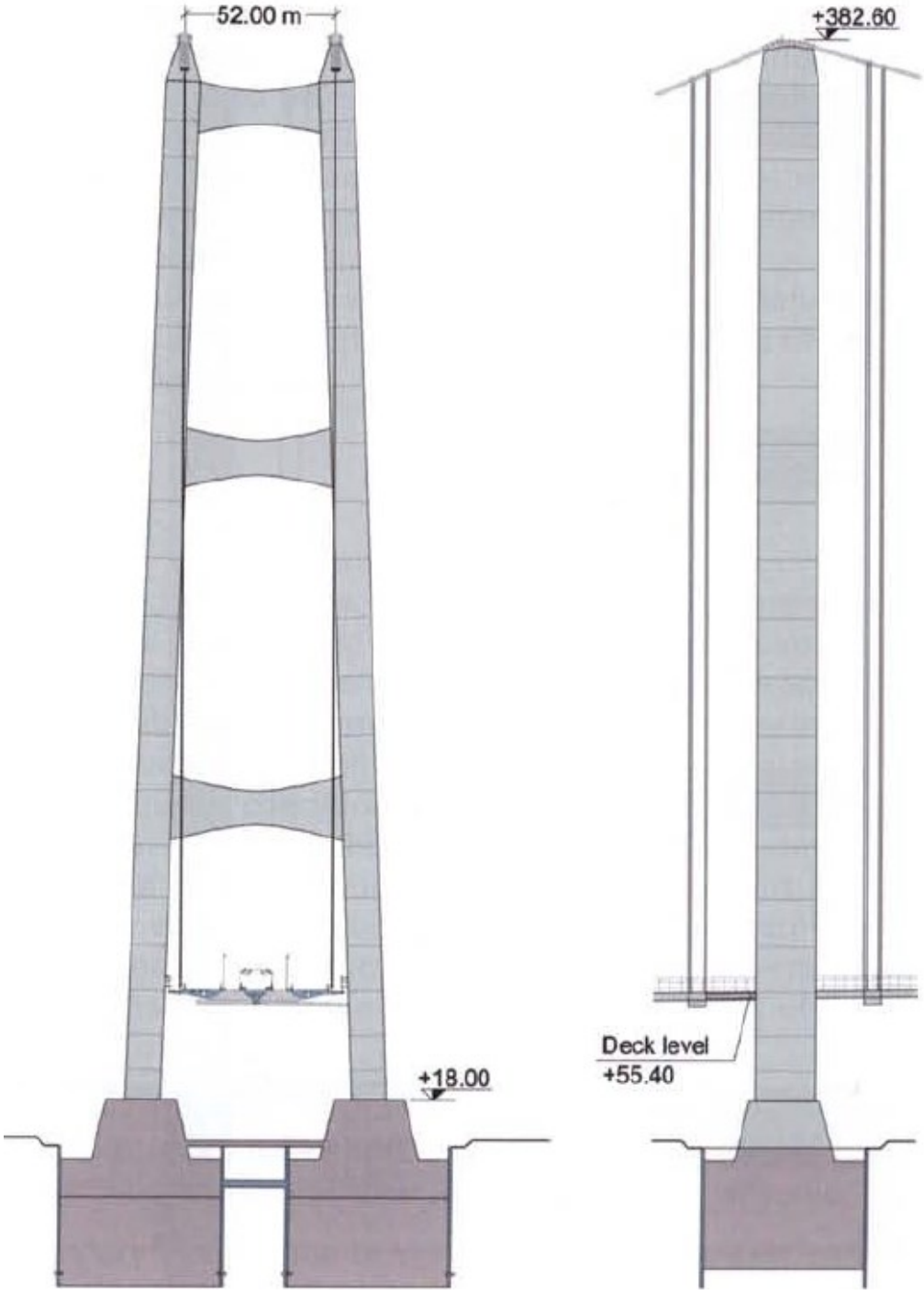

Figure 4.9 Towers according to the 2005 proposal

4.6. Foundations

The bridge main span interacts with the soil through the towers and at the anchor blocks.
The steel towers are connected to massive concrete foundations 130x60 metres in plan, placed at a depth of 10 metres below sea level, within an excavation supported by T-shaped diaphragms walls and waterproofed by jet grouting treatments, which is aimed at preventing potential settlement and liquefaction due to excess pore pressure triggered by earthquake events.

4.7. Operation & maintenance strategies

A fundamental requirement of the bridge is a specific strategy to optimize management, operation and maintenance, due to the large scale and the technical complexity of the structure, but as well as the economic relevance, being an essential link in the national transportation system.
Such a strategy is aimed at achieving best performance in terms of:

- Safety, durability and value of the structure;
- Effective and economic maintenance;
- Safety of users and maintenance personnel;
- Service continuity and quality;
- Security against possible offences.

In addition, a very advanced and innovative monitoring, control and management system was developed for the Messina Bridge, and it consists of a fully integrated instrumentation and communication system involving the collection, distribution, processing and storage of all needed information, including procedures and equipment to manage various events and scenarios.

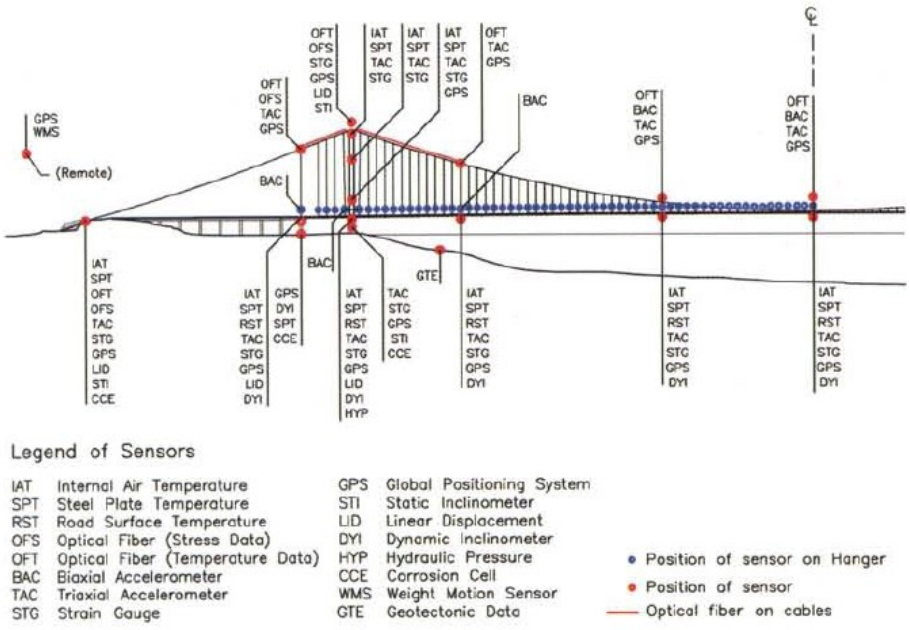

Figure 4.10 Structural instrumentation layout

Chapter 5
MATLAB flutter analysis

5.1. Introduction to multimodal aeroelastic analysis

Suspension bridges subjected to self-excited aerodynamic loads represents a dynamic non-proportionally damped system where both damping, and stiffness are affected by wind load and oscillation frequency.

The MATLAB based flutter analysis, consists in a multimodal aeroelastic analysis, including aerostatic nonlinearities, on a one-dimension continuum model of the suspension bridge.

Vertical and torsional oscillations in suspension bridge subjected to aeroelastic loads are governed by the Equations 5.1 and 5.2 [27], which are based on the classical linearized theory, but improved by including wind-related geometric nonlinearities, such as the stiffening/softening induced by the lift force and a Prandtl-like second-order effect due to the drag force. This procedure has been introduced in [28] and [29].

$$L_{se} = \mu_g \frac{\partial^2 v(z,t)}{\partial t^2} + c_v \frac{\partial v(z,t)}{\partial t} + EI_x \frac{\partial^4 v(z,t)}{\partial z^4} - H \frac{\partial^2 v(z,t)}{\partial z^2} + \frac{\partial^2 \left(m_y(z) \vartheta(z,t) \right)}{\partial z^2} + \left(\frac{8f}{l} \right)^2 \frac{E_c A_c}{L_c} \int_0^l v(z,t)\, dz \tag{5.1}$$

$$M_{se} = I_\vartheta \frac{\partial^2 \vartheta(z,t)}{\partial t^2} + c_\vartheta \frac{\partial \vartheta(z,t)}{\partial t} + EI_\omega \frac{\partial^4 \vartheta(z,t)}{\partial z^4} - (GI_t + Hb^2) \frac{\partial^2 \vartheta(z,t)}{\partial z^2} + m_y(z) \frac{\partial^2 v(z,t)}{\partial z^2} + b^2 \left(\frac{8f}{l} \right)^2 \frac{E_c A_c}{L_c} \int_0^l \vartheta(z,t)\, dz \tag{5.2}$$

Where:

- L_{se} and M_{se} are the aeroelastic (self-excited) lift and moment;
- v and ϑ are the vertical and torsional displacement of the deck-cross section;
- μ_g and I_ϑ are the bridge mass and mass moment of inertia per unit length;
- $c_v = 2\mu_g \xi_v \omega_v$ and $c_\vartheta = 2I_\vartheta \xi_\vartheta \omega_\vartheta$ are the damping coefficients, being ξ_v, ξ_ϑ and $\omega_v, \omega_\vartheta$ damping ratios and angular frequencies;
- EI_x, EI_ω and GI_t are the vertical bending rigidity, warping and primary torsional rigidity, respectively;
- H is the horizontal component of the main cable tension;

- l is the main span length;
- b is half the distance between cables;
- f, L_c, A_c and E_c are the cable sag, length, cross-section area and Young modulus;
- $m_y(z)$ is the horizontal bending moment due to the steady drag force.

Considering a solution for Equations 5.1 and 5.2 in the harmonic form:

$$v(z,t) = \bar{v}(z)e^{\lambda t} \tag{5.3}$$

$$\vartheta(z,t) = \bar{\vartheta}(z)e^{\lambda t} \tag{5.4}$$

The spatial functions are expressed by weighted sums of sinusoids having different wavelengths:

$$\bar{v}(z) = b\sum_{j=1}^{n} a_{vj}\, sin\left(\frac{j\pi z}{l}\right) \tag{5.5}$$

$$\bar{\vartheta}(z) = \sum_{k=1}^{m} a_{\vartheta k}\, sin\left(\frac{k\pi z}{l}\right) \tag{5.6}$$

A quadratic eigenvalue problem, of $N = n + m$ equations, is obtained for the unknowns a_{vj} and $a_{\vartheta k}$, by applying Galerkin method:

$$[A(\lambda, U)]\{a_{v,\vartheta}\} = \{0\} \tag{5.7}$$

Equation 5.7 solutions are the eigenvalues λ_r and eigenvectors $\{a_{v,\vartheta}\}_r$ describing different vibration shape modes, with $r \in [1; 2N]$, and they can be expressed as a linear combination of the 2N independent eigen solutions as:

$$V(x,t) = \sum_{r=1}^{2N} v_r(z)e^{\lambda_r t} \tag{5.8}$$

$$T(x,t) = \sum_{r=1}^{2N} \vartheta_r(z)e^{\lambda_r t} \tag{5.9}$$

Where $v_r(z)$ and $\vartheta_r(z)$ are the vertical and torsional components of the r^{th}eigensolution.
The vertical and torsional displacements are expresses as a sum of r modal contributions; each one being defined by the sum of $N = n + m$ harmonic functions. The real part of the eigenvalues governs the exponential trend of the modal contributions, while the imaginary part represents the modal frequency. If the real part of an eigenvalue becomes positive, the system is unstable, and with the increase of time it will diverge exponentially.
Considering a step value of wind velocity, a complex eigenvalue analysis is performed for each step to analyse the variation of natural frequencies and the corresponding modal shape. When the real part becomes null, the eigenvalue violets the stability condition, and the corresponding wind velocity is the critical velocity.

5.2. Messina Strait bridge project case

The aeroelastic analysis was performed on this project, in order to examine the structural frequencies and modal shapes with increasing wind speed.
The main features of the case study are summarized in Table 5.1, Table 5.2 and Figure 5.1:

l [m]	f [m]	b [m]	Lc [m]	Ac [m^2]	μ_g [kg/m]	I_ϑ [kgm^2/m]	I_x [m^4]	I_ω [m^4]	It [m^4]
3300	297	26	3.37E+03	4.83	7.52E+04	2.87E+02	9.394	0	3.0918

Table 5.1 Main features of the study-case

$c_{l,0}$	0
$c_{d,0}$	0.1

Table 5.2 Steady-state aerodynamic coefficients

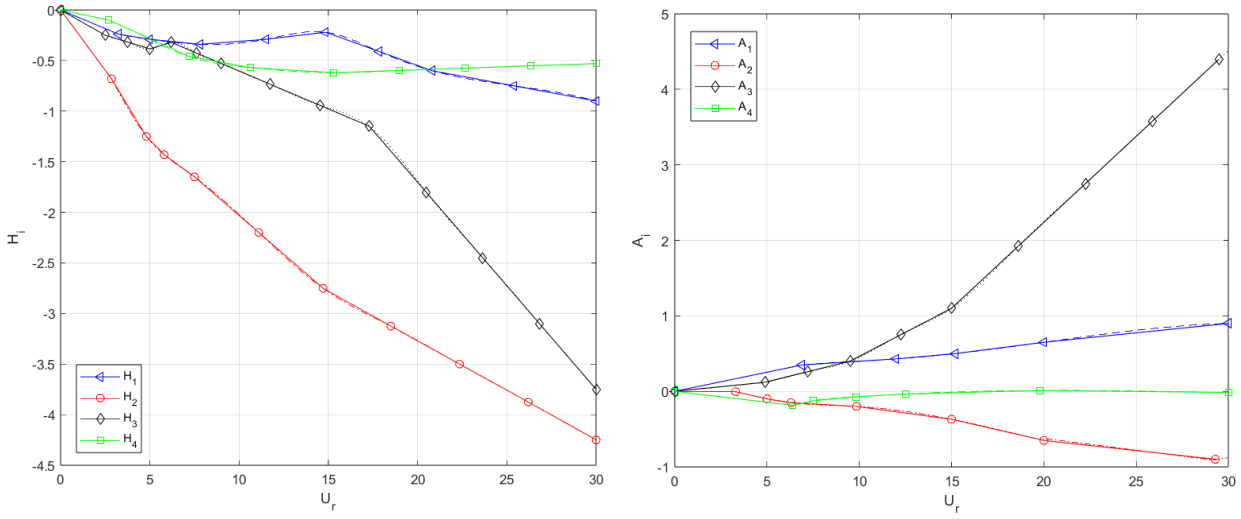

Figure 5.1 Flutter derivatives of the Messina bridge project

Equations 5.12 and 5.13 describes vertical and torsional displacements components and eight sinusoidal functions were chosen to describe them: $n = m = 8$, thus a total of sixteen modes were extracted, however in this study only the first eight modes are reported.
The variation of modal frequencies and damping factors for increasing wind speed is shown in Figures 5.2 and 5.3:

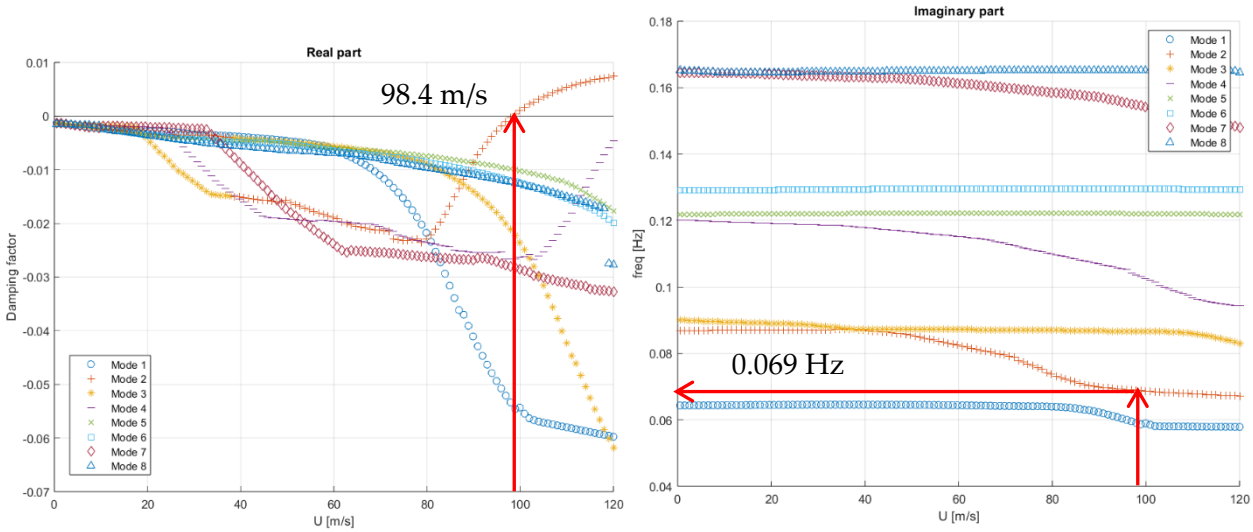

Figure 5.2 Damping factors and modal frequencies

The real part of the eigenvalue corresponding to the second mode becomes positive at the critical wind speed of 98.4 m/s and at a flutter frequency of 0.069 Hz. In fact, the flutter modal shape (Figure 5.3, Mode 3) in wind-free condition is purely torsional however, the correspondent frequency coalesce with the frequency of mode 2 (Figure 5.2), causing the vertical and torsional modes to couple, leading to flutter (Figure 5.4, Mode 2). And it important to point out that the flexural and torsional components of the critical mode, at flutter condition, are out of phase.

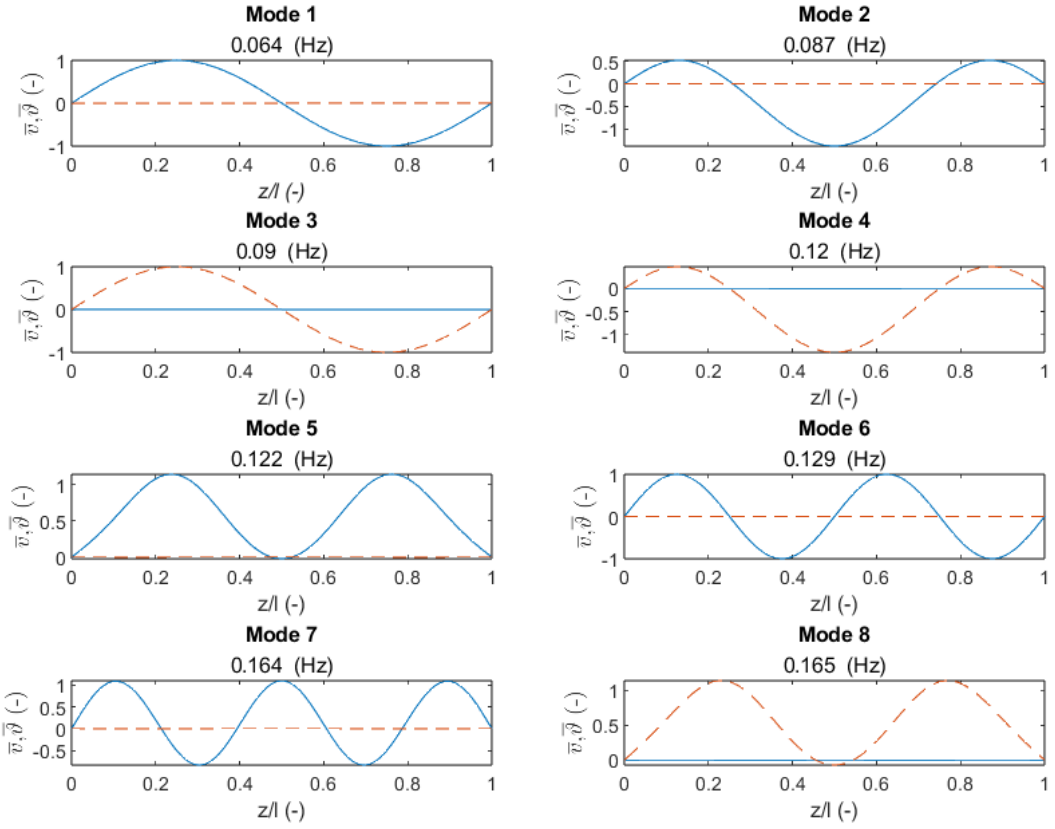

Figure 5.3 Messina bridge modal shapes in wind-free condition

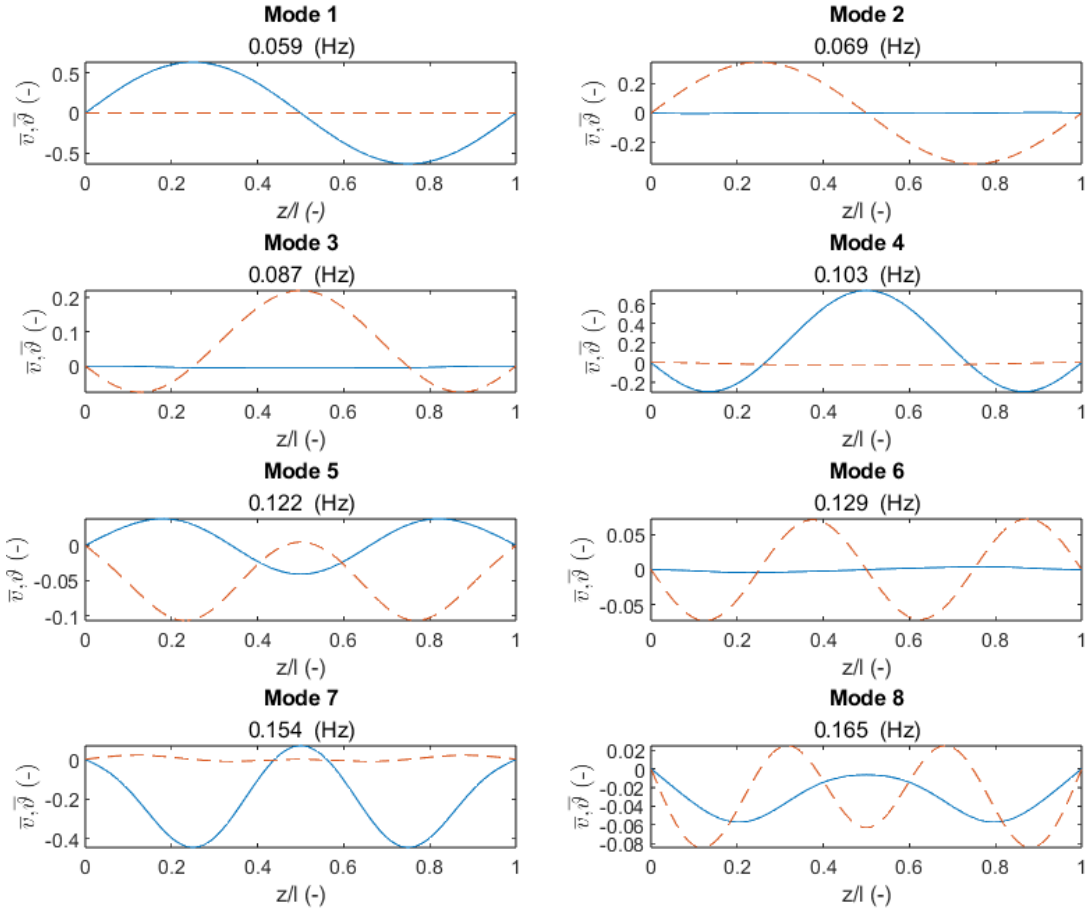

Figure 5.4 Messina bridge modal shapes critical flutter condition

5.3. Result comparison

In conclusion, the results obtained are compared with the flutter wind velocity and flutter frequency derived by Jurado *et al*. [19]and by D'Asdia and Sepe [20]:

	MATLAB	Jurado et al.	D'Asdia&Sepe	%ΔJurado et al.	%ΔD'Asdia&Sepe
Uf [m/s]	98.4	102.7	94	4.2	-4.7
f [Hz]	0.069	0.066	0.067	-4.2	-2.7

Table 5.3 Messina bridge flutter analysis, result comparison

The results obtained with a multimodal aeroelastic analysis, including aerostatic non linearities are perfectly aligned to the results obtained in the studies considered, in fact the critical wind speed calculated with MATLAB can be considered the mean value between the other two, with a relative error lower than 5%. Similarly, the flutter frequency, obtained with MATLAB, is slightly greater than the literature values, but still lower than 5%.

Chapter 6
ANSYS flutter analysis

In this thesis, the flutter analyses are performed by finite element numerical models using the commercial software ANSYS APDL, which allows to easily take into account several non-linear key features of suspension bridges: this kind of structures presents a non-linear geometric behaviour due to hangers and main cables: the increase of tension in main cables induce a reduction of displacements given by further loads. This non-linear behaviour has been considered by including the pre-stress effects due to pretension in the modal analyses, which the software easily allows to implement. Accordingly, the weight of the bridge itself generate a global stiffening effect on the structure, so neglecting the influence of these phenomena would lead to wrong physical representations.

6.1. Flutter problem using ANSYS

The Chinese researchers X.G. Hua and Z.Q. Chen [30], in 2008, proposed a full order approach that allows to analyse coupled flutter on long-span bridges, employing the measured flutter derivatives from tests performed in wind tunnels on bridge sectional model, using the commercial finite element software ANSYS. The method is based on the definition of the aeroelastic loads by means of a particular user defined element and is shortly illustrated below. An example of this analysis can be found in [31] and [32].
The equation of motion of a deck section in a smooth flow can be expressed as:

$$M\ddot{X} + C\dot{X} + KX = F_{ae} \tag{6.1}$$

Where

- M is the global mass matrix;
- C is the damping matrix;
- K is the stiffness matrix;
- $\ddot{X}$ is the acceleration vector,
- $\dot{X}$ is the velocity vector,
- X is the displacement vector,
- F_{ae} is self-excited nodal forces vector, defined in Equation 2.21.

By converting the distributed aeroelastic forces applied on a generic element of a bridge girder into equivalent nodal loads acting on the element's ends, the equivalent nodal loading for that element is obtained:

$$F_{ae}^{e} = K_{ae}^{e} X^{e} + C_{ae}^{e} \dot{X}^{e} \tag{6.2}$$

Where K_{ae}^{e} and C_{ae}^{e} are the aeroelastic stiffness and damping matrices of element *e*, respectively. Using a lumped formulation, they can be expressed as:

$$K_{ae}^{e} = \begin{bmatrix} K_{ae1}^{e} & 0 \\ 0 & K_{ae1}^{e} \end{bmatrix} \tag{6.3}$$

$$C_{ae}^{e} = \begin{bmatrix} C_{ae1}^{e} & 0 \\ 0 & C_{ae1}^{e} \end{bmatrix} \tag{6.4}$$

$$K_{ae1}^{e} = a \begin{bmatrix} 0 & 0 & 0 & 0 & 0 & 0 \\ 0 & P_4^* & P_6^* & BP_3^* & 0 & 0 \\ 0 & H_6^* & H_4^* & BH_3^* & 0 & 0 \\ 0 & BA_6^* & BA_4^* & B^2A_4^* & 0 & 0 \\ 0 & 0 & 0 & 0 & 0 & 0 \\ 0 & 0 & 0 & 0 & 0 & 0 \end{bmatrix} \tag{6.5}$$

$$C_{ae1}^{e} = b \begin{bmatrix} 0 & 0 & 0 & 0 & 0 & 0 \\ 0 & P_1^* & P_5^* & BP_2^* & 0 & 0 \\ 0 & H_5^* & H_1^* & BH_2^* & 0 & 0 \\ 0 & BA_5^* & BA_1^* & B^2A_2^* & 0 & 0 \\ 0 & 0 & 0 & 0 & 0 & 0 \\ 0 & 0 & 0 & 0 & 0 & 0 \end{bmatrix} \tag{6.6}$$

Where $a = \rho U^2 K^2 L_e/2$ and $b = \rho UBKL_e$, B is deck's width and L_e is the length of the element *e*.
Hence it is necessary to represent the elemental stiffness and damping matrices due to motion-dependent aeroelastic forces by applying user-defined element *MATRIX27* in Ansys. The element can only model either an aeroelastic stiffness matrix or an aeroelastic damping matrix, but not both simultaneously, therefore a pair of MATRIX27 elements are attached to each node of a generic bridge deck element, to simulate the aerostatic forces, as illustrated in Figure 6.1:

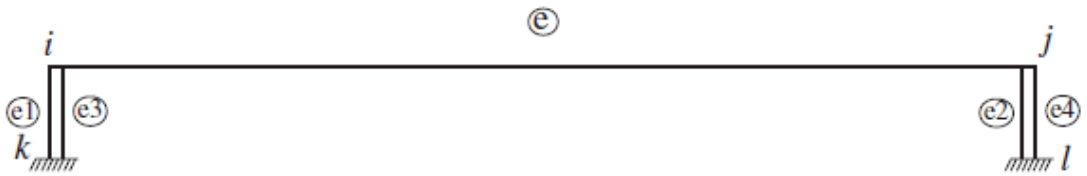

Figure 6.1 Hybrid finite element model

The MATRIX27 elements *e1* and *e3* represent respectively the aeroelastic stiffness and damping of the node *i*, as the MATRIX27 elements *e2* and *e4* represent respectively the aeroelastic stiffness and

damping of the node j. If the length of each bridge deck element is the same, the element matrices are simplified as:

$$K^{e1} = 2K_{ae}^{e} \tag{6.7}$$

$$C^{e3} = 2C_{ae}^{e} \tag{6.8}$$

$$K^{e2} = 2K_{ae}^{e} \tag{6.9}$$

$$C^{e4} = 2C_{ae}^{e} \tag{6.10}$$

Assembling all elemental matrices into a global aeroelastic stiffness and damping matrices leads to:

$$F_{ae} = K_{ae}X + C_{ae}\dot{X} \tag{6.11}$$

The mathematical model of an integrated system is obtained by substituting Equation 6.11 into 6.1, with the effect of aeroelasticity parametrized by wind velocity and vibration frequency:

$$M\ddot{X} + (C - C_{ae})\dot{X} + (K - K_{ae})X = 0 \tag{6.12}$$

By performing a modal decomposition in the state-space, the equation 6.12 is transformed into an eigenvalue problem:

$$(A - \mu I)\phi_{\mu} = 0 \tag{6.13}$$

With this equation, a complex eigenvalue analysis can be carried out to determine the eigenvalues of the system at a specific wind velocity and vibration frequency.
Assuming the conjugate pairs of complex eigenvalues $\mu_i = \alpha_i \pm i\beta_i$ and the conjugate pairs of complex eigenvectors $\phi_i = p_i \pm iq_i$. The real part α_i is related to modal damping, therefore, if it becomes null the system will be dynamically unstable, and the corresponding wind velocity U_f is the critical flutter wind velocity, the maximum speed the bridge can withstand. The imaginary part β_i of the complex eigenvalue μ_f will be the flutter frequency.

It is necessary to provide the variation of both wind velocity and vibration frequency in the complex eigenvalue analysis, so a mode-by-mode tracking method is employed to iteratively search the flutter frequency and the flutter velocity.
The procedure is summarized below:

1. Establish the Finite Element model for the original structure without MATRIX27 elements, perform a modal analysis, including the effects of permanent loads, and compute the first m natural frequencies ω_i^0 $(i = 1,2,\dots,m)$;
2. Set an initial wind velocity U_0 and its increment ΔU;
3. Let the initial oscillation frequency ω_0 be the frequency ω_i^0 of each natural mode;

4. Determine the reduced frequency K and the aeroelastic stiffness and damping matrices in MATRIX27 elements, with the support of a MATLAB script, as in Equations 6.5 and 6.6 at the current iteration, and then carry out the complex eigenvalue analysis;
5. Compare the imaginary part of the i^{th} computed complex eigenvalue μ_i with ω_0. If

$$|(Im(\mu_i) - \omega_0)/Im(\mu_i))| > 10^{-3} \quad let\ \omega_0 = Im(\mu_i) \tag{6.14}$$

repeat step 4 and 5, otherwise go to step 6;
6. Loop steps 3-5 over all the m computed natural modes to obtain all m pairs of complex eigenvalues at the current wind velocity U;
7. Repeat steps 2-6 for all the range of interest of wind velocity to obtain the variation of m pairs of complex eigenvalues with wind velocity.

6.2. Structural FE models

Considering the dimension and complexity of the project of the bridge over the Messina Strait, several 3D finite element models were developed and tested in ANSYS, in order to calibrate them in such a way that the results provided could align with the results obtained by other researchers.
The numerous information available regarding the Messina Strati bridge project, allowed to build a complete model comprehensive of the designed three box deck, main span and the lateral ones.
For the numerical simulation of the mechanical behaviour three different kind of finite elements has been employed [33]:

1. Element BEAM188 is based on Timoshenko beam theory which includes shear-deformation effects. It's a three-dimensional two-node beam element, and it has six degrees of freedom at each node: translations and rotations in the three dimensions.
2. Element LINK180 is a 3D element that can be used for trusses, cables and links. It is a uniaxial tension-compression element with three degrees of freedom per node related to translation.
3. Element MASS21 is a point element having up to six degrees of freedom and it is used to model the structural mass properties. However, this element has been used only to adjust the deck mass moment of inertia, since the weight of the elements have been defined as a combination of sectional properties and material models attached to the beam elements.

A total of three different numerical models of the bridge were realized, and they are presented in the following sections.

6.2.1. Fishbone model, main span

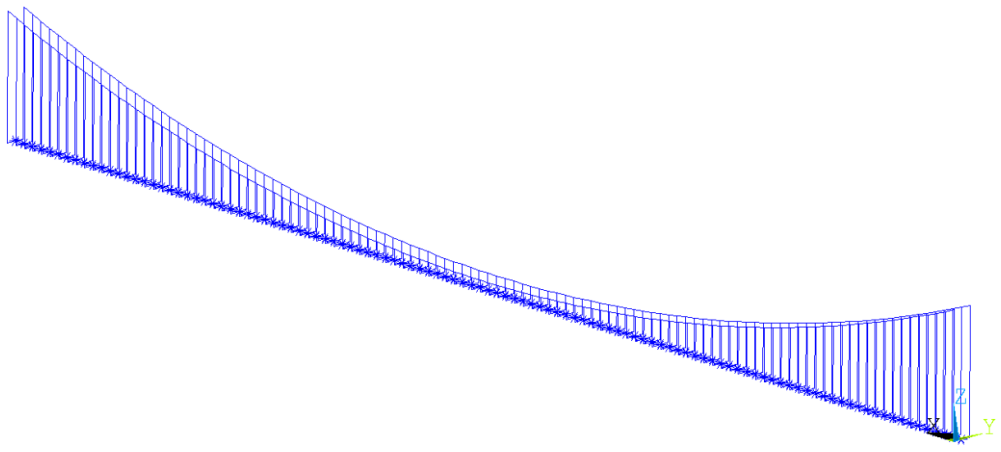

Figure 6.2 FE model 1 of the Messina Strait bridge project

In this model, the two coupled cables are modelled as two equivalent cables, one on each side of the deck, with an equivalent diameter of 1.6 metres. Similarly, the bridge's deck is represented by only its central axis, to which are assigned equivalent properties considering all three longitudinal boxes, and it is connected to the hangers, by means of cross girders, considered as rigid links.

Moreover, the deck is restrained through hinges, which allows rotation in every direction, whereas the rotation around x-axis is prevented for the cables.
The deck girders, as well as the main cables are modelled with BEAM188 elements, by defining the material and geometric properties and assign it to each component of the bridge. It's worth mentioning that the rigid links are defined with a high inertia to achieve rigid flexural behaviour and its weight is set to equal zero. On the contrary, the hangers are modelled with LINK180 elements, which transmit only tension forces between deck and main cables. Lastly element MASS21 is utilized to represents the mass moment of inertia of the deck, however, many tests have proven that the best results are obtained by setting to zero this parameter.
The geometrical and mechanical properties of the model implemented in the calculations are summarized in Table 6.1:

Span length (m)	3300
Total deck width (m)	61.13
Distance between cables (m)	52
Sag (m)	297
Cable area (m^2)	2.01
Young modulus (N/m^2)	2.10E+11
Poisson modulus	0.3
Equivalent vertical moment of inertia, Iz (m^4)	9.394
Equivalent lateral moment of inertia, Iy (m^4)	385.65
Equivalent polar moment of inertia, It (m^4)	3.0918
Deck mass per unit length (kg/m)	18000

Table 6.1 Geometrical and mechanical properties of the Messina Strait bridge project

Subsequently, the modal analysis is carried out in two steps due to the large flexibility of the structure. In the first step, the initial main cable stresses were calculated under self-weight, finally the actual modal analyses with the corresponding overall stiffness of the bridge structure. Figure 6.5 and Table 6.2 summarize only the first 10 natural frequency extracted and the corresponding vibration mode shapes, since it's known that flutter occurs usually at lower frequencies, comprehensive of a comparison with the results calculated Section 5.2 and published by Diana *et al.* in [18], Kusano in [21] and D'Asdia and Sepe in [20].

Mode	*Frequency [Hz]*	*Type*	*MATLAB*	*Diana*	*Kusano*	*D'Asdia&Sepe*	*%ΔMATLAB*	*%ΔDiana*	*%ΔKusano*	*%ΔD'Asdia&Sepe*
1	0.0331	LS	-	0.033	0.0309	0.0311	-	0.2	7.0	6.5
2	0.0622	LA	-	0.059	0.0573	0.0562	-	5.4	8.6	10.7
3	0.0646	VA	0.064	0.061	0.0606	0.0606	1.0	5.9	6.6	6.6
6	0.0862	VS	0.087	0.08	0.0811	0.0806	-0.9	7.8	6.3	6.9
5	0.0740	TA	0.09	0.081	0.0868	0.0794	-17.8	-8.6	-14.7	-6.8
9	0.0983	TS/LA	0.12	0.097	0.1032	0.0962	-18.1	1.4	-4.7	2.2
11	0.1033	LS	-	-	0.1142	0.1075	-	-	-9.5	-3.9
13	0.1289	VA	0.129	0.128	0.1279	-	-0.1	0.7	0.8	-
15	0.1381	TS/LA	-	0.129	0.1356	-	-	7.1	1.8	-
18	0.1539	LA	-	-	0.1461	-	-	-	5.3	-

Table 6.2 Modal frequencies and modal shapes comparison

Note: V (Vertical), L (Lateral), T (Torsional), S (Symmetric), A (Asymmetric)

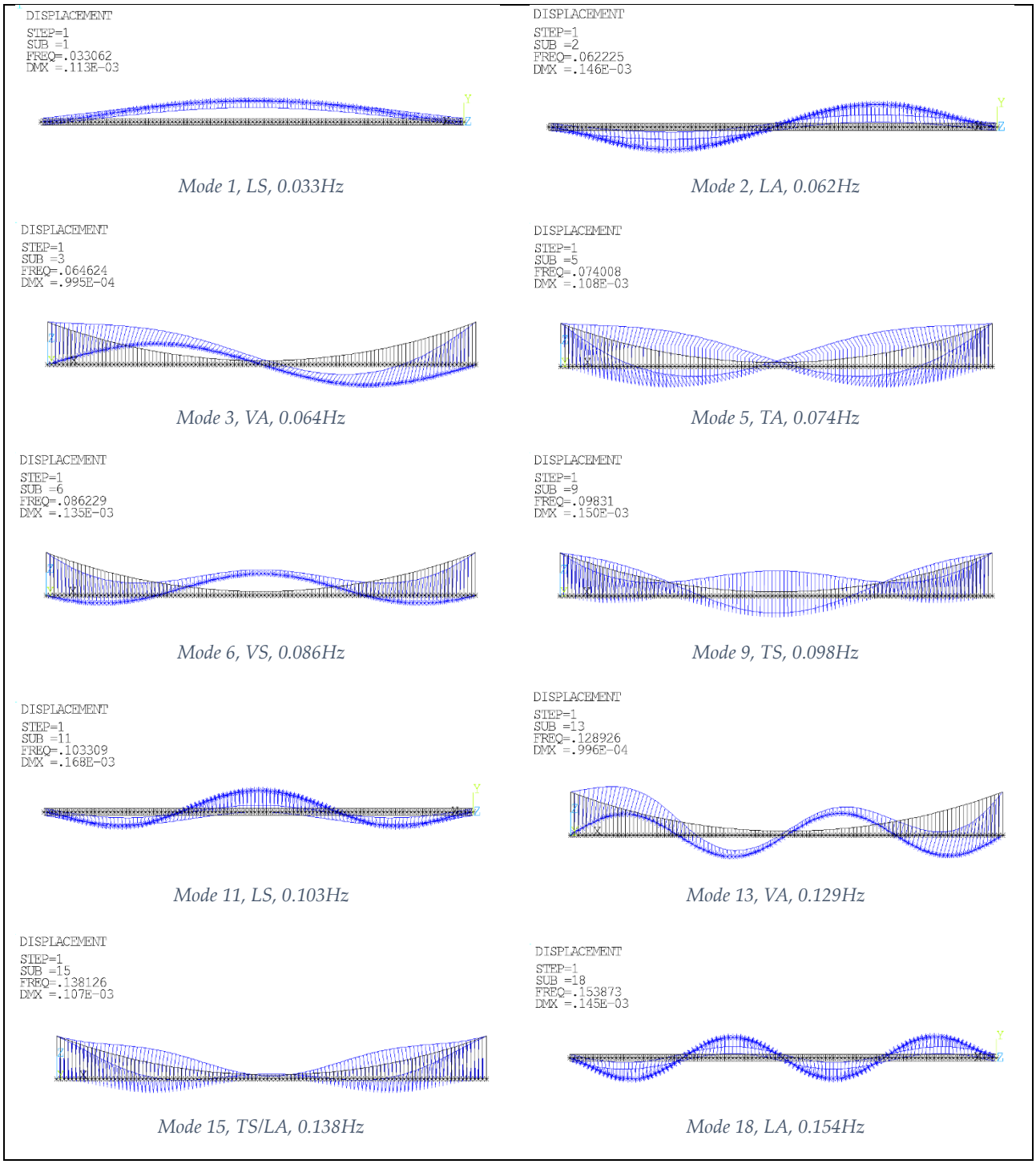

Figure 6.3 Modal frequencies and modal shapes of the model 1

6.2.2. *Fishbone model, three spans*

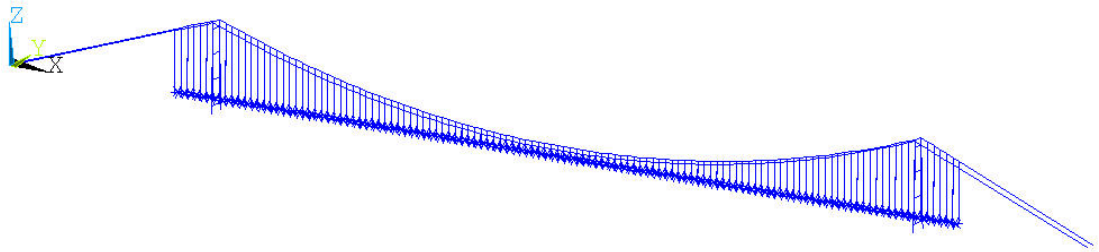

Figure 6.4 FE model 2 of the Messina Strait bridge project

This model is exactly like the previous one, but with the addition of the lateral spans and the towers. As in the previous model, the deck is restrained through hinges, whereas the tower foundations and the anchorages are fixed, so every degree of freedom is constrained.

The tower legs and cross beams are modelled using BEAM188 elements, by assigning the geometry and the steel material properties.

The geometrical and mechanical properties of the model implemented in the calculations are summarized in Table 6.3:

Total span length (m)	3666
Central span length (m)	3300
Lateral span length (m)	183
Tower height (m)	382.6
Total deck width (m)	61.13
Distance between cables (m)	52
Sag (m)	297
Cable area (m^2)	2.01
Young modulus (N/m^2)	2.10E+11
Poisson modulus	0.3
Equivalent vertical moment of inertia, Iz (m^4)	9.394
Equivalent lateral moment of inertia, Iy (m^4)	385.65
Equivalent polar moment of inertia, It (m^4)	3.0918
Deck mass per unit length (kg/m)	18000

Table 6.3 Geometrical and mechanical properties of the Messina Strait bridge project

In conclusion, Figure 6.7 and Table 6.4 summarizes the results obtained from the modal analysis, comprehensive of a comparison with the results calculated Section 5.2 and published by Diana *et al.* in [18], Kusano in [21] and D'Asdia and Sepe in [20]:

Mode	*Frequency [Hz]*	*Type*	*MATLAB*	*Diana*	*Kusano*	*D'Asdia&Sepe*	*%ΔMATLAB*	*%ΔDiana*	*%ΔKusano*	*%ΔD'Asdia&Sepe*
1	0.0328	LS	-	0.033	0.0309	0.0311	-	-0.8	6.0	5.5
3	0.0603	LA	-	0.059	0.0573	0.0562	-	2.2	5.3	7.4
4	0.0651	VA	0.064	0.061	0.0606	0.0606	1.7	6.7	7.4	7.3
7	0.0819	VS	0.087	0.08	0.0811	0.0806	-5.9	2.3	0.9	1.5
5	0.0735	TA	0.09	0.081	0.0868	0.0794	-18.3	-9.3	-15.3	-7.4
10	0.0972	TS/LA	0.12	0.097	0.1032	0.0962	-19.0	0.2	-5.8	1.1
11	0.0998	LA	-	-	0.1042	0.1075	-	-	-4.3	-7.2
15	0.1306	VA	0.129	0.128	0.1279	-	1.2	2.0	2.1	-
16	0.1355	TS/LA	-	0.129	0.1356	-	-	5.0	-0.1	-
17	0.1474	LA	-	-	0.1461	0.1282	-	-	0.9	15.0

Table 6.4 Modal frequencies and modal shapes comparison

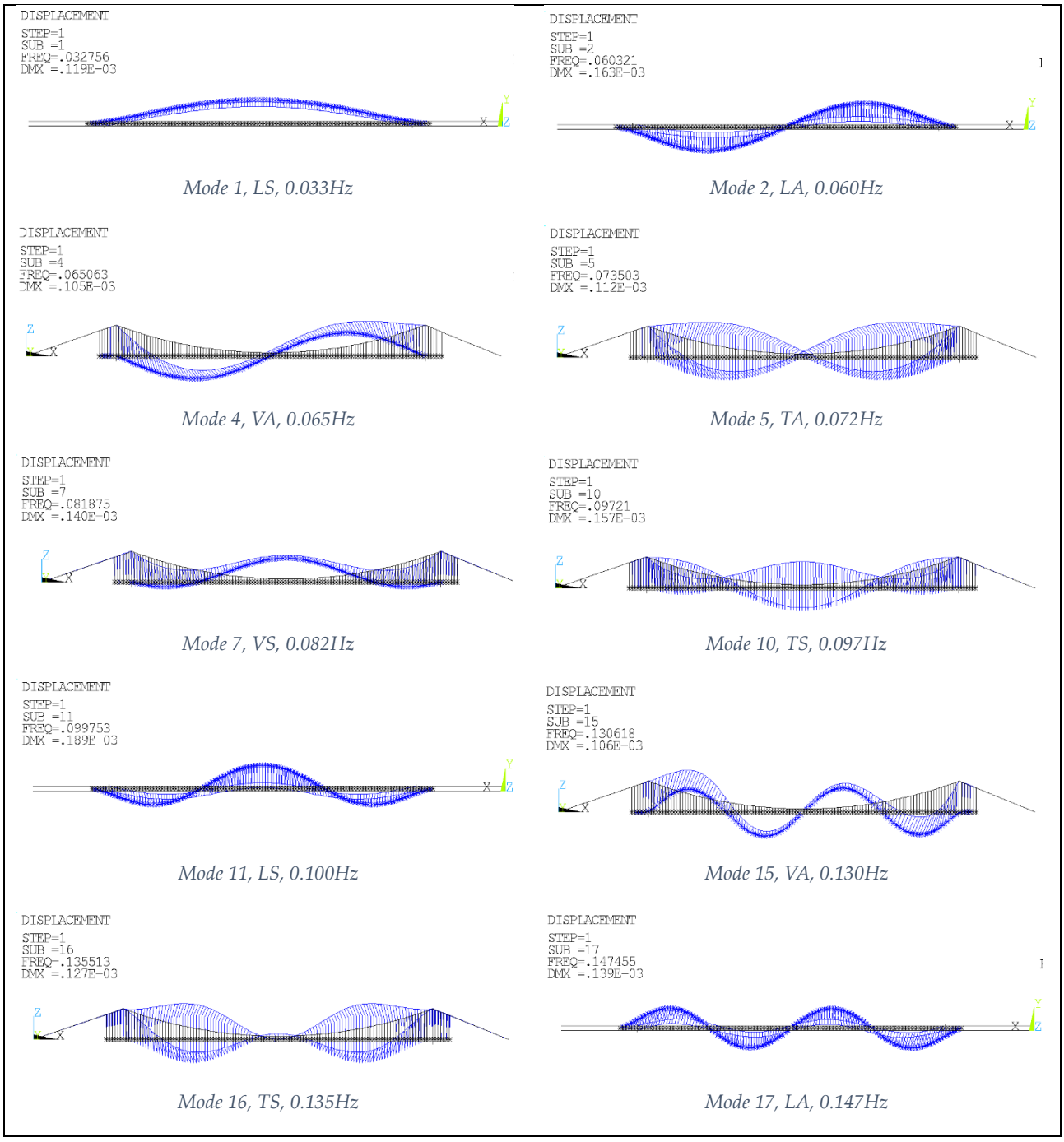

Figure 6.5 Modal frequencies and modal shapes of the model 2

6.2.3. Complete model

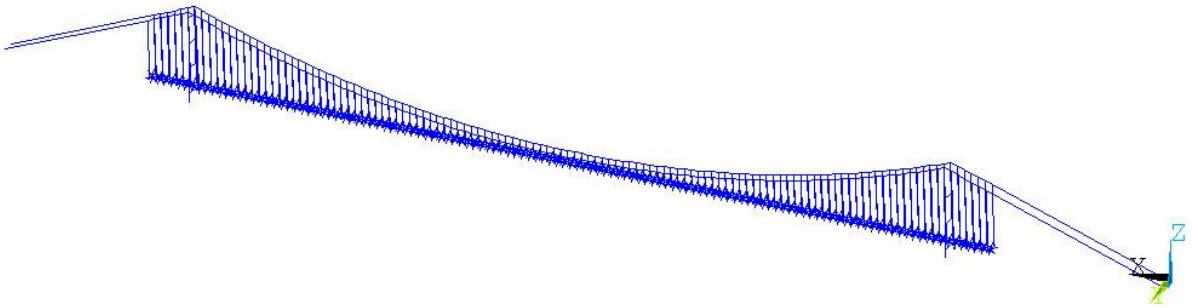

Figure 6.6 FE model 3 of the Messina Strait bridge project

To achieve a more realistic model, each of the three longitudinal boxes that make up the deck are modelled (Figure 6.9) by BEAM188 elements, to which are assigned the geometrical and mechanical properties listed in Table 6.5.
The boundary condition of this model remains unaltered from the previous model.

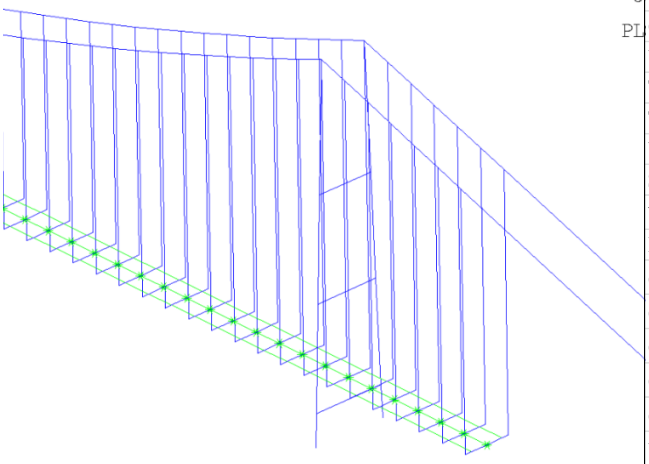

Figure 6.7 Model 3 deck detail

Total span length (m)	3666
Central span length (m)	3300
Lateral span length (m)	183
Tower height (m)	382.6
Total deck width (m)	61.13
Distance between cables (m)	52
Sag (m)	297
Young modulus (N/m^2)	2.10E+11
Poisson modulus	0.3
Cable area (m^2)	2.01
Central box area (m^2)	0.341
Central box vertical moment of inertia, Iz (m^4)	0.286
Central box lateral moment of inertia, Iy (m^4)	1.847
Central box polar moment of inertia, It (m^4)	0.653
Lateral box area (m^2)	0.645
Lateral box vertical moment of inertia, Iz (m^4)	0.623
Lateral box lateral moment of inertia, Iy (m^4)	11.02
Lateral box polar moment of inertia, It (m^4)	1.375
Deck mass per unit length (kg/m)	18000

Table 6.5 Geometrical and mechanical properties of the Messina Strait bridge project

Figure 6.10 and Table 6.6 summarizes the results obtained from the modal analysis, comprehensive of a comparison with the results calculated in Section 5.2 and published by Diana *et al.* in [18], Kusano in [21] and D'Asdia and Sepe in [20].

Mode	*Frequency [Hz]*	*Type*	*MATLAB*	*Diana*	*Kusano*	*D'Asdia&Sepe*	*%ΔMATLAB*	*%ΔDiana*	*%ΔKusano*	*%ΔD'Asdia&Sepe*
1	0.0328	LS	-	0.033	0.0309	0.0311	-	-0.8	6.0	5.5
2	0.0596	LA	-	0.059	0.0573	0.0562	-	0.9	3.9	6.0
4	0.0649	VA	0.064	0.061	0.0606	0.0606	1.4	6.3	7.0	7.0
6	0.0821	VS	0.087	0.08	0.0811	0.0806	-5.6	2.7	1.3	1.8
7	0.0853	TA	0.09	0.081	0.0868	0.0794	-5.2	5.4	-1.7	7.5
11	0.1070	TS/LA	0.12	0.097	0.1032	0.0962	-10.8	10.3	3.7	11.3
12	0.1116	VS	-	0.107	0.1078	0.1075	-	4.3	3.5	3.8
15	0.1298	VA	0.129	0.128	0.1279	-	0.6	1.4	1.5	-
16	0.1399	LA	-	-	0.1347	-	-	-	3.9	-
17	0.1450	TS/LA	-	0.129	0.1356	0.1282	-	12.4	6.9	13.1

Table 6.6 Modal frequencies and modal shapes comparison

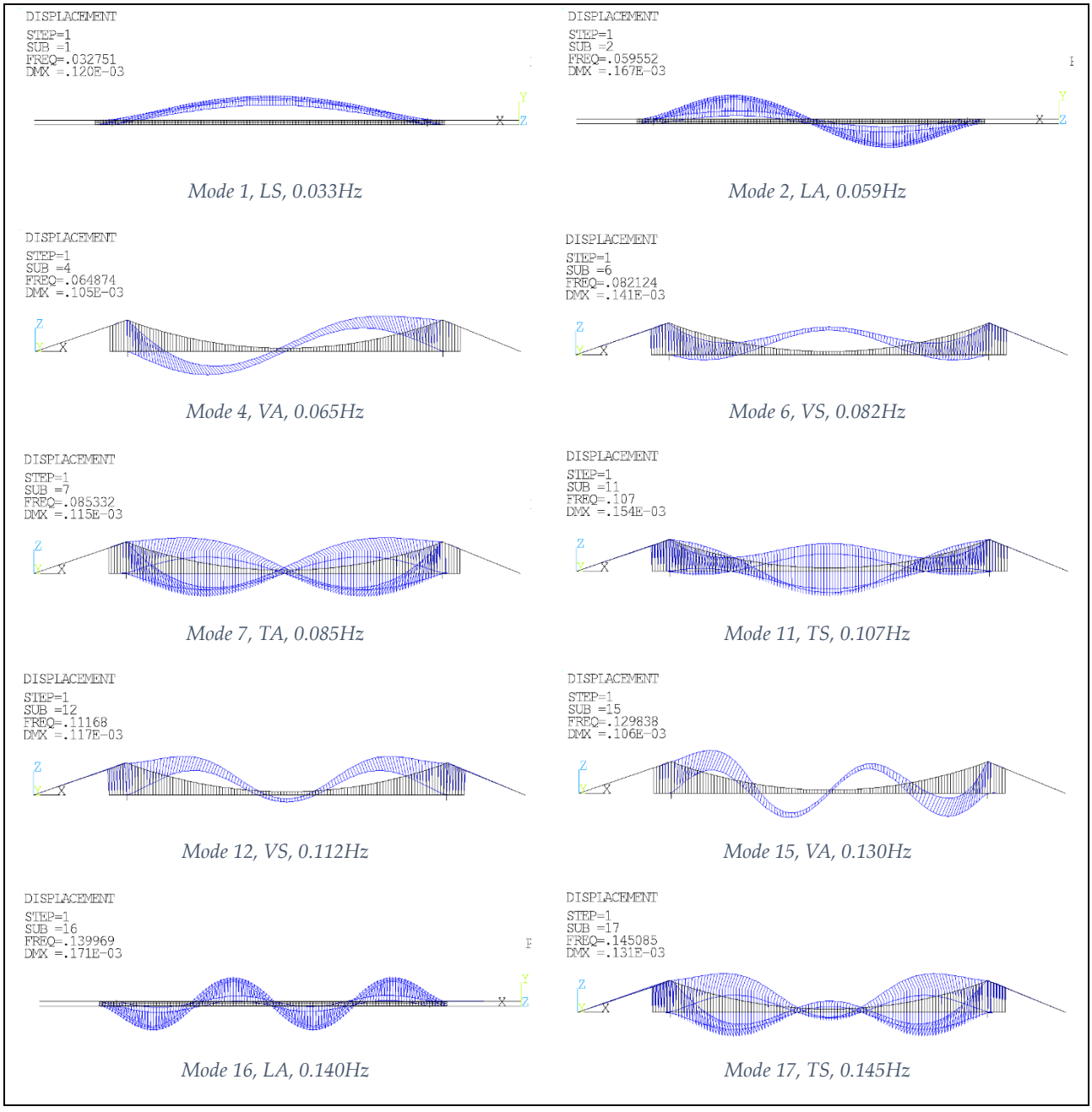

Mode 1, LS, 0.033Hz *Mode 2, LA, 0.059Hz*

Mode 4, VA, 0.065Hz *Mode 6, VS, 0.082Hz*

Mode 7, TA, 0.085Hz *Mode 11, TS, 0.107Hz*

Mode 12, VS, 0.112Hz *Mode 15, VA, 0.130Hz*

Mode 16, LA, 0.140Hz *Mode 17, TS, 0.145Hz*

Figure 6.8 Modal frequencies and modal shapes of the model 3

In conclusion, as shown in Table 6.2, Table 6.4 and Table 6.6, the results of the modal analyses yield natural frequencies and modal shapes that are consistent with the results obtained from the analytical analysis in MATLAB and with the results published by Diana *et al.*, Kusano and D'Asdia&Sepe. The relative frequency error is calculated with respect to all sets of results, and it is less of 15% for each of the three models. It can be observed that the error is usually higher for torsional modes, in fact the frequency error percentage of the other modes are all lower than 7%. The reason being, to a more accurate value of the asymmetric torsional mode frequency corresponds a higher error of the symmetric torsional frequency, and vice versa, this is due to the fact that the geometric and mechanical properties that can be modified in order to improve the relative error, are in contrast. The increase of the level of detail in model 3, didn't aggravate the error percentage with respect to the two preceding models. The frequency values are more consistent compared to Kusano's results, rather than the others: the error percentage is lower than 10%, and the subsequent flutter analysis is carried out using the flutter derivates published by the University of A Coruña, thus resulting in a more accurate comparison.

6.3. Flutter analysis

The flutter analysis is carried out on the complete model, however the MATRIX27 elements must be added prior to the analysis. Two hybrid elements, for aerostatic stiffness and damping, are attached at each of the 123 nodes situated on the middle axis of the deck and they are fully restrained at the extremities.
Figure 6.11 depicts a portion of the bridge and the MATRIX27 elements are marked in red:

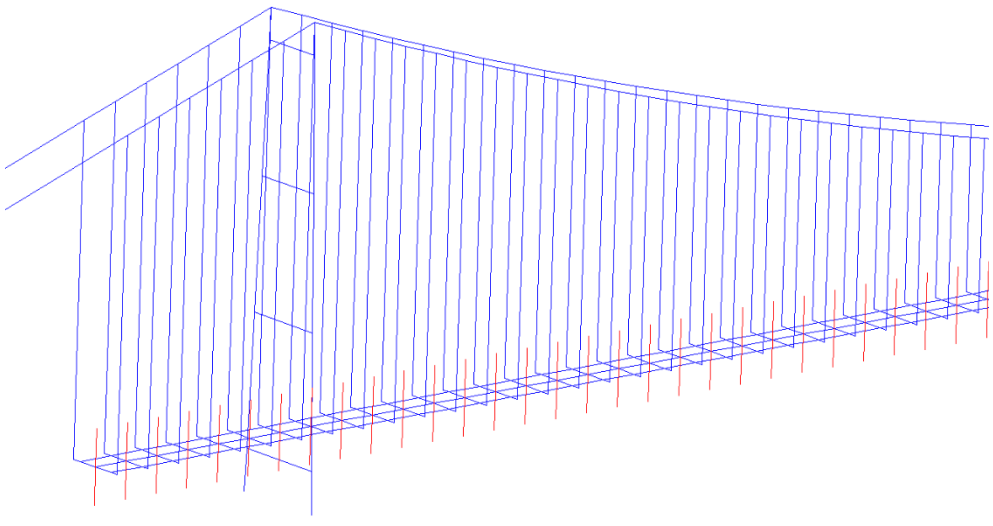

Figure 6.9 FE model 3 with MATRIX27 elements

In order to calculate the flutter velocity, flutter derivatives obtained in wind tunnel tests are also necessary. The flutter derivatives utilized in this thesis are derived by Leon at the wind tunnel of the University of A Coruña, and the whole set of 18 flutter derivatives was published in [34] and

reported in figure 6.12. Moreover, a structural damping equal to $\zeta_i = 0{,}5\%$ has been assumed for all the modes extracted.

Subsequently the analysis can be performed as illustrated in Section 6.1: an iterative procedure is applied to each of the 10 modes extracted by the modal analysis, summarized in Table 6.6.

The damped complex eigenvalue analyses were conducted on the model under wind velocities ranging from 0 to 100 m/s (0 to 360 km/h). The incremental step of wind velocity was set variable, from a standard value of 10 m/s to a minimum of 0.2 m/s when approaching instability.

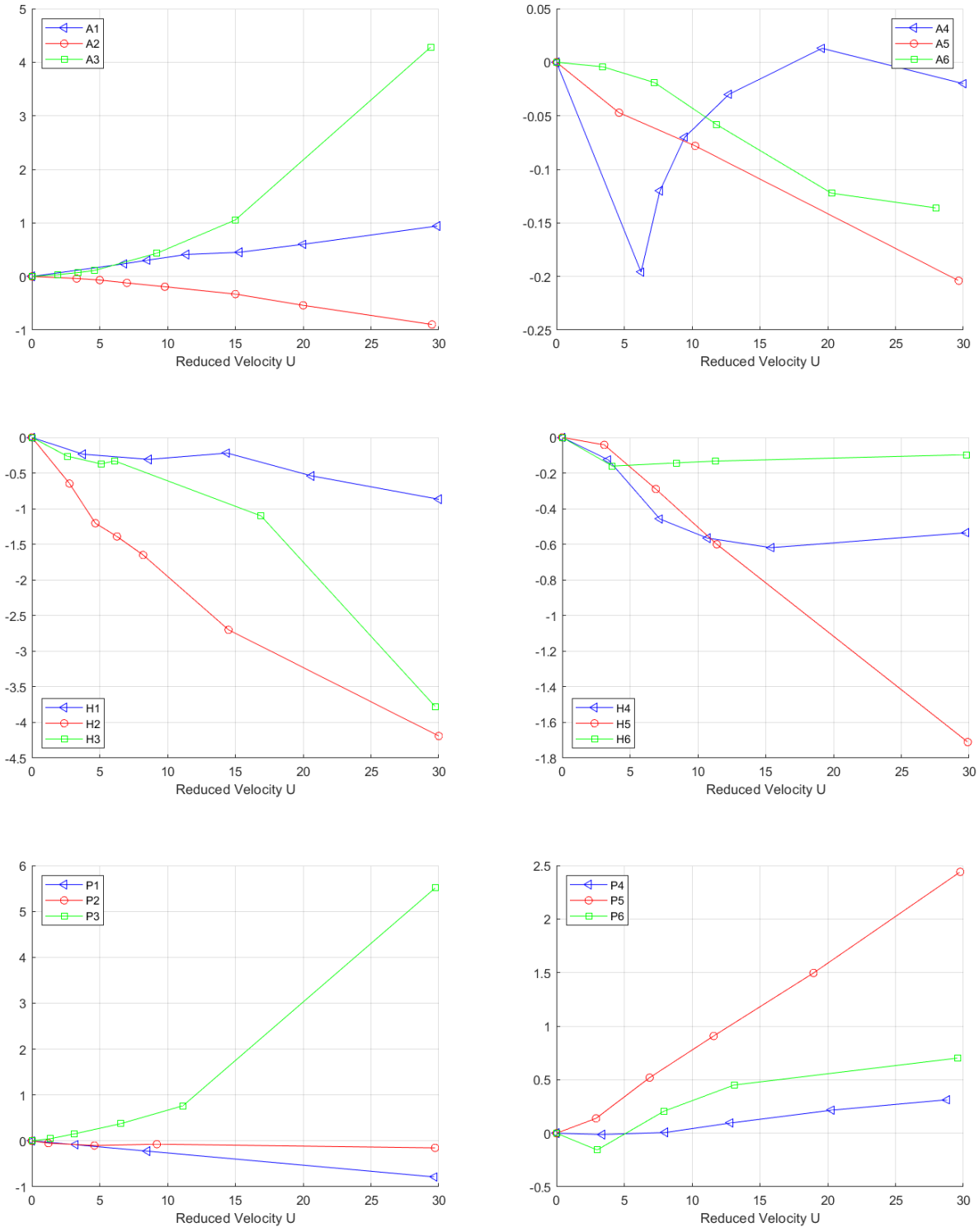

Figure 6.10 Flutter derivatives derived at the University of A Coruña

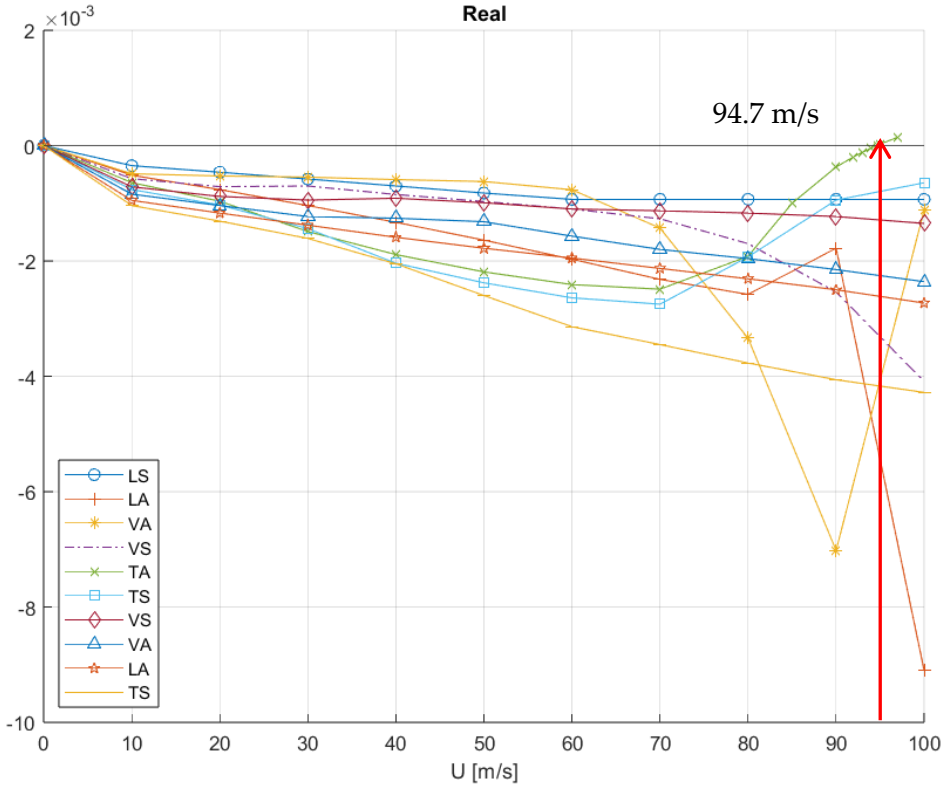

Figure 6.11 Variation of the real part of complex eigenvalues

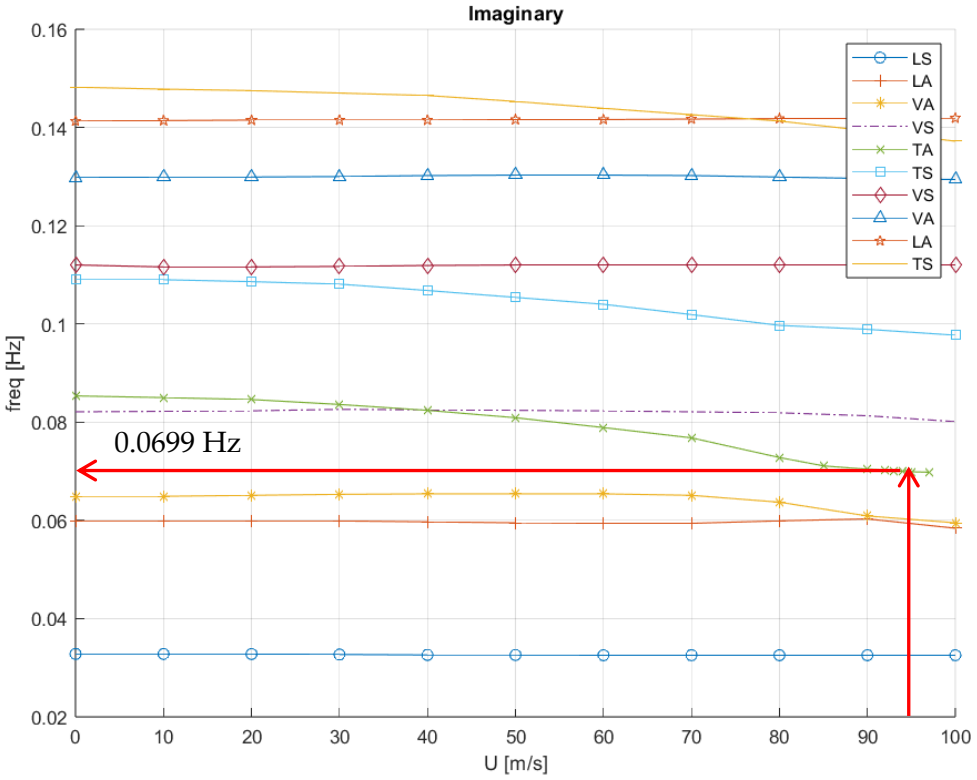

Figure 6.12 Variation of the imaginary part of complex eigenvalues

The flutter condition occurs when the real part, related to the modal damping, becomes null, and the corresponding wind velocity U_f is the critical flutter wind velocity. Hence, the analysis produced a critical flutter wind speed of 94,7 m/s and a corresponding critical frequency of 0.0699 Hz. This wind speed, corresponding to 340 km/h, belongs to the 12th level of the Beaufort scale that characterizes *hurricanes*, and it is much more severe than the strongest wind ever recorded over the Messina Strait, which was approximately 163 km/h.
Contrary to what can be deduced from the analysis output, the torsional mode itself doesn't initiate the flutter instability: the increase of wind velocity causes a variation of modal shape associated with the variation of the eigenvalues, in fact flutter instability is caused by the interaction between modes. Figure 6.15 shows how torsional, vertical and lateral degrees of freedom are coupled together when the flutter condition is approached. Nevertheless, the flutter instability is caused by a variation of the torsional asymmetric mode.

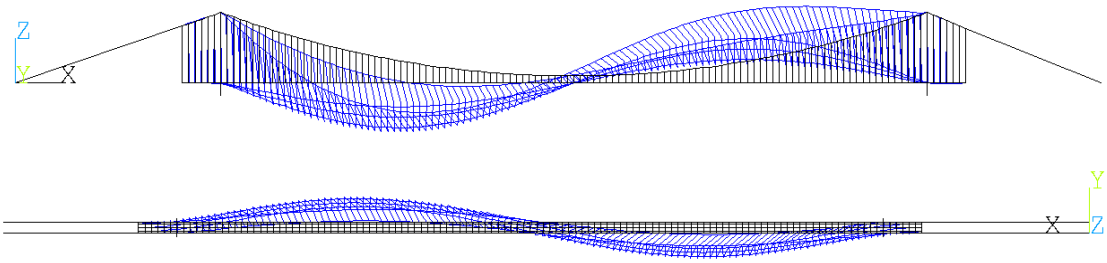

Figure 6.13 Flutter shape: coupled vertical, torsional and lateral modes

6.4. Result comparison

In conclusion, the flutter wind speed and the flutter frequency derived from the ANSYS flutter analysis in this chapter, are compared with the results obtained by Jurado *et al*. [19] and by D'Asdia and Sepe in [20], moreover they are compared with the results from the MATLAB flutter analysis of the previous chapter.

	Uf [m/s]	*f [Hz]*	*%ΔUf*	*%Δf*
ANSYS	94.7	0.0699	-	-
MATLAB	98.4	0.069	3.8	-1.3
Jurado et al.	102.7	0.066	7.8	-5.9
D'Asdia&Sepe	94	0.067	-0.7	-4.3

Table 6.7 Messina bridge flutter analysis, result comparison

As is clear from Table 6.7, the ANSYS flutter analysis produced accurate values of flutter wind velocity and flutter frequency. The flutter wind velocity is almost exactly the same value obtained by D'Asdia, resulting in a relative error of less than 1%. Compared to Jurado's value, it results in a greater error of 7,8% but still in a reasonable error rage. The comparison with the MATLAB results is considered of high interest, because the two analyses, involving different approaches and software, yield approximately the same results, thus further validating the value of the flutter wind speed.

6.5. Influence of lateral flutter derivatives

In addition to the previous flutter analysis, a further two-degree-of-freedom flutter analysis is carried out only for the critical mode, that leads to flutter instability, for the purpose of comparing the results of the two analyses.
This analysis examinates only lift and moment, whereas drag forces are not included at all, thus only flutter derivatives H_i^* and A_i^* are considered, while P_i^* are considered equal to zero. The non-zero values of the stiffness matrix and the damping matrix, reduces to 6 terms:

$$K_{ae1}^e = a\begin{bmatrix} 0 & 0 & 0 & 0 & 0 & 0 \\ 0 & 0 & 0 & 0 & 0 & 0 \\ 0 & H_6^* & H_4^* & BH_3^* & 0 & 0 \\ 0 & BA_6^* & BA_4^* & B^2A_4^* & 0 & 0 \\ 0 & 0 & 0 & 0 & 0 & 0 \\ 0 & 0 & 0 & 0 & 0 & 0 \end{bmatrix} \tag{6.14}$$

$$C_{ae1}^e = b\begin{bmatrix} 0 & 0 & 0 & 0 & 0 & 0 \\ 0 & 0 & 0 & 0 & 0 & 0 \\ 0 & H_5^* & H_1^* & BH_2^* & 0 & 0 \\ 0 & BA_5^* & BA_1^* & B^2A_2^* & 0 & 0 \\ 0 & 0 & 0 & 0 & 0 & 0 \\ 0 & 0 & 0 & 0 & 0 & 0 \end{bmatrix} \tag{6.15}$$

Subsequently the same 7 steps procedure of the previous case if followed: the iterative procedure is applied only to the asymmetric torsional mode extracted in Section 6.2.3.
The damped complex eigenvalue analyses were conducted on the model under wind velocities ranging from 0 to 120 m/s (0 to 432 km/h). The incremental step of wind velocity was set variable, from a standard value of 10 m/s to a minimum of 5 m/s when the instability was expected.

The analysis didn't produce a critical flutter wind speed in the speed range investigated, therefore flutter instability can't occur under the action of wind flows that can be expected in that site, since the maximum wind speed ever recorded is much lower than the upper limit of the range examined.
Figure 6.17 compares the variation of the real and the imaginary part of the complex eigenvalue of the asymmetric torsional mode derived with drag forces and without drag forces.
In conclusion, without taking into account the drag forces, the flutter instability doesn't occur due to the fact that only a three-degree-of-freedom coupled mode initiates the instability, as stated in Section 2.3.

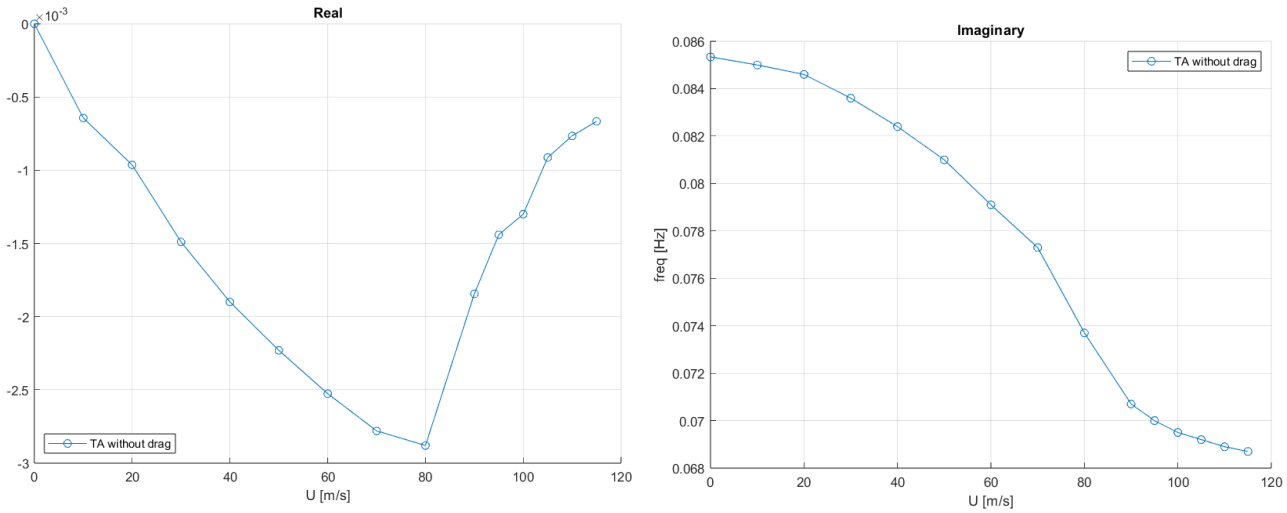

Figure 6.14 Variation of the real and the imaginary part of complex eigenvalue, without drag case

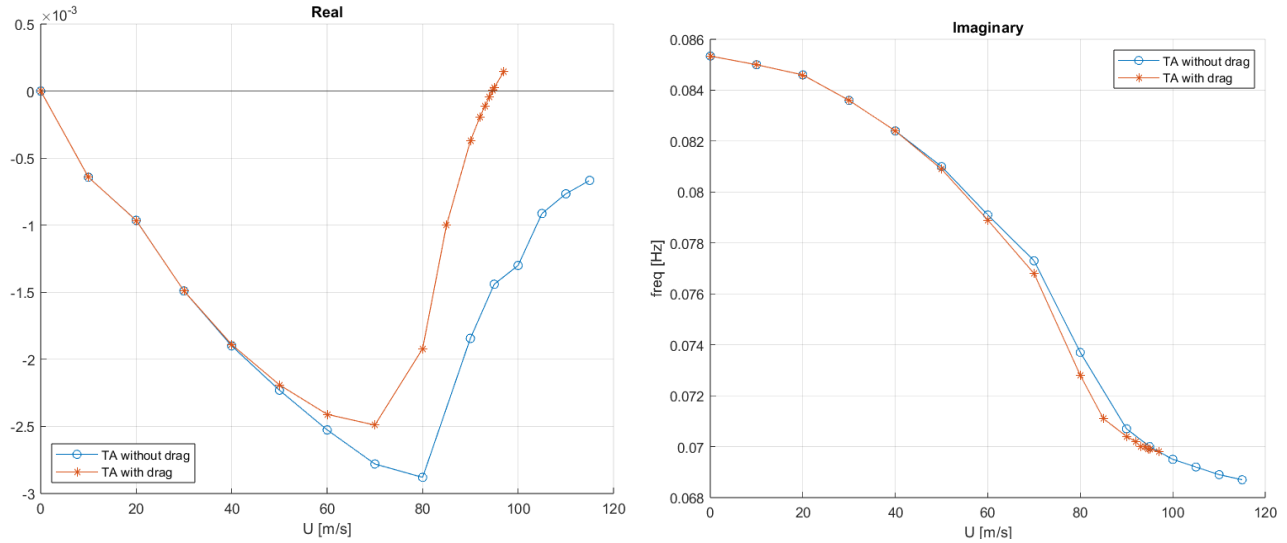

Figure 6.15 Comparison of the variation of the real and the imaginary part of complex eigenvalue

Chapter 7

The single-mode criterion

7.1. Introduction

As already mentioned in Section 2.5, damping-driven flutter occurs in bridges when negative damping in a single mode is achieved without coupling with other modes, initiating flutter as the wind velocity produces enough negative aerodynamic damping to offset the bridge's own mechanical damping.

Most flutter derivatives in bridges maintain the same sign with increasing speed, but A_2^* for some bridges may change sign as U_r increases. In several practical cases all coupling coefficients A_1^*, H_2^* and H_3^* are negligible and by assuming A_3^*, P_2^* and P_3^* negligible, with H_1^* and P_1^* negative, reveals that, for single-mode flutter to occur A_2^* must become strongly positive for some value of K. When this occurs, the torsional mode causes the overall system to flutter. However, it may also be observed how the damping effects from vertical and lateral motions can weight against flutter even when the tendency to torsional instability is present.

The uncoupled single-degree-of-freedom flutter can be analysed as follows, by pre- and post-multiplying Equation 2.23 by the eigenvector $\{\delta_{0,j}\}$ related to the j-th mode:

$$\{\delta_{0,j}\}^T \left(-\omega^2[M] + i\omega\left([C] - \frac{1}{2}\rho U[C^*]\right) + [K] - \frac{1}{2}\rho U^2[K^*]\right)\{\delta_{0,j}\} = 0 \tag{7.1}$$

It's worth mentioning that in order to uncouple the problem, $[C]$ is generally assumed as Rayleigh damping matrix:

$$[C] = \alpha[M] + \beta[K] \tag{7.2}$$

Where α and β are proportionality coefficients of Rayleigh damping.

As mentioned in Section 2.5, Scanlan (1978) [25] and Scanlan and Jones (1990) [17], introduced a single-mode criterion, based on the damping terms in square brackets of Equation 7.2, which compares the aeroelastic damping with the mechanical damping of the system:

$$H_1^*(\bar{K})G_{hi} + P_1^*(\bar{K})G_{pi} + A_2^*(\bar{K})G_{\alpha i} \geq \frac{4\xi_i I_i}{\rho B^4 L_d}\frac{\omega_i}{\bar{\omega}_i} \tag{7.3}$$

In order to apply Equation 7.3 in a finite Element Framework it is necessary to define the following terms:

- The variables G_{hi}, G_{pi} and $G_{\alpha i}$ are the modal integrals in the heave, sway ad torsional directions:

$$G_{hi} = \{u_z\}_i^T \cdot \{u_z\}_i \tag{7.4}$$

$$G_{pi} = \{u_y\}_i^T \cdot \{u_y\}_i \tag{7.5}$$

$$G_{\alpha i} = \{\vartheta_x\}_i^T \cdot \{\vartheta_x\}_i \tag{7.6}$$

- u_z, u_y and ϑ_x are the deflection in vertical direction, in transverse direction and the rotation around longitudinal axis, respectively, of the bridge's deck;
- ξ_i is the generalized damping ratio;
- I_i in the generalized inertia:

$$I_i = \{\delta\}_i^T [M] \{\delta\}_i \tag{7.7}$$

- δ is a vector containing all the degree of freedom of the whole bridge;
- [M] is the mass matrix of the bridge;
- L_d being the deck length.

The vectors containing the nodes degrees of freedom and the mass matrix can be extracted from ANSYS [35], whereas the single-mode criterion has been examined graphically, by means of a MATLAB code, for each mode considered. The resulting graph compares the variation of the aeroelastic damping, the left term of Equation 7.1 with the mechanical damping of the system, the constant value on the right side. The single-mode flutter occurs when the system's total damping vanishes: when left term exceeds the right value and for the lowest wind velocity that validates the equality of Equation 7.1, flutter has been initiated with the corresponding flutter frequency being computed from Equation 7.2. However, the frequency variation with increasing speed is assumed to be negligible, therefore the frequency ratio of the right term equals to one.

In the following sections, two cases have been examined:

- The Tacoma Narrows bridge;
- The Messina Strait bridge project.

The criterion is applied to the subject of this thesis as well as the Tacoma Narrows bridge, a well-known case of failure due to instability in order to validate the criterion, since the Messina Strait bridge is expected to be stable to single-degree-of-freedom flutter as result of the deck girders design, which resembles an airfoil.

7.2. The Tacoma Narrows bridge case

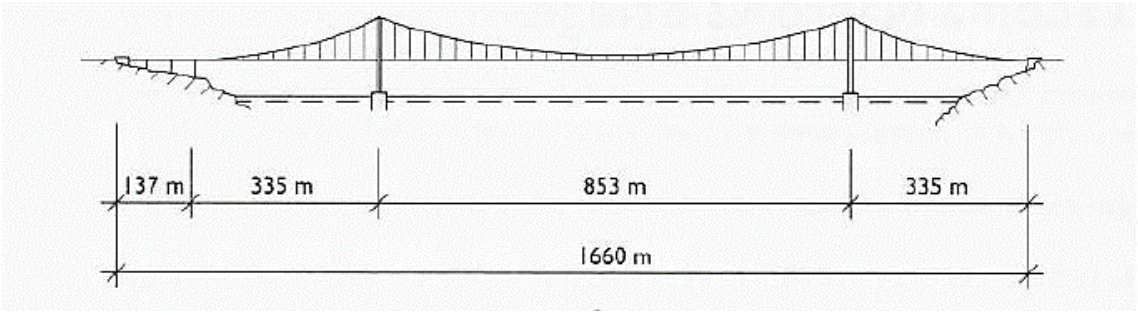

Figure 7.1 Lateral view of Tacoma Narrows bridge

The Tacoma Narrows Bridge was opened to traffic on July 1st, 1940. It was the third longest suspension bridge at the time with a central span of 853 m and it was characterized by the extreme slenderness of the deck thus it had a very low torsional and vertical bending stiffness.
In the first months of service, the bridge presented some mild vertical oscillation, but on November 7th 1940, the bridge developed twisting oscillation of the deck caused by a wind speed of 18 m/s, much lower than the value calculated during design phase, that led the bridge to collapse a few hours later.

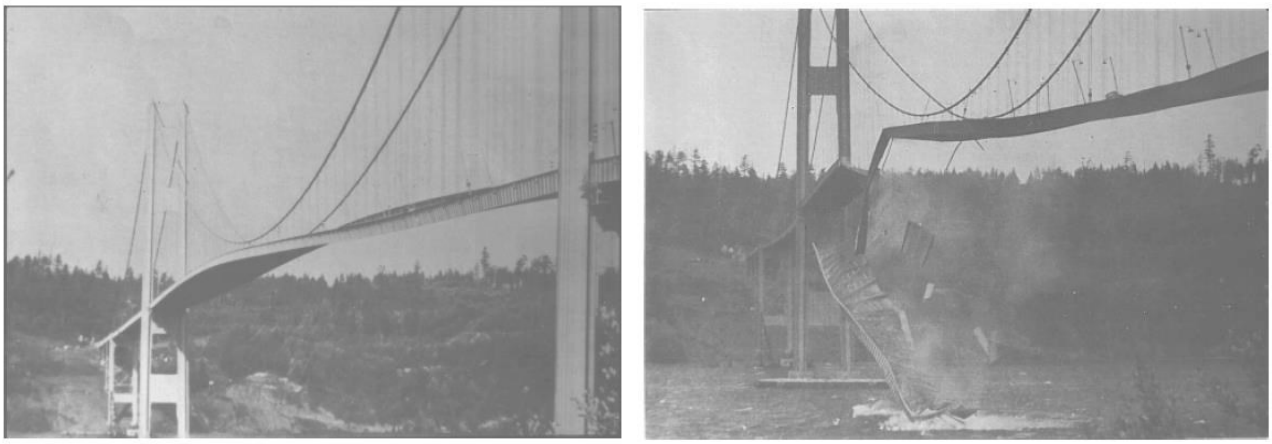

Figure 7.2 Tacoma Narrows bridge collapse

Only the torsional asymmetric mode is investigated, since it is the one that caused the collapse.
The torsional mode is governed by the A_2^* flutter derivative and Figure 7.3 illustrates some examples of A_2^* flutter derivatives, the function related to the Tacoma bridge deck is marked with "1" and it changes sign from a reduced wind velocity equal to 2.

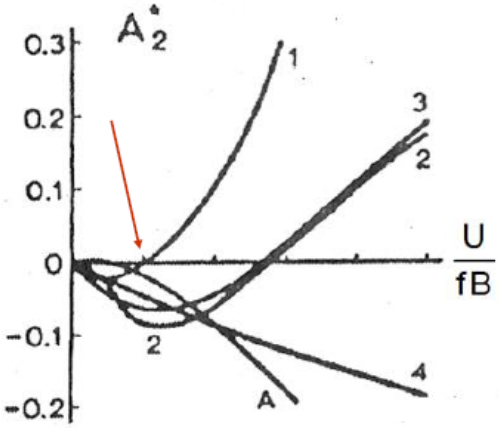

Figure 7.3 Examples of A_2^* flutter derivatives

By implementing the frequency, corresponding to the torsional mode, geometrical properties, such as deck element length and deck width, modal properties extracted in ANSYS APDL, and the three flutter derivatives mentioned above in MATLAB, the software generated the solution in Figure 7.4:

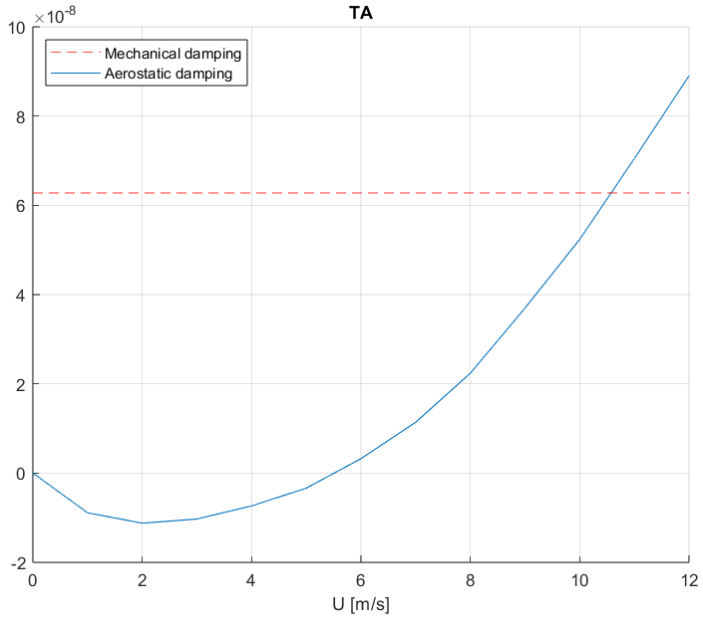

Figure 7.4 Torsional single-degree-of-freedom flutter

The torsional instability initiates at a speed of 10.5 m/s and at a frequency of 0.213 Hz, when the aeroelastic damping changes sign and becomes greater than the mechanical damping. Then resulting total damping becomes negative which causes torsional oscillation on the bridge deck, that could lead to failure.

In literature, the torsional instability speed has been estimated to be in a range of 8 m/s and 12 m/s, therefore, the value obtained with the single-mode criterion aligns perfectly with the results obtained by other researchers.

7.3. The Messina Strait bridge case

In this case the single-mode has been applied to the first lateral, vertical and torsional modes. Figure 7.5 reports the flutter derivatives examined with this approach:

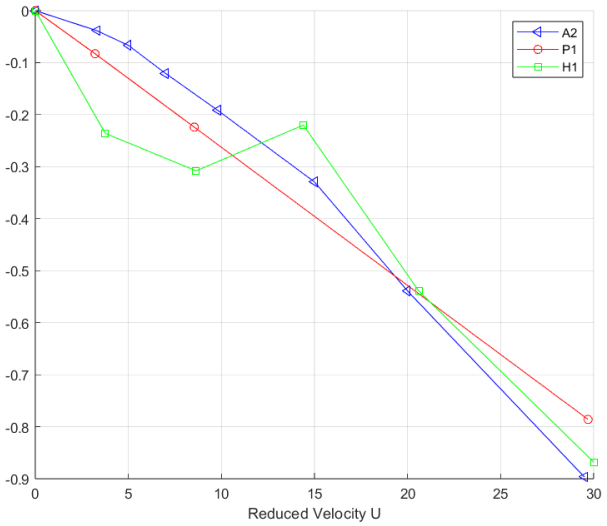

Figure 7.5 A_2^*, P_1^* and H_1^* of Messina Strait bridge

As it is clear from the Figure 7.5, the flutter derivatives mentioned before are all negative function for any reduced wind velocity value, therefore the criterion of Equation 7.1 is expected to be always false and the deck always stable. The results provided by the software are reported in Figure 7.6, 7.7 and 7.8.

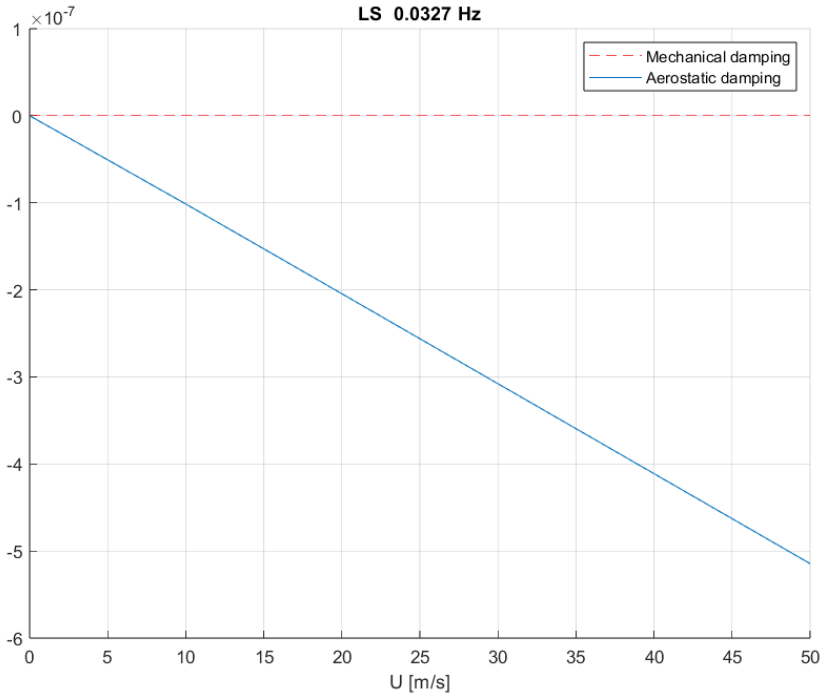

Figure 7.6 Sway single-degree-of-freedom flutter

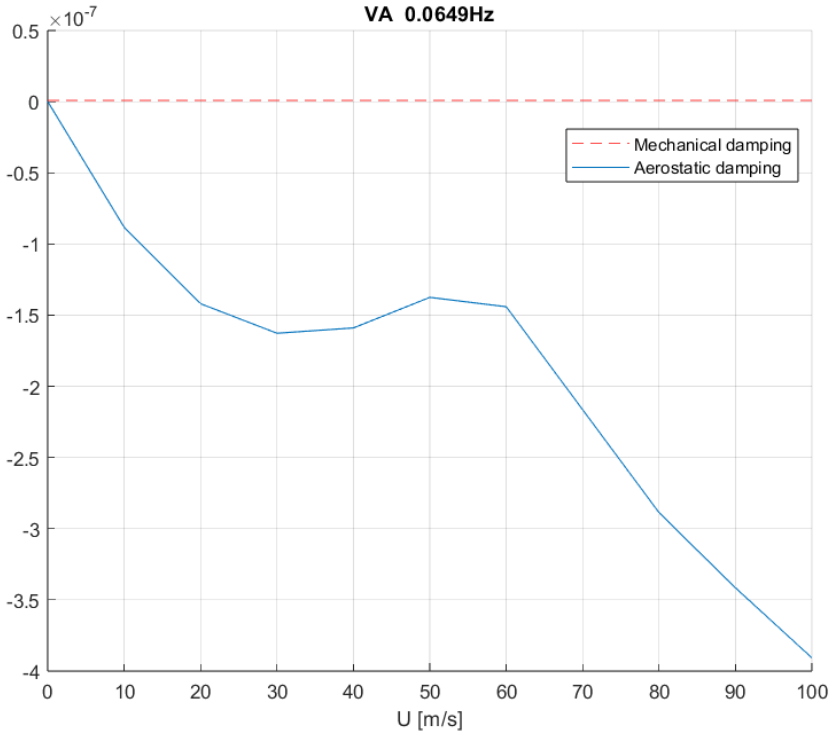

Figure 7.7 Bending single-degree-of-freedom flutter

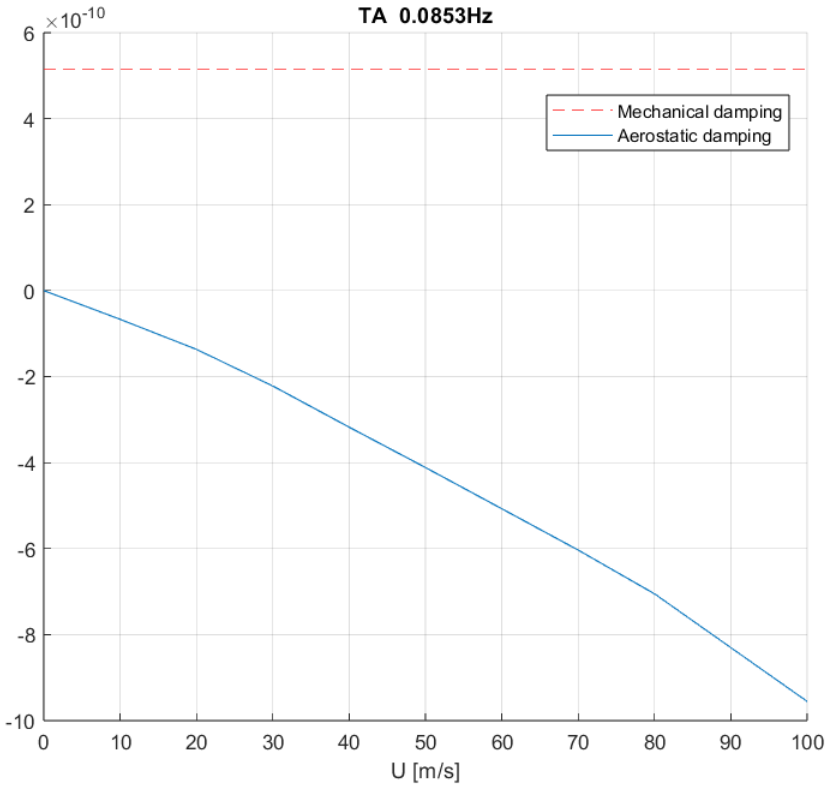

Figure 7.8 Torsional single-degree-of-freedom flutter

The single-mode criterion applied to the Messina Strait bridge project case, didn't produce any critical wind speed since the flutter derivatives never become positive therefore the mechanical damping, in this simplified model, is always greater than the aeroelastic damping. Moreover, the aeroelastic damping is beneficial to the system's total damping, since it is negative and on the other side of the mechanical damping in Equation 7.1, they can be summed to obtain the total damping, which is improved compared with respect to the mechanical one only.

In conclusion the deck can't experience single-degree-of-freedom flutter in any mode, since the critical mechanism involves a coupling between two, or more, modes. However, this behaviour was expected being the flutter derivatives all negative and the deck specifically designed to resemble an air foil shape.

Chapter 8
Conclusions

A critical phase of the design process of a long-span bridge is certainly the aerodynamic analysis, which assesses the behaviour of the structure when it interacts with a wind flow, however under certain conditions, an aeroelastic instability could arise, that causes the bridge to oscillate which could lead to structural failure.
The project of the bridge over the Messina Strait is analysed by means of both numerical and analytical approaches, focusing on the problem of flutter instability.

Although several Finite Element models have been developed, the flutter analysis was performed only on the last, and most complete one, which is comprehensive of the airfoil multi-box deck, the main span and the lateral spans. This analysis was carried out on ANSYS APDL, a software that allowed to take into account the stiffening effect of the cables as well as the aerodynamic forces, modelled by flutter derivatives. Initially a modal analysis was performed on every model developed, and the natural frequencies obtained were compared with the results obtained in other studies, thus the third model was selected to be tested with aerodynamic forces, since the level of detail was higher and the relative error of the natural frequency, compared with literature values, were lower than the results produced by the other models. The flutter analysis was carried out through an iterative process, applied to each of the modes considered. In the end the critical flutter wind speed and the flutter frequency were obtained.
Moreover, the same analysis was performed with a purely analytical approach, by means of a MATLAB code, which is programmed to include aerostatic nonlinearities, such a stiffening induced by lift forces and Prandtl-like second order effects due to drag force.

At the end of Chapter 6, the results obtained from both the analyses were compared with the results obtained by the research groups examined:

	Uf [m/s]	*f [Hz]*	*%ΔUf*	*%Δf*
ANSYS	94.7	0.0699	-	-
MATLAB	98.4	0.069	3.8	-1.3
Jurado et al.	102.7	0.066	7.8	-5.9
D'Asdia&Sepe	94	0.067	-0.7	-4.3

Table 8.1 Flutter analysis result comparison

As Table 8.1 demonstrates, both the methods employed produced accurate results in terms of flutter velocity and flutter frequency, that are perfectly in line with the results by Jurado et al. [19] and D'Asdia and Sepe [20], whereas Diana *et al.* didn't provide an exact value, but they estimated a flutter velocity over 80 m/s.
It's important, to point out that the MATLAB code employed was able to capture the phase difference that occurs between the vertical mode and the torsional mode, and given that the relative difference between the numerical and analytical approaches is not significant, it can be concluded that the method is as valid as the finite element analysis, however it involves a much more simplified model, therefore a reduced computational time.

In addition, the influence of the lateral flutter derivatives was evaluated by performing a flutter analysis on the same model as before but neglecting the flutter derivatives related to drag force. However, flutter instability didn't arise for wind speeds up to 120 m/s, for this reason it can be concluded that lateral flutter derivatives are essential, since the critical flutter mode is a vertical, lateral and torsional coupled mode.

Another approach was investigated, the single-mode criterion, originally proposed by Scanlan [16], has been applied to the model, but it didn't lead to flutter instability. This is due to the fact that the flutter derivative that governs this type of flutter, also known as damping driven flutter, are negative for every reduced velocity, which is a characteristic feature of this type of bridge decks, designed to resemble air foils, being extremely stable to single-degree-of-freedom flutter instability.

Nevertheless, these results confirm the excellent aeroelastic behaviour of the Messina Strait bridge, since maximum wind speed ever recorded at the bridge's location in significantly lower than the flutter speed calculated on the approved project.

References

[1] "Wikipedia," [Online]. Available: https://en.wikipedia.org/wiki/Suspension_bridge.

[2] M. Cid Montoya, "A fully numerical methodology for optimization of deck shape and cables size in long-span bridges considering aeroelastic and structural constraints," Doctoral thesis, University of A Coruña, 2017.

[3] "New Civil Engineer," [Online]. Available: https://www.newcivilengineer.com/the-future-of/future-of-modular-construction-turkeys-suspension-bridge-kit-06-05-2022/.

[4] C. Bruzzi, "Messina, Analisi costi - benefici per la valutazione dei (grandi) progetti di investimento pubblico," Master thesis, Politecnico di Torino, 2022.

[5] F. Brancaleoni, G. Diana , E. Faccioli and G. Fiammenghi , The Messina Strait Bridge: A Challenge and a Dream, Taylor & Francis Ltd, 2009.

[6] "B2 Bill Brown's Bridges," [Online]. Available: https://b2.co.uk/world-bridges/messina-straits-crossing/.

[7] "Strettoweb," [Online]. Available: https://www.strettoweb.com/2022/11/ponte-stretto-campata-unica/1442924/.

[8] "Wikipedia," [Online]. Available: https://it.wikipedia.org/wiki/Ponte_sullo_stretto_di_Messina.

[9] "Webuild group," [Online]. Available: https://www.webuildgroup.com/it/ponte-sullo-stretto/.

[10] "Marco Peroni Ingegneria," [Online]. Available: https://www.marcoperoni.it/.

[11] "Ingenio," [Online]. Available: https://www.ingenio-web.it/articoli/storia-tecnologia-e-futuro-dei-ponti-sospesi-nel-libro-di-marco-peroni/.

[12] R. H. Scanlan, "Aerodynamics of cable-supported bridges," *Journal of Constructional Steel Research*, vol. 39, no. 1, pp. 51-68, 1996.

[13] A. Namini, P. Albrecht and H. Bosch, "Finite Element-Based Flutter Analysis of Cable-Suspended Bridges," *Journal of Structural Engineering*, vol. 118, pp. 1509-1526, 1992.

[14] A. Carpinteri, Advanced structural mechanics, Taylor&Francis Group, 2017.

[15] W. Chen and L. Duan, Bridge Engineering Handbook: Substructure Design (2nd ed.), CRC Press, 2014.

[16] R. H. Scanlan, "Interpreting Aeroelastic Models of Cable-Stayed Bridges," *Journal of Engineering Mechanics*, vol. 113, no. 4, 1987.

[17] R. H. Scanlan and N. P. Jones, "Aeroelastic Analysis of Cable-Stayed Bridges," *Journal of Structural Engineering*, vol. 116, 1990.

[18] Diana, G., M. Falco and F. Cheli, "The Aeroelastic Study of the Messina Straits Bridge," *Natural Hazards*, vol. 30, pp. 79-106, 2003.

[19] A. Baldomir, I. Kusano, S. Hernandez and J. Jurado, "A reliability study for the Messina Bridge with respect to flutter phenomena considering uncertainties in experimental and numerical data," *Computers & Structures,* vol. 128, pp. 91-100, 2013.

[20] P. D'Asdia and V. Sepe, "Aeroelastic instability of long-span suspended bridges: a multi-mode approach," *Journal of wind engineering and industrial aerodynamics,* Vols. 74-76, pp. 849-857, 1998.

[21] I. Kusano, "Reliability based design optimization of long-span bridges under flutter contraint," Doctoral thesis, Univeristy of A Coruña, 2015.

[22] J. Jurado, S. Hernández, F. Nieto and A. Mosquera, Bridge Aeroelasticity: Sensitivity Analysis and Optimal Design, WIT Press, 2011.

[23] I. Kusano, A. Baldomir, J. Á. Jurado and Santiago Hernández, "Probabilistic optimization of the main cable and bridge deck of long-span suspension bridges under flutter constraint," *Journal of Wind Engineering and Industrial Aerodynamics,* vol. 146, pp. 59-70, 2015.

[24] C. Mannini and C. Borri, Aeroelastic phenomena and pedestrian-structure dynamic interaction on non-conventional bridges and footbridges, Firenze University Press, 2010.

[25] R. Scanlan, "The action of flexible bridges under wind, I: Flutter theory," *Journal of Sound and Vibration,* vol. 60, pp. 187-199, 1978.

[26] H. Santiago, J. Jose, B. F. and Baldomir Aitor, "A comparison of flutter speed of the Messina Bridge considering several cable configurations," *WIT Transactions on the Built Environment,* vol. 84, pp. 437-446, 2005.

[27] G. Piana and A. Carpinteri, "Long-span suspension bridge flutter analysis with drag force effects," *Journal of Applied and Computational Mechanics,* vol. 7(SI), p. 1077–1089, 2021.

[28] S. Russo, G. Piana and A. Carpinteri, "Linear aeroelastic analysis of suspension bridges with second-order effects," in *2nd International Conference on Computations for Science and Engineering (ICCSE2)*, Rimini Riviera, Italy, August 30-September 2, 2022.

[29] S. Russo, G. Piana and A. Carpinteri, "Multimodal aeroelastic analysis of suspension bridges with aerostatic nonlinearities," in *XII International Conference on Structural Dynamics (EURODYN 2023)*, Delft, The Netherlands, July 2-5, 2023.

[30] X. Hua and Z. Chen, "Full-order and multimode utter analysis using ANSYS," *Finite Elements in Analysis and Design,* vol. 44, pp. 537-551, 2008.

[31] S. Russo, L. Patruno, G. Piana and A. Carpinteri, "Preliminary flutter stability assessment of the double-deck George Washington Bridge," *Applied Sciences,* vol. 13, no. 11, p. 6389.

[32] S. Russo, "Fluid-dynamic and flutter analysis of the George Washington suspension bridge," Master thesis, Politecnico di Torino, 2019.

[33] *ANSYS Mechanical APDL Element Reference,* ANSYS, Inc., 2018.

[34] A. Leon, "Análisis aeroelástico de puentes soportados por cables en el dominio," Doctoral thesis, University of A Coruña, 2009.

[35] "ANSYS tips," [Online]. Available: https://www.ansystips.com/2017/10/export-stiffness-matrix-from-ansys.html.